Exploiting Interfacial Phenomena to Expel Matter from its Substrate

Ranit Mukherjee

Dissertation submitted to the Faculty of the
Virginia Polytechnic Institute and State University
in partial fulfillment of the requirements for the degree of

Doctor of Philosophy
in
Engineering Mechanics

Jonathan B. Boreyko, Chair
Jiangtao Cheng
David A. Dillard
Robert B. Moore
Anne E. Staples

July 30, 2021
Blacksburg, Virginia

Keywords: Interfacial phenomena, jumping-droplet condensation, spore dispersal, frost, SLIPS

Exploiting Interfacial Phenomena to Expel Matter from its Substrate

Ranit Mukherjee

(Abstract)

Spontaneous expulsion of various forms and types of matter from their solid substrates has always been an integral part of interfacial physics problems. A thorough understanding of such interactions between a solid surface and different soft materials not only expands our theoretical knowledge, but also has applications in self-cleaning, omniphobic surfaces and phase-change heat transfer. Although there is a renewed interest in the design of robust functional surfaces which can passively remove highly viscous liquids or dew, or retard ice accretion or frost formation, the physics of several dewetting and/or deicing mechanisms are yet to be fully understood. Even though we know how jumping-droplet condensation offers significantly better heat transfer performance than regular dropwise condensation and can liberate foreign particles, fundamental questions on the effect of surface orientation on jumping-droplet condensation or how it helps in large-scale fungal disease epidemic in plants are still unanswered. Thus, we first try to fill the knowledge gap in jumping-droplet condensation by characterizing their orientation-dependence and their role in a large-scale pathogenic rust disease dissemination among wheat. Unfortunately, understanding of such dewetting mechanisms does not necessarily translates to prevention or removal of ice and frost on subzero surfaces. Use of superhydrophobic structures or hygroscopic materials to retard the growth of frost was found to be limiting. Therefore the search for an efficient, inexpensive, and environmentally favorable anti-icing or de-icing mechanism is still underway. Here we give a framework for making a novel de-icing construct by analyzing a peculiar jumping frost phenomena where frost particles spontaneously jump off the surface when a polar liquid is brought above. Lastly, we demonstrate a simple and cost-effective technique to design a slippery liquid-infused surface from low-density hydrocarbon-based polymers, which is able to effectively remove a wide variety of soft materials. The main all-encompassing theme of this dissertation is to enhance our understanding of several dewetting phenomena, which might enable better design and/or mitigation strategies to control the expulsion of various forms of matter from a wide variety of surfaces.

Exploiting Interfacial Phenomena to Expel Matter from its Substrate

Ranit Mukherjee

(General Audience Abstract)

A few years back, a laundry detergent company in India came up with a famous ad campaign; it showed kids coming home from school with dirt all over their clothes to face the wrath of their parents. Rather than casually disparaging their mischievousness, the ad would make us think with their tagline: "*Agar daag*[1] *lagne se kuch achha hota hain, toh daag achhe hain na? (**Fig.** If something good comes out of a mess, is it a mess?)*". While this presents to us an excellent philosophical conundrum, in reality, we always find ways to get rid of foreign materials from surfaces of everyday use. Using water or dirt-repellent coatings on our shoes/clothes/car windshields or in worst case, spending hours trying to clean frost off our cars is something we are all familiar with. Finding innovative ways to remove unwanted materials from surfaces is not limited to humans, but also exhibited by various natural organisms. The excellent water repellency of lotus leaves, antifogging abilities of mosquito eyes or cicada wings, and slipperiness of pitcher plants are just few examples of natural self-cleaning surfaces designed to keep foreign materials or dew droplets off the surface. Sometimes we take a *leaf* or two out of these natural designs to help our cause.

Surfaces with extreme water repellency are called superhydrophobic (*hydro*: water, *phobos*: fear). For a long time, gravity was considered to be the only passive droplet removal mechanism on these surfaces. About ten years ago, researchers found out that when two or more small dew droplets come together on these surfaces, they jump off the surface. Compared to the gravity removal, much smaller droplets can be removed via this method resulting in better anti-fogging qualities and heat transfer performance on the surface. As the jumping droplet event itself is independent of gravity, it was long assumed that the performance of these surfaces would not be dependent on their orientation. These jumped droplets can also take off with contaminating particles by partially or fully engulfing them. A recent study has brilliantly showed how rust spores are liberated from the superhydrophobic wheat leaves via jumping dew droplets. This fundamentally new mode of pathogen transport is yet to be fully understood at the same scale as we know wind or rain-induced fungal spore transport. In this work, we try to fill the knowledge gap by answering questions such as whether the surfaces with the abilities of gravity-independent jumping-induced droplet removal ironically fail to gravity and how far can spore(s) travel engulfed in a jumped droplet.

But it is not just water droplets (or particles collected by water droplets) on a surface that we want to get rid off. The solid phase of water, *i.e.*, ice or frost, when formed on regular surfaces, is actually harder to remove. The common ice-preventing surfaces are generally unable to stop complete frost formation and forces us to use salt or other moisture attracting chemicals to remove ice from a surface, knowing very well what is the economic and environmental cost of these chemicals. Here, we have introduced a novel de-icing mechanism by holding only a

[1] **Lit.** stain, **Fig.** mess

drop of water over a sheet of frost. The simplicity of our experimental setup may remind you the home physics experiments we all did in our childhood.

We finish our discussion by designing a slippery surface from regular polymer films used in food packaging. Although the idea behind these slippery surfaces has been around since 2011, polyethylene films have never been used to make such surfaces before. Here, we show through extensive characterization that by choosing a suitable lubricating oil and a polyethylene-based film, we can finally get all of our ketchup to slide out of their packets, without struggle.

If the future design of superhydrophobic condensers, de-icing constructs, or slippery surfaces benefit from the work reported here, may be I can finally say with certainty, "*Daag Achhe Hain (Dirt is good.)*."

ভালো থেকো ঠাকুমা, ছোট কাকা

Acknowledgments

...And among that billion minus one
Might have chanced to be
Shakespeare, another Newton, a new Donne—
But the One was Me.

Fifth Philosopher's Song, Aldous Huxley

I will soon go back to the "Old school" acknowledgement pattern of thanking people, I promise; but before that, before the flurry of faces whom I have met in this journey make me forget how I ended up in this path, let me start at the beginning and thank my *Privileges*. Being born as an upper caste, male child from the faith of the majority, opened a lot of doors for me without much struggles. For all I know, even being a solid 10 in the Fair and Lovely fairness meter might have helped me in a country obsessed with fair skin tone. Even if I really do want to live in a world where your gender or race or caste or religion or skin color will no longer decide your life choices, I still have to acknowledge their existence as they dictated my thoughts and actions so far and will continue to do so (I could've just written the term *unconscious bias* to describe this here, but decided to use 10 times more words).

I was not supposed to be here. Sure, I wanted to be back in academia after a 2 years hiatus, but I was not even thinking about pursuing a PhD. It was Nath[2], my friend from *Jadavpur*[3], who persistently talked to me and finally convinced me to apply to PhD programs in the US. I will not forget those 3 or 4 hour long talks we had on the phone where discussion (mostly him talking) would range from movies to what research he recently found interesting. He taught me how to read research papers, edited my statement of purpose and helped me with the application process. But what he did not teach me, but I learned by watching him, is to be curious and to think and think. Although he is the gifted one in this particular sense and no amount of training would ever take me there, it is comfortingly inspiring. His carefree approach to research helped me calm my nerves in that dreaded first year of grad school.

I was not supposed to be here, had it not been for Jonathan. He took me in his lab, realizing very well that I will be starting with a clean slate and will take a considerably longer time to get a foothold in the research field. I know he detests gambling, but I will always be thankful

[2]Saurabh Nath. No he is not like James Bond, it's just that he is known as Nath to us

[3]❤️

to him for taking a chance with me. I will miss his enthusiasm with littlest of findings in our lab, his favourite "NIFI Dundies" and most of all, the ease with which I could talk to him from day one.

I might not have been here, without the people of Blacksburg. They may not have realized this, but it is them who pulled me out of a darkness. I wandered there for more than a year but they are the ones who did not let me wander off. A few lines about you in these pages will never convey the connection I have with all of you. But I will still do it[4] so that when the time (of boredom) comes[5], on one lazy evening in Cascade Ct., someone can start to read it for entertainment[6].

But before that, let me first thank my committee members, Prof. Jiangtao Cheng, Prof. David Dillard, Prof. Robert Moore and Prof. Anne Staples. When I look at their careers and the hardships they went through, I really feel humbled. The ease with which all of them approaches a problem and to see it in front of my eyes has been a delightful experience. I am really grateful to all of you for agreeing to be on my committee and helping me getting this dissertation here.

When I landed in Roanoke, fresh off the flight, apart from Nath, another known face was Shantanab's (from *Jadavpur*). His eagerness to help me as I was slowly adjusting to the life in the US, I initially put it on our acquaintance. Soon, I would find out that regardless of whether he knows someone or not, he is always eager to help people. I am equally glad to have him as my friend and to have survived some of his jokes.

Sreeya'di[7], the "classiest" roommate I have had who also had a novel-sized life stories[8]. With me, you were always the quickest to fight with[9] and quickest to mend it. Hopefully that will continue and I will continue to use your story of *becoming an architect from an economist* for bragging in random places.

Poorna'di, my only friend with a real knowledge of disease epidemiology[10]; another person with whom I have had the most random heated arguments and then in the next moment, we were getting drunk together. Here's to a future where I am eating the *actual Rosogolla* that was promised. Hopefully, by this point, you have also noticed that your name is behind Sreeyadi's. And hopefully, Gupta'da 's apple watch is screaming to him to get out of the dangerous levels of noise zone.

Speaking of Gupta'da, the person with seemingly endless knowledge of everything, is also the person who taught me to drive. While I can never possibly repay the debt (not only for teaching me driving, but also for the endless addas here and in Kolkata, those Jacques

[4] No need to thank me
[5] very rarely
[6] baffling, I know!
[7] Freud Lite
[8] it took a car ride from Niagara to Blacksburg to scratch the surface of it
[9] I started it *most* of the time
[10] which surprisingly came in handy in the last year or so

Pépin omelettes, those melt-in-your-mouth steaks and so on...), as *Gurudokkhina*, I have graduated two students from my unauthorized driving school.

It was just one year, but so much happened between Fall 2016 and 2017, I can't even remember certain days. But I remember Prasen'da. I remember him as this elder brother in my very first trip to Shenandoah and as someone who always had stories to share. Even the most mundane things he would say would sound interesting as he channeled his inner *Tarini Khuro*. I missed him a lot throughout my stay here. But thanks to his efforts mostly, we have kept in touch and I hope we will continue to be in touch.

Hiya, thank you for including me in a tiny part of your life. I enjoyed every moment of it. I wish that you *open all the happiness*™[11] in life.

Shuchi - one of the most creative persons...I am kidding! No you are, but not what I will remember you with. I will remember you as my longest flatmate with a knack for making a full course meal out of nowhere, for all the cocktails and herbal concoctions, for all the trip plannings[12], the very-late-night addas where inevitably, your unrequited love for power electronics and dogs would come up.

AK Paul[13], sorry for the jab[14] in the last paragraph. But I only did it to prove my earlier point that people of Blacksburg (myself included) would read *anything* when bored. Now that you are starting a new life in India as a professor[15], let me use this small space as a time capsule which your students might one day open to find out what a wild party person you were when we were here. Keep making Vegans of Bengal proud with your innovative soybean dishes!

Srijanda, thank you for the countless sensible and non-sensical addas at our place, your place or on the downtown sidewalk[16].

For the first year, it was just Shreyadi and Gabluda with whom I spent an awful lot of time, of course with the constant flow of snacks and tea from their kitchen. Then we got another reason to go there and just stay the weekend without any prior planning. And the reason was Niharika, the youngest member of our *Pahaartowlir Loop*. Thank you for tolerating all of our sudden visits and nuisance over the years. As I am leaving, Shreyadi is starting her 2^{nd} PhD program after already getting 2 Master's and one PhD degree[17]. I wish her all the success and hope to see Niharika becoming the first woman POTUS.

[11] Coca-Cola

[12] I hope to see more of that now that all of us are starting to live in different parts of the country

[13] Arnab Kumar Paul, Virginia Tech, PhD 2020, CS Dept.

[14] though in MCU, this will be called an Easter Egg

[15] BITS Pilani, Goa Campus

[16] Also, sorry for saying "tenure pawa chaap eibhabe party korte thakle" to Prasenda back in 2016. I did not mean it because I knew you will (or already have).

[17] Sheldon who?

GB[18], the soon-to-be millionaire friend of ours, thank you for inspiring me with the amazing photos that you always take. I wish the Pacific[19] is as blue as Arit's wardrobe.

Before the judgement comes, there's so much more to Arit[20] than his wardrobe. You are probably the kindest and most unpretentious person I have met in my life with a mind which is equally efficient in writing research papers at will, ordering chicken wings, managing confusing splitwise bills, and finding out the dirtiest possible humor in an apparently SFW conversation. Do not change. The world should be full of people like you.

Esha[21] thank you for enthusiastically taking part in all the drunk talks when the only two souls awake were us. I wish we could've talked earlier (and without the blood alcohol), but this was the only way it was meant to be[22].

Shadab Towqir, the sleeping beauty and the harshest critic of fish dishes, here's to few more painful graduate years beyond which all the happiness awaits you.

Debasmita, my seasonal roommate, with whom I managed to fight a surprisingly large number of times in a span of just two years. I don't regret those fights because I know those were meaningless (and have already forgotten the first few). A part of what I will remember from the last two years are the kabobs and the daals[23] you made, Jägermeister which you introduced in our party and those out-of-the-blue late nights in your apartment.

I am also grateful to all the labmates I had in NIFI. Had I not come here, I would not have known how people from different parts of the world with vastly different languages, culture, background can work without any conflicts. Farzad, thanks for teaching me everything I know of experimental research and for the persian foods you shared over the years. I owe you a homemade biryani[24]. Weiwei, my world-travel partner[25] with an insane work ethic; you seriously inspired me and at times gave me impostor syndrome. Kevin, I will miss your quips and insightful comments in the weekly meetings. Hyunggon, our very own Terrence Malick with camera, thanks for teaching me what you do best and also introducing Korean movies, memes and shows[26] to me. And then among the late-comers to the lab, Yash has become a very good friend of mine in this short period even with the lab closure for more than half a year; Thank you for taking care of the projects we started. Thanks to all the undergrads (who were really grads in disguise) and other grad students who have been part of this wonderful lab, which in my belief should be the poster child of UNESCO for world harmony and peace.

[18] Arjun Saluja, sorry, Chiranjib Saha
[19] from your balcony view
[20] Student #2
[21] Student #1
[22] unrelated, but *that* Dosa chutney was amazing, never heed to the haters
[23] Shuchi's favourite
[24] Not Beryani, the food from your city. You owe me that one.
[25] China and Italy tour
[26] I am sure Signal is amazing!

Flashback scene, imagine B&W if you want from here on: I would like to introduce some characters integral to the story here. Nirmalya, my *oldest*[27] friend; thank you for choosing to sit with me when I did not have any friend at school. I always wanted to go to your house, be it your birthday or other times, because you had a family full of people and I felt they are also my relatives! I know you remember much more of the last twenty years of us with your elephant-like memory, but I sincerely have to try really hard to find memories where you are not there. Sourav[28] and Rituraj, part of our notorious gang in school, thanks for sticking around even with all the business and other happening social circles in your lives.

And finally, my family of India, my *Maa, Baba, and Dada* who were kind of forced to love me and will keep on doing it regardless of what I do or become. This unconditional love of theirs is what draws me to Kolkata. This is the same mental comfort which I used to feel during those countless nerve-wrecking exams knowing that at the end of it, *Maa* would be waiting for me behind the metal gate. I used to dread *Baba* when I was a kid, but as he and I grew older together, I started to see his softer side. My knack for reading books or writing stories is what I inherited from my *Maa* and from *Baba*, the most knowledgable person to that kid version of me, I got my habit of reading about stuff of the world. Growing up with *Dada* and seeing him become this amazingly caring, down-to-earth, responsible, full-fledged adult human being has been no less wonderful of an experience than watching a Richard Linklater movie.

On that note, is this a *dream sequence* or is it *real*?

[27] not by age, by the length of time
[28] thanks for all the *double carry*

Contents

List of Tables

List of Figures

Symbols

α	Angular orientation
F	Force
E_{i}	Elastic modulus of ice
ΔE_S	Work of adhesion
h_c	Heat transfer coefficient (convection or phase-change)
h, H	Height
k	Thermal conductivity
p	Pitch or distance between two adjacent micropillars
P_v	Saturated vapor pressure
q	Heat flux
T	Temperature
T_w	Temperature of cold plate or the surface attached to it
T_∞	Ambient temperature
S	Degree of supersaturation, given by the ratio RH$P_{\mathrm{sat}}(T_\infty)/P_{\mathrm{sat}}(T_w)$
r_c	Critical nucleation radius of liquid condensate
r_{col}	Radius of same-sized drops (before coalescence)
R, r	Radius of curvature of a liquid drop
Re	Reynolds number
R_g	Ideal gas constant
M	Molar mass
t	Time
ΔT	Degree of subcooling
V	Volume of a liquid droplet
$\hat{\alpha}$	Coefficient of dropwise condensation
ϵ	Surface coverage of dropwise condensate
γ	Liquid-vapor surface tension (otherwise, subscripts will denote)
l_c	Capillary length of water
μ	Viscosity of liquid
ϕ	Solid fraction of a roughened surface (projected roughness area divided by projected basal area)

r	Surface roughness (actual surface area divided by projected basal area)
ρ	Density of liquid
ρ_v	Density of saturated water vapor
θ_a	Intrinsic advancing contact angle of a liquid drop on a smooth surface
θ_A	Advancing contact angle of a liquid drop on a surface
θ_R	Receding contact angle of a liquid drop on a surface
θ^*	apparent contact angle of a liquid drop on a rough surface

Abbreviations

AFM	Atomic force microscope
ESEM	Environmental scanning electron microscope
SEM	Scanning electron microscope
SHPB	Superhydrophobic (ultra water-repellent surface).
SHPL	Superhydrophilic (ultra water-absorbant surface).
NCG	Non-condensable gases
CAH	Contact angle hysteresis
SLIPS	Slippery liquid-infused surfaces, also called:
LIS	Liquid-impregnated surfaces
RH	Relative humidity
HVAC	Heating, ventilation and air conditioning

Subscripts

max	Maximum
sat	Saturation
col	Coalescence

Attributions

Several chapters of this thesis include material already published in peer-reviewed journals, as detailed below.

Chapter 3: Effect of Surface Orientation on Jumping-Droplet Condensation

Originally published as: How Surface Orientation Affects Jumping-Droplet Condensation, Ranit Mukherjee, Austin S. Berrier, Kevin R. Murphy, Joshua R. Vieitez, & Jonathan B. Boreyko, *Joule*, **3**, 2019, 1360-1376, DOI: 10.1016/j.joule.2019.03.004.

J.B.B. conceived the research. A.S.B., J.R.V., and R.M. carried out the experiments. K.R.M. and R.M. analyzed the images. R.M. and J.B.B. interpreted the results and developed the theoretical modeling. R.M. and J.B.B. wrote the manuscript. All authors proofread, added comments, and approved the manuscript.

Chapter 4: How Jumping-Droplet Condensation Spreads Fungal Disease with the Help of Wind

Accepted as a journal article: Synergistic dispersal of plant pathogen spores by jumping-droplet condensation and wind, Ranit Mukherjee, Hope. A. Gruszewski, Landon. T. Bilyeu, David. G. Schmale III, & Jonathan. B. Boreyko, *PNAS*, 2021.

D.G.S and J.B.B conceived the research. H.A.G cultivated the wheat plants, inoculated the samples and prepared the fungicide. R.M and L.T.B performed the experiments and analyzed the data. R.M and J.B.B developed the theoretical modeling and prepared the manuscript. All authors proofread the paper, made comments, and approved the manuscript.

Chapter 5: The Curious Case of Jumping Frost

Originally published as: Electrostatic Jumping of Frost, Ranit Mukherjee, S. Farzad Ahmadi, Hongwei Zhang, Rui Qiao, & Jonathan B. Boreyko, *ACS Nano*, **15**, 2021, 4669-4677, DOI: 10.1021/acsnano.0c09153.

S.F.A. discovered the jumping frost phenomenon. S.F.A. and J.B.B. conceived the research. R.M. and S.F.A. designed and carried out the experiments in the laboratory and walk-in freezer. R.M. and S.F.A. analyzed the data. H.Z. and R.Q. performed the numerical analysis.

R.M., S.F.A., H.Z., R.Q., and J.B.B. developed the theoretical analysis. R.M., S.F.A., and J.B.B. prepared the manuscript. All authors proofread the paper, made comments, and approved the manuscript.

Chapter 6: Oil-Impregnated Hydrocarbon-based Polymer Films

Originally published as: Oil-Impregnated Hydrocarbon-Based Polymer Films, Ranit Mukherjee, Mohammad Habibi, Ziad T. Rashed, Otacilio Berbert, Xiangke Shi & Jonathan B. Boreyko, *Scientific Reports*, **8**, 11698 (2018), DOI: 10.1038/s41598-018-29823-7.

J.B.B., O.B. and X.S. conceived the research. All authors developed the experimental set-up. R.M., M.H., and Z.T.R. conducted the experiments. R.M. and J.B.B. conducted the theoretical analysis. R.M. and J.B.B. wrote the manuscript.

Chapter 1

Background Information

1.1 The process of condensation

We will start with a story. A story that involves condensation, violent jumping, and spores. All of which (and some more) will be part of this dissertation. The story (probably) starts in the late 19^{th} century when a mycologist, Victor Fayod, first noticed the formation of a small droplet near the base of certain basidiospore [1], just before they are forcibly discharged into the air. We will find out much later that this happens with most basidiospore discharge, also called ballistospores due to their violent discharging process. Unfortunately for Fayod, the recognition for this discharging process went to Buller, who was the first to extensively study the so-called "droplet mechanism" of spore discharge [2]. Although he found out that the droplet is responsible for the discharge, he could not figure out its exact role on the discharge process. It was found out much later that this droplet, now of course, called Buller's drop, forms via condensation of water [3, 4]. The relative humidity in regions of fungal growth is rather high which is helped by the hygroscopic chemicals secreted by the spore. Apart from the Buller's drop, on the surface of the spore itself, a lens of condensate forms. Once the Buller's drop and the droplet on the spore coalesce, the violent discharge (estimated acceleration of about $10{,}000g$) occurs as the loss of kinetic energy is sufficient to provide the extreme kinetic energy. The cartoon in Figure 1 might be better at explaining the whole ballistospore discharge process.

Now that we have introduced all (almost) the necessary concepts: spore dispersal, condensation of water vapor, and surface tension-induced jumping droplets, we will build upon them in the next few sections.

1.1.1 Evolution of condensation

Condensation is a common phase change phenomena occurring so frequently around us that we do not think of how complex the process of "breath patterns" formation on a variety of surface is [5]. There is an energy cost associated with the formation of a convex liquid droplet shape from the ambient vapor phase. The first step is the formation of a stable nanometric liquid droplet which will not be evaporated. For this, the free energy of the vapor phase has to be more than the energy of convex liquid-vapor surface formation. The total change in

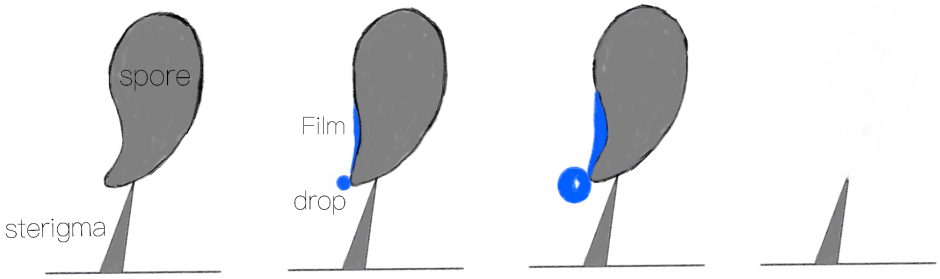

Figure 1.1: Ballistosporic discharge. Diagram for the ballistosporic discharge in some basidiomycetes. The actual spore grows on sterigma. Just before the discharge of the spore, a droplet, called Buller's droplet forms on the joint between the spore and the sterigma. While this droplet grows *via* continuous condensation, a film of water condenses on the spore surface above the sterigma. The violent discharge occurs when the Buller's droplet coalesce with the film of water on the adjacent spore surface.

free energy associated with the change of phase from vapor to liquid for a volume of gas V is $W = 4\pi\Delta e R^3/3$, where Δe is the change in volumetric free energy and R is the radius of the corresponding water droplet. The energy cost associated with the liquid-vapor surface formation is $8\pi R\gamma$. We can now find out the critical radius R for a nucleating water droplet which corresponds to the maximum total energy of formation of a small liquid droplet from vapor phase. The total energy of formation is:

$$W = -\frac{4}{3}\pi R^3 \Delta e + 4\pi R^2 \gamma. \tag{1.1}$$

For the maximum W,

$$\begin{aligned} \frac{\partial W}{\partial R} = 0 = -4\pi R^2 \Delta e + 8\pi\gamma \\ 4\pi R^2 \gamma = 8\pi\gamma \\ R^* = \frac{2\gamma}{\Delta e}, \end{aligned} \tag{1.2}$$

where R^* is the minimum radius required for the embryo to grow (not collapse).

For water, at normal temperature and pressure, this value is about $R^* \approx 1 - 10\,\text{nm}$ [6]. But knowing the stable nucleating droplet size is only part of the story, as the nucleated droplet has to continuously grow by vapor diffusion from the ambient. If such a nucleating droplet forms on a space which is at an ambient relative humidity of 100%, it would evaporate instantly. This is because the vapor pressure just outside a curved droplet, p_r is different from the vapor pressure above a flat surface, p_∞. This relation, for a droplet of size r, was

provided long ago by Lord Kelvin [7] and later, written in the form below by a PhD student, Robert von Helmholtz in his dissertation [8]:

$$\ln\frac{p_r}{p_\infty} = \frac{2\gamma M}{r R_g T \rho}. \tag{1.3}$$

For an ambient temperature of 20 °C or $T = 293\,\mathrm{K}$, $\frac{p_r}{p_\infty} \approx \exp(1.09 \times 10^{-9}/r)$. For a droplet of size between 1-10 nm, p_r is generally more than p_∞, but not by much. Thus, for a droplet to not evaporate after nucleation, the supersaturation has to be proportional to $\frac{p_r}{p_\infty}$ which increases exponentially as r decreases [9]. In fact, for the formation of a nanometric droplet the supersaturation needed is about 3 which becomes 235 for a droplet of size 2 Å. Thus in normal conditions, any small nucleating droplets in space (homogeneous) will evaporate instantly. But we know from our experience that water condenses on surfaces around us at much lower supersaturation (or much higher ambient temperatures). This is because nucleation of a droplet in all of these and most cases occurs on either a macroscopic flat substrate or microscopic foreign particles. This reduces the energy spent on creating a liquid-vapor interface drastically as now we don't need to worry about creating a complete sphere which is the case if the nucleus is forming in a bulk. This is why it is easier to form condensing droplets on hydrophilic surfaces (lower contact angle) than on hydrophobic or superhydrophobic surfaces.

The difference in the nucleation rate between these two modes of nucleation becomes much more apparent for the case of "soda geysers" (Fig. 1.2): formation of carbon dioxide bubbles *via* homogeneous nucleation within the liquid bulk is energetically costly. But most of the de-gassing occurs due to few pre-existing bubbles which act as nucleating surfaces (heterogeneous nucleation) for carbon dioxide bubbles to form and escape the liquid. This is a slow process. If we now drop a Mentos into the soda, the millions of surface cavities in the mentos introduces millions of sites for nucleation and forms the violent geyser of buoyant bubbles.

That the energy barrier of heterogeneous nucleation during vapor to liquid phase change is dependent on the droplet and substrate contact angle, we see different condensation patterns on surfaces (Fig. 1.3). If the contact angle is near zero, such as for glass and clean metal surfaces, the water forms a film (filmwise) which appears dark to us. For non-wetting substrates such as wax-coated natural and artificial surfaces or teflons, nucleation occurs as discrete drops (dropwise) which can scatter lights and thus we see the familiar sparkling dew droplets on grass. In fact, during the early years, it was thought that metal surfaces such as gold, silver are natural surfaces for promoting dropwise condensation. But it turned out that over time metal substrates are covered with fatty impurities which makes them more non-wetting than their cleaner counterparts. On this note, it should be mentioned that surfaces which only shows filmwise condensation can also promote dropwise condensation if the condensing liquid is changed from water to a higher surface tension liquid. Back in the 70's, investigations on the condensation of mercury vapor on metal surfaces showed

Figure 1.2: Physics of soda fountains. When mentos meet soda water, the rough asperities on the mentos provide millions of spots for the carbon dioxide bubble formation. The result is the violent eruption of bubbly soda water as the bubbles all try to escape together once the soda cap is opened. The rightmost eruption is almost 3 m high. Image courtesy: K. Shimada, wikimedia commons.

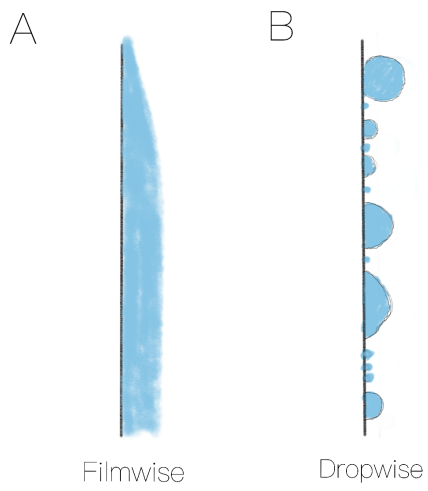

Figure 1.3: Two most common modes of condensation. (A) Condensation on most clean metals or glass or other hydrophilic substrates. A thin layer of condensate is formed on the surface in this mode of condensation. This severely hinders further heat transfer from the ambient to the surface. (B) Enter a more efficient mode of condensation where instead of a thin films, condensates form discrete droplets.These droplets eventually coalesce and frees up more area for further condensation, thereby increasing the heat transfer.

continuous dropwise condensation as well as jumping-droplet condensation [10] (Fig. 1.4), much before it was discovered that superhydrophobic substrates can promote the same effect with condensing water [11].

From a practical viewpoint, dropwise condensation are much more desirable than filmwise condensation, especially on heat transfer devices [12]. This is because in filmwise condensation, the entire surface is covered with low conductivity water which inhibits the latent heat transfer from the vapor to the substrate. In dropwise condensation, on the other hand, the condensation occurs as discrete droplets leaving spaces in between them for further nucleation. After the initial growth from direct vapor condensation, the droplets grow larger *via* coalescence which always reduces the wet surface area. This is also the reason why constant surface coverage by the condensing droplets is typical to continuous dropwise condensation (Fig. 3.7). This directly leads to the realization that if the free space between condensing droplets are increased, that will act as nucleation sites for more condensation and better phase change heat transfer will be achieved [13]. In fact, it has been shown that the heat transfer coefficient of a condensing surface increases exponentially as the maximum condensate size on the surface is decreased [14]. But in reality, due to surface defects or design constraints, not all the condensates can be removed from the surface which eventually flood the surface resulting in inferior filmwise condensation [15].

Continuous droplet removal can be passively achieved using gravity, such that condensates

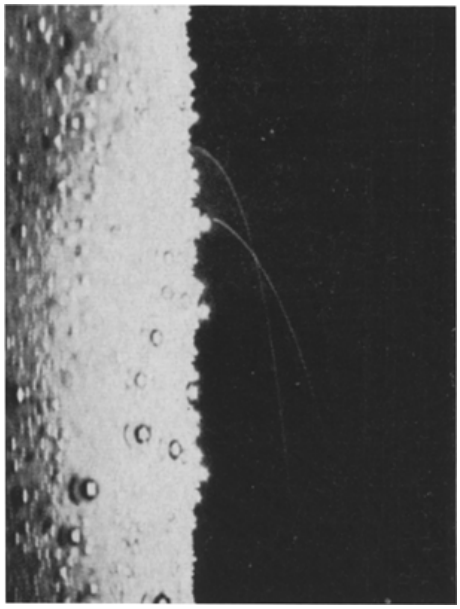

Figure 1.4: Mercury jumping. Condensation of mercury vapor on a steel surface resulted in dropwise condensation. The droplets jumped off the surface after coalescence. The figure is taken from a seminal study by M. Kollera and U. Grigull on the bouncing off phenomenon of condensing mercury droplets. Reprinted here with permission from [10].

reaching the capillary length (length-scale where surface tension balances the weight of the droplet) will slide down the surface [15]. Active mechanical vibration [16] or wind shear force [17, 18, 19] have been employed to remove droplets from a surface at small scales. For the passive gravitational removal, for a long time, the focus has been on finding a durable "dropwise promoter" whose job would be to make the surface hydrophobic, *i.e.* decrease the adhesion or contact angle hysteresis. As most of the coatings failed over a long time of condensation, increasing their thickness was the only way to increase their durability [13]. But the cost of increasing thickness was less efficient heat transfer. Later, with the advent of superhydrophobic surfaces which are even better in repelling water droplets at smaller scales, it was thought that finally the deadlock has been broken. Unfortunately, due to the nanometric size of the nucleating condensates, they tend to grow from within the textures of these surfaces resulting in impaled droplets which are even harder to remove via gravity [20]. But not all hope is lost with superhydrophobic surfaces, as we will see in the next section.

1.1.2 Jumping-droplet condensation

We talked about jumping condensates in the previous section while talking about the condensation of mercury vapor on steel surfaces. About 40 years later, Boreyko and Chen would find that jumping droplet condensation is possible with water vapor also [11]. Their surface was

a hierarchically structured (*i.e* micro-posts with nano-roughness on them) superhydrophobic surface where water vapor condensed as discrete and almost spherical shaped droplets. Once two or more such droplets coalesced, the total surface area and consequently the total surface energy decreases. This excess surface energy for the coalesced droplet supplies the jumping velocity, v, normal to the surface as in below-

$$\begin{aligned} \gamma R^2 &\sim \frac{1}{2}\rho R^3 v^2 \\ v &\sim \sqrt{\frac{\gamma}{\rho R}}. \end{aligned} \tag{1.4}$$

But this energetic viewpoint tells us nothing about the process before the jumping and how the surface and droplet interaction plays a role in the jumping. Figure 1.5 is a sketch for the whole process [21]. As the two spherical droplet grows, they eventually touch each other and a liquid bridge is formed above the surface. The quasi-spherical shape of the droplets ensure that the liquid bridge forms above the surface. The bridge keeps growing and hits the surface once it grows beyond the droplet size. The very low adhesion of the superhydrophobic surface ensures that the bridge does not get stuck on the surface. Rather, it exerts a reaction force on the bridge and the droplet is propelled upwards. We can explain the jumping of the mercury condensates on the steel surface via the same logic as mercury contact angle on metal substrates is very high as well as their mobility. Although the jumping-droplet condensation was first observed on artificial superhydrophobic substrates [11, 22], later reports have come out to show that even natural surfaces like cicada wings [23], and wheat leaves [24] all exhibit this phenomena with some interesting effects.

Usually droplets with diameter in the order of 10-100 μm has been observed to be participating in the jumping events [11, 22, 25]. But even smaller droplet departure size of 500 nm has been reported in literature [26]. Due to such extremely small droplet departure size, jumping-droplet condensation is about 30% more efficient than regular dropwise condensation [22]. Moreover, as the jumping event itself is a capillary-inertial event with no gravity-dependent terms, it was long thought that the performance of a condensing surface exhibiting jumping-droplet condensation would also be independent of surface orientation [27, 28]. We will see in Chapter 3 when this common understanding fails.

1.2 The road to liquid-infused surfaces

The first mention of superhydrophobicity was back in 77 AD, by Pliny the Elder, a naturalist in the Roman empire [29]. He saw beads of water on some wooly plants which we now know, is a feature of superhydrophobicity. But, proper characterization of artificial patterned superhydrophobic surfaces became available only at the end of the 20^{th} century [30, 31]. After

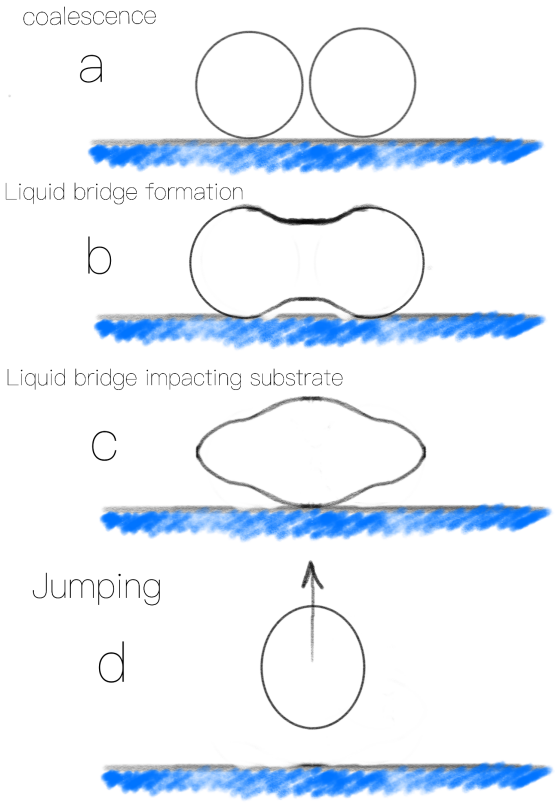

Figure 1.5: Steps for jumping-droplet condensation. (A) Two micrometric (lowest size generally varies within 2-10 μm) droplets coalesce on a nano or hierarchically-textured surface. (B) Formation of liquid bridge above the surface. (C) Impact of the bridge on the surface. (D) The reaction force exerted by the surface on the droplet propels it upward.

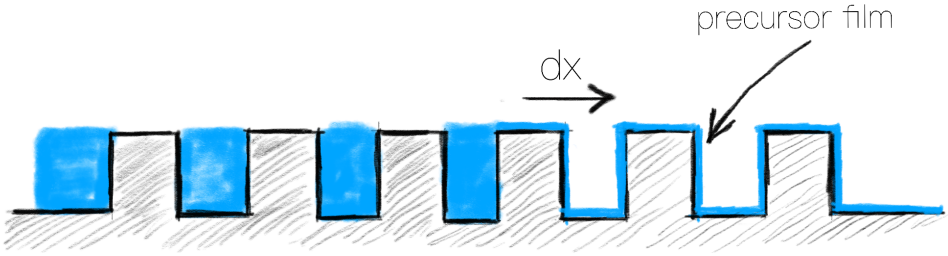

Figure 1.6: The hemiwicking process. Roughness, here modeled with square posts, enhances the affinity of a liquid to a solid substrate. A liquid which wets or spreads on a flat solid, would invade the air pockets within the roughness and replace the solid-vapor interface with a solid-liquid and a liquid-vapor interface. This is the basic of hemi-wicking. A droplet placed on such a textured solid would first impale the texture just beneath and then would sit on a composite of solid and liquid with a contact angle less than that in an Wenzel state.

the advent of modern manufacturing techniques, making a surface superhydrophobic has become as easy as spraying with a solution containing millions of nanoparticles [32]. Whether made through advanced photolithography techniques [25] or by a $10 colloidal solution, all superhydrophobic surfaces work on the same principle [29]: if we increase the roughness of an already hydrophobic solid, due to the air trapped within these roughness, a drop of water will sit on a mixture of solid and air, further reducing the surface energy of the combined surface. This is called the Cassie state of wetting. Once superhydrophobic surfaces became more common, the next decade saw a wave of research that went into understanding their low adhesiveness, potential heat transfer and self-cleaning applications, as well as limitations. But soon we realized that the air pockets which make the superhydrophobic surfaces extremely water repellent are the very reason of their downfall. Impacting droplets or hydrostatic pressure can displace the air from the pockets and impaling the structures in the process. The micro and nano-structures are also very prone to damage and clogging via impurities which increases adhesion locally. This is why even after more than 20 years after their introduction, the use of superhydrophobic surfaces in practical applications never caught on. It was necessary to find an alternative durable omni-repellent surface. It turned out the answer was in front of us all along.

About 100 years before the famous Kao corporation reports which kickstarted the whole research on superhydrophobic surfaces [30, 31], Wenzel proposed a relationship [33] between the apparent contact angle of a droplet on a textured solid (θ^*) and the equilibrium contact angle (Young's angle) on a flat solid of the same material (θ) as $\cos\theta^* = r\cos\theta$, where r is the roughness ratio of true surface area over apparent surface area. As r is always greater than 1 by design, we can readily see what we described in the last paragraph: a hydrophobic surface ($\cos\theta < 0$) will become more hydrophobic and a hydrophilic solid ($\cos\theta > 0$) will become more hydrophilic when roughness is introduced on a flat solid. On such a textured hydrophilic solid, a drop of water will instantly impale the underlying textures forming what is known

as the Wenzel state. But another interesting wetting state can be seen on rough hydrophilic surfaces where not only the structures just beneath the droplet is impaled (Wenzel state), but the liquid invades into the underlying textures beyond the three-phase contact line of the droplet and the droplet sits on a composite structure of solid and liquid [34],. If this wetting process sounds similar to wicking inside a porous solid such as a sponge or a paper towel, that is because a solid surface decorated with textures is a two-dimensional approximation of a three dimensional porous medium [35]. But the similarity ends there. When a liquid invades a porous solid, it replaces the one phase (solid) with another (liquid). The criteria for this case is *i.e*, $\gamma_{SV} > \gamma_{SL}$. From Young's equation, $\gamma_{SV} - \gamma_{SL} = \gamma \cos\theta$ which means for any $\theta < 90°$, a liquid will wick into a porous solid. But for the case of a liquid invasion into a textured two dimensional surface, one interface is replaced with two: solid-liquid and liquid-vapor [34]. Such an imbibition process is shown in Fig. 1.6 using a model textured surface made of microposts [36]. In this process, a liquid invades the air pockets within the textures but the top of the posts remain dry making it a partial wetting state. As this is between the complete wetting state on a flat solid ($\theta = 0°$) and wicking ($\theta < 90°$), the term "hemi-wicking" is often used to describe this situation. The condition for hemi-wicking can also be derived from a simple energy balance: when a thin precursor film of liquid is displaced by an amount dx, the corresponding surface energy change is written by, $dE = (r - \phi)(\gamma_{SL} - \gamma_{SV})dx + (1 - \phi)\gamma dx$. Here the first term considers liquid replacing the solid-air interface within the microposts and the second term represent the liquid-air interface energy where the liquid is flush with the top of the posts but the post tops themselves are dry. For better understanding, r is the factor representing total roughness area over the apparent surface area and ϕ_s is the area fraction of top of posts over the apparent surface area. Thus, a precursor film will only progress and fill the cavities if $dE < 0$ which along with the Young's relation, gives us the criteria for hemi-wicking, $\cos\theta > \cos\theta_c$ or $\theta < \theta_c$ where $\cos\theta_c = \frac{1-\phi}{r-\phi}$. Interestingly, both the conditions for wicking inside a porous media ($r \to \infty$ which makes $\theta_c = 90°$) and complete wetting on a flat surface ($r = 1$ which makes $\theta_c = 0°$) can be recovered from the hemiwicking criteria. To summarize, on a hydrophilic solid ($\theta < 90°$), if $\theta > \theta_c$, a liquid droplet will follow the Wenzel rule and invade the roughness beneath the droplet creating a Wenzel state, but the area beyond the drop remains dry. But when $\theta < \theta_c$, the drop exists on a composite: islands of solid and a film of the same liquid with a non-zero angle which is higher than the angle predicted by the Wenzel relation. For any textured surface, *i.e*, a surface with unknown ϕ, the criteria for hemi-wicking is $\cos\theta > 1/r$ [35].

This theory of hemi-wicking would later be used to make certain self-cleaning surfaces which are also much more durable than superhydrophobic surfaces. The impregnating liquid can be chosen carefully to repel specific substances. Generally, oils are popular choice for lubricating liquids. Textured hydrophobic surfaces (*i.e.*, superhydrophobic) are generally completely wetted by oil ($\theta = 0°$), such that the condition of $\cos\theta > 1/r$ will always be satisfied. Thus when such a surface is brought over an oil bath or an oil droplet placed over the surface, oil will propagate into the texture as a thin film until the cavities are completely flushed. Orientation of the surface does not matter for the oil film progression because the main driving

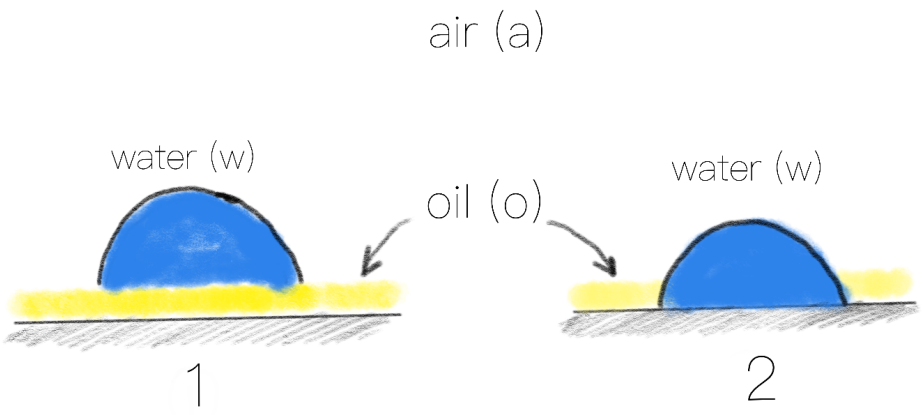

Figure 1.7: Two cases of droplets on SLIPS. A water droplet can stay on a liquid-infused surface in one of two ways: (1) the water droplet sits on top of the oil layer without displacing it or (2) the droplet displaces the oil and touches the solid surface underneath.

force is capillary. These hemi-liquid, hemi-solid surfaces are called slippery liquid-infused surfaces (SLIPS) or liquid-impregnated surfaces (LIS) [35, 37, 38]. These are characterized by an apparent angle close to 90°, extremely low contact angle hysteresis ($\Delta\theta < 1°$), and higher durability to mechanical abrasion or pressure. Figure 1.8 shows a water droplet on a liquid-infused surface. The oil ridges on the side of the droplet arises due to the vertical component of the water-air surface tension force [38, 39]. This same vertical component is also present on a completely solid substrate, but as the solids have higher elastic modulus E, the strain or size of the annular ridges around the droplet is non-existent (as $\delta \sim \gamma/E$). Once a droplet of an immiscible liquid (like water is immiscible in oil) is placed on the liquid-infused surface, two things can happen: the droplet might sink in and touch the micro/nano-textures underneath or it will float on the oil layer with the islands of solid in between [35] (Fig. 1.7). Extreme repellency will only happen if it is the second scenario. Thus we need to find the energy criterion which makes the second scenario energetically favorable. The total surface energy in the first scenario is $E_1 = \gamma_{wa} + \gamma_{wo} + \gamma_{os}$, while in the second scenario the total surface energy can be written as $E_2 = \gamma_{wa} + \gamma_{ws}$. The second situation will prevail if $E_2 < E_1$ or $\gamma_{wo} + \gamma_{os} < \gamma_{ws}$. By replacing the solid-liquid surface tension will liquid-air surface tension (easier to measure), we get the final energy criterion for floating and easy removal of the droplets from the surface: $\gamma_{oa}\cos\theta_1 - \gamma_{wa}\cos\theta_2 - \gamma_{wo} > 0$, where θ_1 and θ_2 are the Young's contact angle of oil and water on a flat solid of the same material. While this criterion successfully predicts whether the droplet of water will float or sink, it can not predict whether oil will cloak the water droplet. An example of a droplet cloaked by a thin oil film is shown in Fig. 1.8. Cloaking is an important issue as oil slowly drains from the liquid-infused surface *via* these cloaked droplets [38]. The cloaking criterion can also be similarly found out by comparing surface energy for the cloaking and no-cloaking case. The surface energy for an oil-cloaked droplet is simply, $E_{cloak} = \gamma_{oa} + \gamma_{wo} + \gamma_{wo} + \gamma_{os}$ and that for a non-cloaking case it is $E_{no\text{-}cloak} = \gamma_{wa} + \gamma_{wo} + \gamma_{os}$. Cloaking will happen if $E_{cloak} < E_{no\text{-}cloak}$ or $\gamma_{wa} - \gamma_{wo} - \gamma_{oa} > 0$. For

durable slippery coatings, we want to choose the surface, the droplet, and the oil combination in such a way that both the criteria for floating and no cloaking are satisfied.

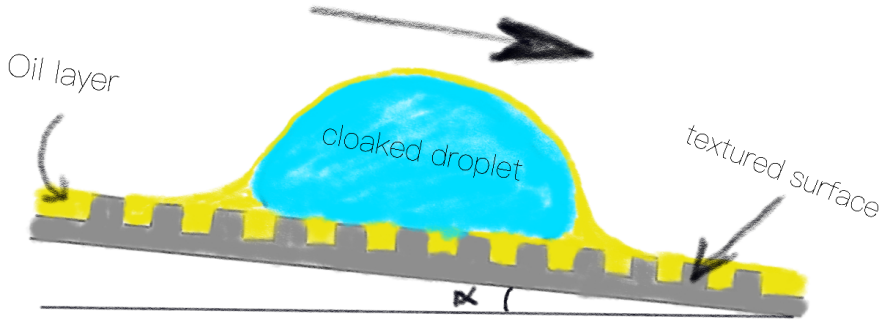

Figure 1.8: Basics of SLIPS. A micro or nano-textured surface forms the basis for SLIPS or LIS. The surface generally is hydrophobic or in other words olephilic, which increases its affinity towards the lubricating oil (yellow). Thus, a strong capillary attraction between the substrate and the thin oil layer is formed. A water droplet (Blue) immiscible in the lubricating oil slides down this super-repellent surface with ease. Also notice the capillary ridges on either side of the droplet which arises due to the vertical component of the water-air surface tension. Also, whether the droplet will be completely cloaked by the oil or not would depend on satisfying an energy criteria.

Numerous manufacturing techniques have been proposed for making such liquid-infused surfaces (a comprehensive list is given in the Introduction of Chapter 7), each with their own sets of benefits and limitations. But, how such a surface is prepared does not affect the characteristics of these surfaces [35]. SLIPS have been made on various substrates with a functional rough layer and by dip coating or spin-coating (which creates a uniform thin film) or by contacting with a reservoir of oil and using gravity or capillarity for propagation. The main objective is finding appropriate lubricating oil and surface combination where the oil wets the surface and the textures on the surface holds on to the thin oil film via capillary attraction. In Chapter 7 we will talk about making such a slippery liquid-infused surface on a hydrocarbon-based polymer film.

1.3 The process of frost formation

There is a 3 min sequence in the Hollywood movie "The Day After Tomorrow" which starts with people running from an invisible threat in a city covered with a thick snow. After a few seconds, we spot the threat: a rapidly moving frost front that, as soon as it touches a surface,

it becomes frozen solid regardless of its initial state. The fabric with the American flag is also not spared from this frost propagation. Eventually our hero stops this seemingly unstoppable frost front by closing the door on its face and burning books to create heat. Thankfully, not all of us need to endure three hours of bad acting, worse background score, and childish at best writing to understand the enormous impact of frost accretion in our lives. Frost accumulation on energy and transportation infrastructures including HVAC systems, power grids, aircraft engines and wings, roads, and buildings not only causes loss of efficiency [40] but can also be fatal in extreme cases. Frost on a solid surface can form in two ways: water vapor from ambient can transform directly into ice in a process known as desublimation. However, in most cases the water vapor first condenses into supercooled liquid droplets, which later freezes into ice. This is called condensation frosting, which requires significantly lesser degree of supersaturation than desublimation. As condensation of droplets precedes frost formation in the second scenario, early research ideas proposed superhydrophobicity as a method to retard frost formation. Apart from the gravity removal of droplets before heterogeneous nucleation occurs on the condensed droplets, nanostructured superhydrophobic substrates also demonstrate droplet removal *via* jumping-droplet condensation.

There are two ways to reduce or remove frost on a surface- the active method uses energy input or hygroscopic chemicals like glycol or salt [41, 42, 43] to remove frost from surfaces once it is formed. Apart from being an energy-inefficient process, the hygroscopic materials lose their hygroscopicity over time as they attract more moisture. Excessive use of salt on roads is also detrimental for the environment. Thus, passive defrosting techniques are being preferred where the main goal is to delay or control the ice nucleation *via* surface chemistry and topography. But it turned out none of these can actually stop complete frost formation on a solid surface. Much like the marching of freeze front in the movie, frost grows on a surface due to inter-droplet frost bridging phenomena where once one droplet freezes on the surface, ice bridges connect neighboring liquid condensates and freeze them. This creates a percolation of ice bridge networks which then start to grow in the third dimension and the whole surface gets covered in a thick forest of frost. Another approach is to reduce the ice adhesion strength of the surface by imparting chemical coatings on the surface itself [41, 44] or impregnating a textured surface with lubricating oil [45]. Much like the use of superhydrophobic surfaces, durability of such low ice adhesion surfaces are still not up to the standard for continuous use [46, 47]. Poulikakos et al. has recently shown a new passive method of removing supercooled water droplets from superhydrophobic surfaces via rapid freezing [48, 49]. But this phenomena is relevant to only low pressure environment which makes it impractical. A more recent study by Ahmadi et al. has shown that the hygroscopicity of ice itself can be used to keep a surface frost-free [50] for an extended period of time. Of course, the constraint is the elevated surface structures in this case where the moisture attracting ice are kept at a higher elevation above the underlying surface which is required to be frost free. In Chapter 6 we will discuss a new passive mode of frost removal by using just water.

Chapter 2

Introduction

2.1 Motivation

(*Inspired by the preface of one of my favorite books: Capillarity and Wetting Phenomena: Drops, Bubbles, Pearls, Waves*)

As you wake up in the early winter morning to look outside, much to your dislike, you found the beautiful view to the horizon (and pearl-shaped dew drops on spider webs and leaves) is obstructed by a foggy glass window. You went to take a refreshing hot morning shower. You come out of the shower only to find again a completely foggy mirror. After your second aargh! moment, you rush to your car to beat the early morning traffic. But you find the car windshield covered in a thick layer of frost which to your surprise, you found to be quite hard to remove by force. On your way to work, you pick up your breakfast with small packets of ketchup. You again face frustration while trying to get all of the ketchup out of those tiny single-use packets.

These few examples from our daily life illustrates the not-so-beautiful effects of capillarity and wetting phenomena and the need to expel different forms of matter from surfaces. Removal of liquid condensates or frost efficiently and effectively from artificial and natural surfaces will not only improve their performance (think about the functional improvement of heat transfer devices or insect eyes due to the removal of droplets or frost), but will also help in saving lives (de-frosting airplane wings is both necessary, and economically and environmentally costly affair). This urgency to remove or repel materials from surfaces is not only limited to water or its solid form, but also to other much stickier and messier fluids like ketchup. Creating an omni-repellent surface from the same materials which were used in the ketchup packets you used earlier could save tons of food products from being wasted if you think about the cumulative waste in a year. But the very effect which help us in getting rid of liquid condensates from artificial superhydrophobic surfaces, enables plant-to-plant fungal pathogen transport among wheat crops. We need to understand the dynamics of such pathogen transport mode to devise a plan to stop the disease spreading.

Not everything we have done here is following a plan or strict protocol. The remarkable jumping frost event that we discuss here is a completely accidental discovery made by a graduate student with a pair of attentive eyes and a mind curious enough to ask questions. As child, when the science behind most of the regular phenomenon were not known to us,

we rejoiced at the most insignificant of events as if we were witnessing magic. It is with the same bewilderment, we approach the problems described here. Our primary motivation is to improve our understanding of several interfacial phenomena which would help us improve future design of antifogging or omni-repellent slippery surfaces or novel de-icing constructs, and also help in mitigating dew-induced fungal pathogen spread among plants. Our secondary motivation is more pedagogical; the theoretical analysis throughout this work often involves simplified systems and scaling analysis to make the physics of the problem more accessible to readers from different fields. Our hope is that this work will inspire them to ask trivial and mundane questions; questions which made all of these works possible.

2.2 Goals and Objectives

The overall goal of this work is to enhance our understanding of several spontaneous or passive expulsion mechanisms seen on a variety of surfaces and for different forms of matter. This can be broken down into three major objectives- we will talk about two different aspects of gravity-independent jumping-droplet condensation on artificial and natural superhydrophobic surfaces, one chapter will be devoted to the understanding of a novel passive frost removal mechanism that manifests itself in close proximity to a water droplet and lastly, our objective would be to design a slippery liquid-infused surface from some widely used hydrocarbon-based polymer films.

Objective 1a: Characterizing Orientation-Dependence of Jumping-Droplet Condensation

Heat transfer efficiency of a condensing surface largely depends on the fraction of total surface area that is covered by the condensates. In dropwise condensation, the condensates are formed as isolated droplets on the surface compared to the formation of a uniform film in case of filmwise condensation. But, over a long period of condensation, the individual droplets grow continuously till they merge or fall off the surface due to gravity, creating fresh spaces for further nucleation in both cases. But for continuous removal, gravity is the only passive mechanism which comes into the picture only when the droplets grow to a threshold diameter ($\approx 3\,\text{mm}$ for most surfaces). But as the heat transfer coefficient of condensation decreases with increasing condensate size, vertical or upside-down condensers perform significantly better than a horizontally oriented one which cannot shed the growing droplets. About ten years ago, a fundamentally new mode of dropwise condensation was discovered on nanostructured or hierarchically structured superhydrophobic surfaces where microscopic condensate spontaneously jump out-of-plane upon coalescence by converting surface energy to kinetic energy. Droplets as small as $2\,\mu\text{m}$ can be ejected from the surface via the jumping removal mechanism. As this mechanism is gravity-independent, follow-up researches assumed that the heat transfer efficiency of the surface would show little sensitivity to the surface orientation. Our first objective in Chapter 3 is to determine how the heat transfer performance and drop-size distribution of jumping-droplet condensation are

affected by systematic variations in the substrate orientation. To determine whether jumping droplets returning to the substrate is beneficial for the subsequent chain reactions (more droplet removal) or detrimental (droplets get stuck), the dynamics and size distribution of droplets on the condensing surface will be compared at horizontal, 45°, vertical, and upside-down orientations. A theoretical treatise will also be provided for comparing the heat transfer performance at different surface orientations.

Objective 1b: Understanding how wind and jumping-droplet condensation synergistically help in the large scale dissemination of wheat leaf rust spores.

Fungal pathogens in plants spread in three stages- liberation of spores from the diseased plant, drift or passive horizontal transport and then finally deposition onto a host plant. The liberation of spores can be achieved via spontaneous ejection from within the fungi body or via passive removal agents such as wind or rain. Recently, one study has shown that wheat leaves, which are superhydrophobic, can demonstrate jumping-droplet phenomenon during a natural dew cycle and leaf rust spores can be liberated with these jumped condensates. Being a relatively new form of passive spore removal mechanism, not a lot is known about it. The objective of this work (Chapter 4) would be to increase our knowledge of spore spreading via jumping-droplet condensation. We will also look into the synergistic effect of wind and jumping-droplet condensation on the range of pathogen dispersal. We also aim to prescribe methods to mitigate disease spreading during natural dew cycles.

Objective 2: Understanding jumping frost phenomena

It was discovered in our lab, quite accidentally, that frost dendrites can spontaneously jump from a substrate when a liquid water droplet or film is brought opposite to it. After performing some preliminary experiments, our hypothesis is that the strong attraction between frost dendrites and the opposing water droplet is a result of temperature gradient-induced charge separation in ice. Here in Chapter 5, we will use simple experimental and numerical methods to gain a fundamental understanding of the charge separation mechanism in ice and frost. Our long-term vision is to show that this technique can be translated to rapid removal of entire ice or frost sheets with a pulsed charge of high voltage, replacing the costly methods of applying heat or antifreeze chemicals.

Objective 3: Designing a slippery liquid-infused surface using a hydrocarbon-based polymer film.

Superhydrophobic surfaces achieve their mythical ability to repel a variety of materials via the inclusion of a lubricating air layer between the surface roughness. But these air layers are also very fragile; they can be penetrated by pressure or lower surface tension liquids making them unsuitable for many applications. Back in 2011, researchers found an ingenious way to achieve similar mobility on a textured surface by replacing the air layer within the surface textures with a layer of lubricating liquid e.g., oil). Stability of the thin oil film is maintained by the capillary force exerted by the underlying hydrophobic micro or nano-textures of the substrate. As long as the surface chemistry (wettability and textures) and the oil compo-

sition are carefully chosen, a stable and durable omni-repellent surface would be achieved. Many studies have since come up with different techniques to achieve the roughness or porosity on the substrate along with variations in the oil layer. But common hydrocarbon-based polymers such as polyethylene (PE) were generally excluded from these discussions as PE is generally considered resistant to impregnation by oils. In Chapter 6, we will establish the design criteria for making slippery liquid-infused surfaces from hydrocarbon-based polymers. We will characterize the surfaces before and after oil infusion as well as test for their durability.

2.3 Organization

In Chapter 1, background information was provided on two main phase change phenomena involving water, namely, condensation and frosting. Chapter 3 is an experimental study which will look into the surface orientation effects on jumping-droplet condensation. Being a gravity-independent (capillary-inertial) phenomenon, it had long been assumed that the efficiency of jumping-droplet condensers would also be independent of gravitational forces. While this assumption does hold for short duration condensation events, for long term condensation, the surface effects start to affect the heat transfer performance. A theoretical subsection is also provided at the end of the paper which shows how the changes in the condensate pattern on differently oriented surfaces lead to a change in the condensation heat transfer efficiency. The jumping-droplet effect can also be observed on natural superhydrophobic surfaces like wheat leaves. A recent study has shown that fungal spores (leaf rust) on a wheat leaf can be liberated by taking a ride with the jumping condensates during a natural dew cycle. In Chapter 4, we show how jumping-droplet condensation enables short range spore dispersal which can be extended spatially with the help of a breeze. Next, we shift our focus from removal of condensates to the removal of frost. In Chapter 5, we try to decode the remarkable frost jumping phenomena opposite to a polar liquid droplet like water. A thorough understanding of this might enable us to design a novel de-icing construct in future. We end our discussion on expelling different forms of matter from surfaces with an experimental study on designing a liquid-infused surface (LIS or SLIPS) from common hydrocarbon-based polymers (Chapter 6). Although about 10 years have passed since the initial discovery of these omni-repellent surfaces, very few reports have mentioned the use of polyethylene for making such surfaces. In Conclusion and Future Work, we report some recent works that are being done or has already been done by us which will hopefully further our understanding of these mechanisms reported here.

Chapter 3

Effect of Surface Orientation on Jumping-Droplet Condensation

"...madness is like gravity, all it takes is a little push."
—The Joker, The Dark Knight

The content of this chapter was previously published as a journal manuscript as an article [51] (How Surface Orientation Affects Jumping-Droplet Condensation, Ranit Mukherjee, Austin S. Berrier, Kevin R. Murphy, Joshua R. Vieitez, and Jonathan B. Boreyko, Joule 2019 3 (5), 1360-1376, DOI: 10.1016/j.joule.2019.03.004), and reproduced here with minor modifications. This chapter experimentally and theoretically investigates the effect of surface inclination on jumping-droplet condensation and associated heat transfer performance.

3.1 Introduction

Vapor condenses on a solid substrate either as a liquid film or in the form of discrete droplets, depending upon the surface energy of the substrate [13, 52, 53]. Dropwise condensation is nearly an order of magnitude more efficient than filmwise condensation [12, 54, 55], due to the considerable thermal resistance of a continuous liquid film. The heat transfer coefficient for dropwise condensation increases monotonically as the critical size of departing droplets decreases, as this maximizes the dry surface area exposed to steam [56, 57]. For conventional dropwise condensation on smooth hydrophobic surfaces, droplets are passively shed by gravity which constrains their departure size to the capillary length (~ 1 mm for water) [57]. Dropwise condensation is therefore well-known to be highly dependent on surface orientation, where a vertical condenser minimizes the departure size and maximizes heat transfer, and vice versa for horizontally oriented condensers [15, 58].

As an alternative to removing large droplets by gravity, condensing micro-droplets can spontaneously jump out-of-plane from nanostructured superhydrophobic surfaces upon coalescence [11]. This passive jumping mechanism serves to decrease the maximum droplet departure size of the condensate by several orders of magnitude compared to gravitationally-driven dropwise condensation [11, 25, 26, 59]. As a result, the heat transfer coefficient of jumping-droplet condensation is at least 30% higher than classical dropwise [22, 60, 61], and can be even higher when using electric fields [62, 63], tall and interconnected nanowires [64], or overlaying hydrophilic features [65, 66].

The mechanism for out-of-plane droplet jumping is the impact of the coalescing liquid bridge against the low-adhesion substrate [21, 67, 68]. For micrometric water droplets, the hydrodynamics of the liquid bridge are capillary-inertial in nature as both the Bond and Ohnesorge numbers are much less than unity, indicating negligible gravitational and viscous effects [11, 26, 69]. Therefore the initial out-of-plane velocity is independent of the substrate's gravitational orientation, which is why all studies to date have only chosen a single orientation to characterize jumping-droplet condensation. A theoretical study by Miljkovic et al. best summarizes the current perspective of surface orientation effects: the calculated heat transfer coefficient increases monotonically as the surface tilts from horizontal to vertical for dropwise condensation, while the heat transfer of the jumping-droplet model remains constant due to an assumption of an orientation-independent droplet distribution [28].

While it is true that the critical departure size of a jumping droplet is orientation-independent, we suggest that there are two reasons why orientation still matters. First, droplets jumping from a non-vertical surface will fall back to the surface due to gravity. The returned droplets can often coalesce and jump again in chain reactions [11, 70, 71], but will eventually grow large enough to become unable to jump. Second, jumping is suppressed if the coalescing droplets exhibit a sufficiently large mismatch in size [72, 73, 74]. In the absence of a gravitational orientation, these stuck droplets will continually grow over time which will diminish the heat transfer.

Here, we show that the droplet size distribution and heat transfer of jumping-droplet condensation are profoundly impacted by the surface orientation of the condenser. A horizontally oriented surface was unable to shed any droplets that became stuck due to gravitational return or size mismatch, resulting in large millimetric droplets after several hours of continuous operation. For partially inclined surfaces, we found that these large, stuck droplets were instead able to roll down the surface upon coalescence-induced dislodging. This new phenomenon is a blend of capillary-inertial and gravitational effects working together synergistically. Finally, a vertically oriented surface minimized the amount of returning droplets in the first place, while retaining the supplemental gravitational removal of droplets stuck due to mismatch. A semi-empirical model was used to calculate the condensation heat flux as a function of the overall droplet size distribution for each surface orientation. Inclined orientations exhibited a 40–100% enhancement in the theoretical heat transfer coefficient compared to the horizontal orientation, due to an order of magnitude decrease in the maximum droplet size. These findings indicate that the performance ceiling of jumping-droplet condensers may be higher than previously expected, further motivating their potential application in power plants, HVAC systems, or thermal desalination.

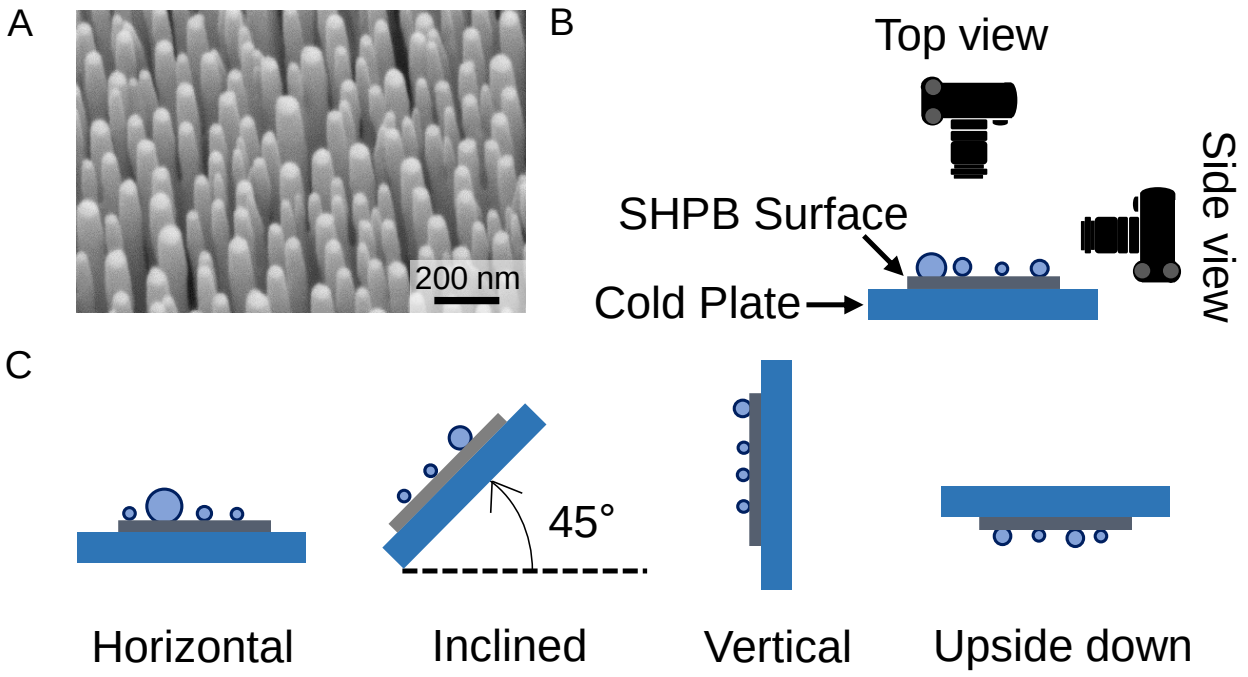

Figure 3.1: Experimental setup. a) SEM image of the silicon nanopillar arrays comprising the superhydrophobic surface used in the condensation experiments. b) Schematic of the experimental set-up. c) Schematic of the condensation experiments in different surface orientations.

3.2 Materials and methods

Superhydrophobic surface preparation.

The nanopillared superhydrophobic surfaces were made in the cleanroom of the Center for Nanophase Materials Sciences at the Oak Ridge National Laboratory. The silicon nanopillars were fabricated non-lithographically by dry etching into a thermally dewet platinum film that served as the etch mask. For more details on the fabrication process, please refer to the previous reports by Boreyko et al. [25, 75]. The nanopillars have a height $h = 531 \pm 6\,\text{nm}$, diameter $d = 69 \pm 8\,\text{nm}$, and center to center pitch $p = 119 \pm 40\,\text{nm}$. The nanopillars were conformally coated with a hydrophobic monolayer by the vapor-phase deposition of trichloro(1H, 1H, 2H, 2H–perfluorooctyl)silane (Sigma-Aldrich). The silicon sample and an open vial of the liquid silane were held within a container on a hot plate set to 70 °C for several hours. Surface characterization was done on a contact angle goniometer (ramé-hart) using the droplet shrink-swell method. The apparent advancing and receding contact angles for water on the superhydrophobic surface was measured to be $\theta_A = 161° \pm 1°$ and $\theta_R = 151° \pm 4°$, respectively.

Condensation Experiments Setup.

The condensation experiments were performed either in the ambient or in a customized humidity chamber (ramé-hart) with the nanostructured surface thermally bonded to a Peltier cold stage (ramé-hart) with the help of a thermal paste (Aavid Thermalloy). The temperature of the cold stage was set at $T_w = 1.0\,°\text{C}$ with an ambient air temperature $T_\infty = 20 \pm 4\,°\text{C}$ and a relative humidity of $RH = 59 \pm 2\%$. This correspond to an average supersaturation of $S = 2.1 \pm 0.4$, where $S = P_v/P_{sat}(T_w)$ is the ratio of the partial vapor pressure of the ambient air and the saturation pressure of water vapor at the substrate temperature. Condensation visibly appeared in the camera images about 30 s after reaching $T_w = 1.0\,°\text{C}$, which corresponds to our definition of time zero for the 3 h growth experiments.

For the horizontal orientation, a high-speed camera (Phantom v711, Vision Research) was used along with a function generator (Agilent, 10 MHz) for capturing top-down images of the condensing surface at 10 s interval for 3 h. For the 45° inclined and vertical orientation experiments, a Nikon D5300 camera attached to a Infiniprobe TS-160, two extension tubes and a ring light (Polaroid) was used. The high-speed videos of the dynamics of the condensate droplets on horizontal, 45° inclined, vertical and upside-down surface orientations were captured from three different angles, e.g., top-down, bottom-up and side view using the high-speed camera (Phantom v711).

Image Analysis.

Image analysis techniques were used to calculate number of droplets within the field-of-view and individual droplet diameter from the time-lapse images of experiments. From these two sets of data, average and maximum droplet diameter over 3 h condensation and surface coverage by the condensates were calculated. Even though images were taken at every 10 s during the actual experiments, to save time, images at 1 min interval were used for all the analyses. Images on the horizontal surface orientation were analyzed with the help of an image processing software (ImageJ). All images were converted to binary images before a droplet edge detection algorithm was applied. For the 45° inclined and vertical orientation images, custom Java codes were used for the image analysis.

Surface Fabrication and Condensation Visualization

Superhydrophobic nanopillars were used for all of the condensation experiments performed here (see Experiments Section for details). Figure 3.1a shows a typical scanning electron microscope (SEM) image, where the roughly cylindrical nanopillars exhibit the following averaged values: a diameter of 69 nm, a height of 531 nm, and a center-to-center pitch of 119 nm. Deposited droplets exhibited an apparent advancing contact angle of $\theta_A \approx 160°$ and an apparent receding contact angle of $\theta_R \approx 150°$, as measured using the shrink/swell method on a contact angle goniometer. The advancing intrinsic contact angle on a corresponding smooth silanized silicon surface is $\theta_a \approx 113°$ [25]. All condensation experiments were performed by cooling the substrate down to $T_w = 1.0\,°\text{C}$ with an ambient temperature of $T_\infty \approx 20°\text{C}$ and a relative humidity of $RH \approx 59\,\%$. Time-lapse photography captured the evolution of the droplet size distribution over 3 h of continuous condensation, as depicted in the schematic of Figure 3.1b. High-speed imaging was used to capture the jumping and sliding dynamics. Four different surface orientations were used: horizontal, 45°, vertical, and upside-down (Figure 3.1c).

3.3 Results

The results of the time-lapse photography are shown in Figure 3.2 for the horizontal, 45°, and vertical orientations. Previous reports of jumping-droplet condensation have shown a near-constant droplet size distribution over time, even for a horizontal orientation.[11] However, nearly all previous visualizations of jumping droplets have only recorded a few minutes of growth for a single surface orientation [11, 59, 76, 77, 78, 79]. One study by McCarthy et al. did report 24 h of continuous jumping-mode condensation on a vertically oriented

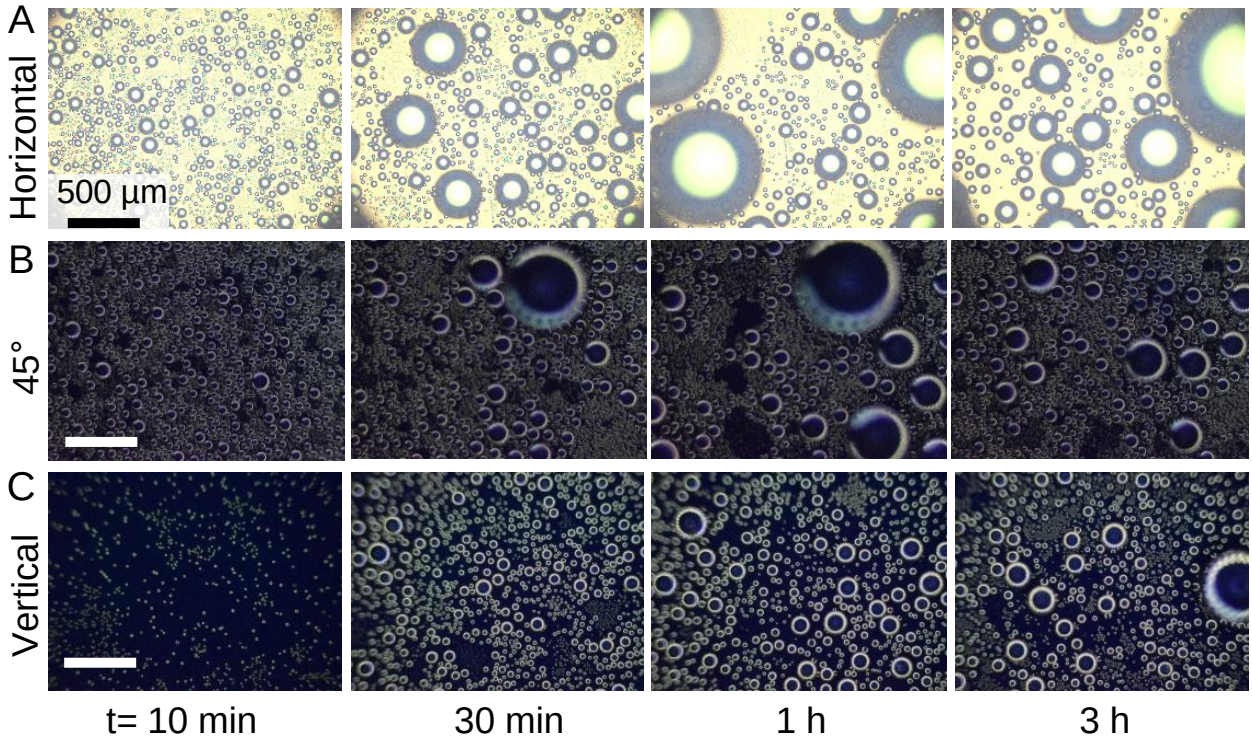

Figure 3.2: Time-lapse photography from the 3 h long condensation experiments. The surface orientations used were: a) horizontal, b) 45 ° inclined and c) vertical.

superhydrophobic surface, but they only quantified the average droplet diameter for the first 12 min [80]. Here, the droplet size distribution was imaged over 3 h of condensation, to reveal that droplets on the horizontal surface continue to grow in size over time (Figure 3.2a). In contrast, condensate on the 45° and vertical surfaces exhibited a near-constant size even after 3 h of continuous growth (Figure 3.2b,c).

The initial capillary-inertial jumping itself is orientation-independent. To explain why the resulting droplet size distribution is still dependent on orientation, high-speed imaging was used to get a fuller picture of the range of droplet dynamics possible during growth. As expected, droplets jumping from the horizontal surface eventually returned due to gravity, which readily explains the increase in droplet size over time (Figure 3.3a). Even for inclined surfaces, droplets can still grow due to gravitational return of jumped droplets (Figure 3.3b), failed jumping upon coalescence due to size mismatch [72, 73, 74], or due to vapor entrainment of jumping droplets [62, 81, 82]. While return by gravity is obviously not applicable to the vertical or upside-down orientations, vapor entrainment was observed even in these cases (Figure 3.3c). From the analysis of Miljkovic et al., for an upside-down surface orientation and a characteristic heat flux of 1 W/cm^2, the critical diameter beneath which vapor entrainment occurs is 38 μm [62]. This matches our experimental observations, where the largest jumping droplet that got entrained by the vapor flow was 33 μm for the upside-down

surface. For the vertical surface, droplets as large as 70 μm returned to the surface as gravity no longer opposes vapor entrainment.

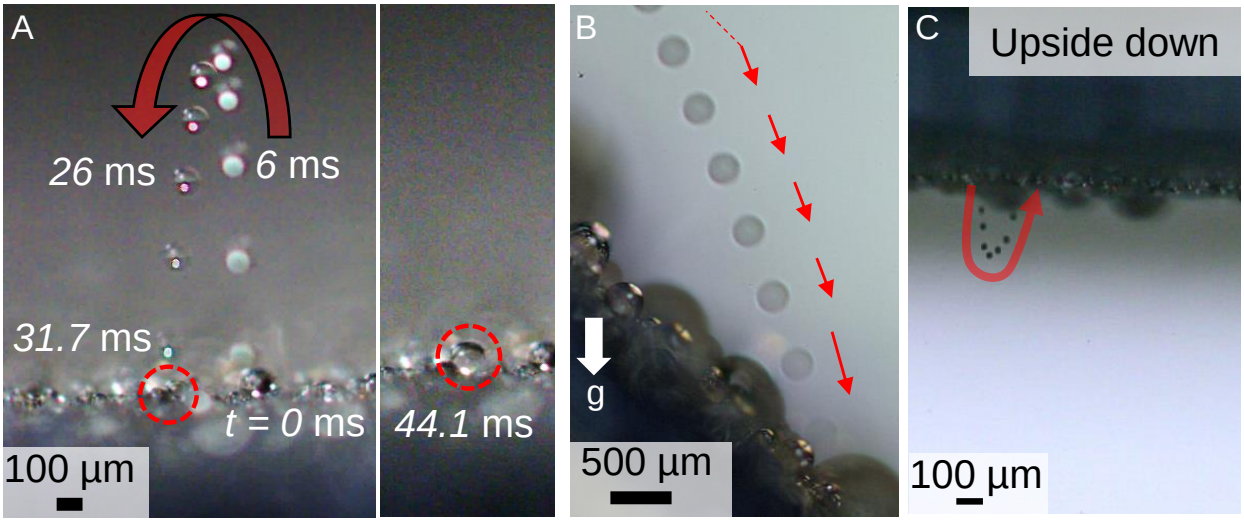

Figure 3.3: Images capturing different droplet removal and return mechanisms on the condensing surfaces. a) Jumped droplets returned to a horizontal surface (first frame chronophotography) and got stuck (second frame). b) Chronophotography of a jumped droplet being returned to a surface at 45° inclination. c) A small droplet returns to an upside-down surface due to vapor entrainment. The red arrows show the droplet trajectory. See Movie S1 for visualizing droplet return on different surface orientations..

3.3.1 Model of Gravity-Assisted Droplet Departure

In short, even vertical or upside-down condensers cannot fully prevent the return of jumping droplets or the failure of certain droplets to jump. However, the use of a gravitational orientation does enable the removal of droplets by sliding or falling, which would otherwise remain stuck on a horizontal surface. Regarding droplets sliding off a condenser, the critical departure size can be approximated from the analysis of Furmidge [83]. Balancing the retention force (i.e. hysteresis) of the Cassie droplet ($F_{hys|C}$) with the gravitational force (F_g):

$$\rho V_c g \sin\alpha \approx \pi a \gamma (\cos\theta_R - \cos\theta_A), \tag{3.1}$$

where α is the inclination angle of the surface, ρ and γ are density and surface tension of water, $V = \frac{\pi}{3}R^3(2 - 3\cos\theta^* + \cos^3\theta^*)$ is the volume of a spherical-cap droplet exhibiting a radius of R and averaged apparent contact angle $\theta^* = \frac{1}{2}(\theta_A + \theta_R)$, and $a = R\sin\theta^*$ is the contact radius. Using $\theta_A \approx 160°$ and $\theta_R \approx 150°$, the calculated critical departure size is

$2R_c \approx 915\,\mu$m on the 45° surface and $2R_c \approx 770\,\mu$m for the vertical surface. This is in good agreement with the experimentally observed departure size of $713\,\mu$m for a droplet sliding down the vertical surface (Figure 3.4a).

For the upside-down surface, droplets must detach and free fall, rather than slide. The critical size for detachment can be estimated by comparing the gravitational energy (E_g) against the work of adhesion required to detach a Cassie droplet ($E_{ad|C}$):

$$\rho V_c R g \approx \pi a^2 \gamma \phi (1 + \cos\theta_a), \tag{3.2}$$

where $\phi \approx 0.295$ is the solid fraction of the pillar tops in contact with the droplet and the averaged apparent contact angle θ^* (embedded in the expressions for V and a) is replaced by θ_A. Solving for V_c and re-expressing in terms of the droplet radius yields a critical size of $2R_c \approx 660\,\mu$m. This gravitational removal could not be observed experimentally, as coalescence-induced detachment (which will be discussed shortly) always occurred before droplets could reach this large size.

Not all of the condensate was able to slide at sizes corresponding to Eq. 3.1. For example, in Figure 3.4a, the droplet shown in red arrows remained adhered to the vertical condenser at size $2R = 1.6$ mm even as the smaller droplet outlined in the green circle was able to slide at $2R = 713\,\mu$m. This can be attributed to many condensate droplets not being in an idealized Cassie state, but rather having a fraction of their base impaled as a Wenzel neck. This spectrum in the extent of partial impalement for jumping-droplet condensation has been directly observed by Miljkovic et al. [60]. It can be understood by considering how a droplet originally nucleates and inflates within the nanostructure. A liquid embryo is initially of size $\sim$1–10 nm [6], such that it can nucleate somewhere inside of a unit cell of roughness [84]. In such cases, the water initially fills a unit cell(s) in a Wenzel state but can subsequently inflate into a Cassie state beyond this impaled neck [85]. This energetic comparison for inflating in the Cassie versus Wenzel states can be simply expressed as [84]:

$$E^* = -\frac{1}{r\cos\theta_a}, \tag{3.3}$$

where θ_a is the intrinsic advancing contact angle on a smooth silanized surface, and r is the surface roughness. A nucleated droplet prefers to inflate into the Cassie state if $E^* < 1$; here, we get $E^* = 0.28$ for our surface parameters of $\theta_a = 113°$ and $r = 9.12$. However, even when $E^* < 1$ and the outer perimeter of the droplet is in the Cassie state, the central portion of the droplet still exhibits a Wenzel state from where it initially nucleated. This explains why some of our droplets approximate a pure Cassie state, where Eqs. 3.1–3.2 are valid, while others exhibit a much higher degree of pinning where new equations now need to be formulated.

For Wenzel droplets on a highly roughened and superhydrophobic surface, the contact angle hysteresis approaches its maximal value: $\theta_A \to 180°$ and $\theta_R \to 0°$ [86]. This Wenzel state therefore modifies the hysteresis term in Eq. 3.1 to $(\cos\theta_R - \cos\theta_A) \approx 2$. Comparing gravity ($F_g$) to the Wenzel hysteresis force ($F_{hys|W}$) yields the modified Furmidge equation:

$$\rho V_c g \sin\alpha \approx 2\pi a\gamma. \tag{3.4}$$

This results in a critical diameter of $2R_c \approx 4.2\,\text{mm}$ for vertical orientation, nearly an order of magnitude larger than that for Cassie droplets. Similarly, for the upside-down orientation the work of adhesion term must be modified for a droplet in the partial Wenzel state. For a Wenzel neck of radius r_p, beyond which the droplet is in the Cassie state, the competition between gravity (E_g) and work of adhesion ($E_{ad|W}$) now becomes:

$$\rho V_c R g \approx 2\pi {r_p}^2 \gamma(1-\phi) + \pi a^2 \gamma(1+\cos\theta_a)\phi, \tag{3.5}$$

where the first term on the right-hand side represents the energy required to rip the droplet from its neck and the second term is the energy for detaching the liquid-solid interface from the pillar tops. The value of r_p for a given surface structure can be estimated by the three-stage energetic growth model developed by Mulroe et al. [25] (see Appendix A.1). Using 119 nm, 531 nm and 69 nm as the average geometrical values of pitch, height and diameters of our nanopillars, respectively, we obtain $r_p \approx 0.30\,\mu\text{m}$. Using this value of r_p, we get $2R_c \approx 1.8\,\text{mm}$ which is three times larger than the critical fall-off size for Cassie droplets.

Besides gravitational removal for Cassie droplets or Wenzel droplets, we discovered a third mechanism for gravitationally-driven droplet removal. In Figure 3.5a, it was observed that the surface energy released upon coalescence was sufficient to detach Wenzel droplets from their impaled necks. In other words, for larger droplets, coalescence can no longer produce jumping but can be sufficient for detaching from Wenzel necks. Besides detachment, another hypothetical possibility is for the impaled necks to dewet (i.e. recede) out of the cavities. However, it is now well-known that the impaled Wenzel state is almost always irreversible [87, 88, 89], as the energy barrier for pinch-off is lower than that for dewetting [90]. A final scenario, of coalescence actually increasing the extent of droplet impalement, was ruled out from energetic [87] and physical criteria [53] (see Appendix A.2).

The schematic shown in Figure 3.5b represents the model used to rationalize this coalescence-induced detachment. When two (or more) droplets coalesce with each other, they release excess surface energy [11]. Assuming a spherical cap geometry for two similar-sized droplets in a partial Wenzel state, from simple geometric relations we can write the excess surface

energy due to coalescence as [91]:

$$\Delta E_s = \pi\gamma[4R^2(\cos\theta_{app} - 1) - 2^{\frac{4}{3}}R^2[(2 + \cos\theta_{app})(\cos\theta_{app} - 1)^2]^{\frac{2}{3}}], \tag{3.6}$$

where R is the radius of the droplets before coalescence and θ_{app} is the apparent contact angle of each droplet. Using Figure 3.5a as an example, $R \approx 867\,\mu$m, while $\theta_{app} = \theta_A = 160°$ from the aforementioned goniometric measurements of deposited droplets. While it is true that the deposited droplets were in a Cassie state while the droplets here exhibited a Wenzel neck, the outermost perimeter of these pinned droplets is in the Cassie state which governs the angle. Plugging these values into Eq. 3.6 yields $\Delta E_s \approx 10^{-6}$ J. This excess energy must overcome the work of adhesion required for detachment from the impaled necks. Before coalescence, each droplet is pinned by a Wenzel neck of cross-sectional area $A_p = \pi {r_p}^2$. The work of adhesion to detach two droplets from their Wenzel necks, while the merged droplet still rests atop the pillars, is given by:

$$E_{ad|N} \approx 4\pi {r_p}^2\gamma(1 - \phi). \tag{3.7}$$

If the ratio of $\Delta E_s / E_{ad|N} \gg 1$, then droplets will detach from their pinned necks upon coalescence. For our surface, we found that $E_{ad|N} \approx 10^{-14}$, which results in $\Delta E_s / E_{ad|N} \approx 10^8 \gg 1$ for a droplet radius of $R = 867\,\mu$m. When the merged droplet exceeds the critical diameter for sliding in the Cassie state (Eq. 3.1), departure occurs immediately upon coalescence-induced detachment from the Wenzel necks. For example, the aforementioned 1.6 mm droplet stuck to the vertical surface (Figure 3.4a) was able to shed immediately after merging with a smaller droplet (Figure 3.4b), as a critical diameter of only $770\,\mu$m is required once in the Cassie state (Eq. 3.1). For the example on the 45° surface (Figure 3.5a), the droplet was $2R \approx 2$ mm after coalescence which similarly exceeds the critical diameter of $915\,\mu$m.

Coalescence can also overcome the work of adhesion required to detach impaled droplets from an upside-down condenser, at which point gravity induces droplet falling (Figure 3.4c). Comparing the same surface energy released upon coalescence to the work of adhesion for droplet detachment, we get the following equation:

$$\begin{aligned}\pi\gamma[4R_c^2(\cos\theta_{app} - 1) - 2^{\frac{4}{3}}R_c^2[(2 + \cos\theta_{app})(\cos\theta_{app} - 1)^2]^{\frac{2}{3}}] \\ \approx 4\pi {r_p}^2\gamma(1 - \phi) + 2\pi a_c^2\phi\gamma(1 + \cos\theta_a)\end{aligned} \tag{3.8}$$

where $a_c = R_c \sin\theta_A$ is the contact radius of each droplet before coalescence. This equation can be solved for the critical value of R_c.

To our knowledge, gravitational shedding enabled by coalescence-induced droplet detachment has not been previously reported. Past studies have instead focused on the ability of coalescence to trigger out-of-plane jumping [11, 21, 68] or in-plane sweeping [79, 92], for micrometric droplets where gravity was not playing a role. Other works have characterized the chain reactions triggered by jumping droplets returning to the surface for subsequent coalescence-induced jumping events [11, 70, 93]. Finally, it has been shown that coalescence can trigger dewetting [94, 95] or neck detachment [26, 91] to switch the merged droplet to the Cassie state, but only for microscopic droplets on a horizontal substrate. Instead of only using coalescence to eject microscopic condensate, our findings indicate that coalescence can work in tandem with gravity to remove mid-sized droplets that could not be removed by surface tension or gravity in isolation.

In Figure 3.6, we have constructed phase maps that graph the critical departure radius for each possible mode of droplet detachment and departure. The critical radii were non-dimensionalized by the capillary length of water: $l_c = \sqrt{\gamma/\rho g} \approx 2.7\,\text{mm}$. The red region in the bottom of each phase map represents nano-scale condensate that has not yet been able to inflate to large apparent contact angles. Prior to inflation, such droplets are not prone to removal from either coalescence or gravitational mechanisms. The green dotted line in each map represents the critical size above which coalescence-induced jumping is now possible, $R/l_c \sim 10^{-4}$, due to the droplets now being inflated [25]. As already discussed, due to various factors including entrainment or size mismatch, some droplets will remain stuck to the surface even in the blue regions above the green dotted lines. The remaining aspects of the phase maps differ depending on whether the surface is inclined or upside-down, which will now be discussed in turn.

For inclined surfaces (Figure 3.6a), droplets stuck on the surface can at least detach from their Wenzel necks upon coalescence in the blue region above the green line. This is because the two necessary conditions are both satisfied: the droplets are inflated to large angles (i.e. above green line) and the surface energy gained upon coalescence can overcome the work of adhesion required to detach from the necks, as $\Delta E_s / E_{ad|N} > 1$ for micro-scale droplets (Eq. 3.6 and Eq. 3.7). The detachment of impaled droplets in the blue region of the phase map could not be observed, as the Wenzel necks within the nanostructure are too small to be optically resolved while the droplets themselves still remain pinned on the surface. The solid blue line represents the critical droplet size where Cassie droplets can slide off the surface by gravity (Eq. 3.1). The blue diamond symbol corresponds to the critical size of an isolated Cassie droplet sliding down the surface, as measured in Figure 3.4a, in excellent agreement with the blue theory line. The green region above this blue line represents droplets still in the impaled state, where as soon as they coalesce to detach into the Cassie state, can therefore immediately slide down the surface. Experimental measurements of this coalescence-induced detachment and sliding are shown as blue circles. Finally, for any unlucky impaled droplets that never coalesced with similar-sized neighboring condensate, gravitational sliding within the impaled state is estimated by the orange dotted line (Eq. 3.4). No experimental observations of impaled droplet sliding were observed, as coalescence always

occurred before growing to a size commensurate with the orange line.

An analogous phase map can be drawn for the upside-down orientation (Figure 3.6b). Now gravity no longer facilitates droplet sliding along the surface, but rather, causes droplets to fall from the surface once their work of adhesion is overcome. This is why the upside-down phase map now plots the droplet size against the solid fraction of the surface (ϕ), as the work of adhesion is a function of the droplets' contact area with the pillar tops. For condensate impaled with Wenzel necks, recall the critical size above which the energy gained from two-droplet coalescence overcomes the work of adhesion is given by Eq. 3.8. This results in $R/l_c \sim 10^{-5}$, an order of magnitude smaller than the size required for the droplets to inflate and coalesce in first place (green line). Therefore, the blue region above the green line satisfies the dual criteria for impaled droplets to be both inflated and result in coalescence-induced detachment and falling from the surface. Blue circles depict the experimentally measured droplet sizes where coalescence-induced detachment and subsequent gravitational falling occurred. Comparing ΔE_s to the work of adhesion for droplets able to initialize in the Cassie state ($E_{ad|C}$), we found that droplets of any size will detach upon coalescence which could not be shown directly in the phase map. This is expected to be the minority case, however, as most condensate originates with Wenzel necks. For hypothetical droplets that do not coalesce, gravity eventually overcomes the work of adhesion at much larger sizes. This is shown for Cassie droplets (Eq. 3.2) or for droplets with Wenzel necks (Eq. 3.5), with the blue and orange lines respectively. While the critical size for gravity-induced detachment was lower for Cassie droplets compared to Wenzel, this distinction was so small that the phase lines virtually overlap. This is because the pillar top adhesion dominates over that of the small Wenzel neck for droplets of this size.

3.3.2 Heat Transfer Analysis

The demonstrated orientation-dependence of gravity-induced droplet departure rationalizes the contrasting droplet size distributions shown in Figure 3.2. These disparate droplet size distributions are quantified in Figure 3.7 using image analysis over the full 3 h of growth. The average droplet size increased continuously to about $D_{\text{avg}} \approx 100\,\mu$m after 3 h of growth on the horizontal surface. In contrast, a smaller plateau value of $D_{\text{avg}} \approx 30\,\mu$m was reached on both the 45° inclined and vertical surfaces (Figure 3.7a).

The maximum droplet size was $D_{\text{max}} \approx 1.4$ mm and climbing for the horizontal surface, nearly an order of magnitude larger than the stable value of $D_{\text{max}} \approx 160\,\mu$m on the vertical surface (Figure 3.7b). The maximum droplet diameter measured here for the vertical orientation is smaller than the sliding diameter shown in Figure 3.4a. This is because jumping droplets do not tend to return to the surface for a vertical orientation, such that droplets as large as that shown in Figure 3.4a are extremely rare and not visible in the field-of-view used for the Figure 3.7 measurements. In Figure 3.7b, the maximum droplet diameter on the 45°

inclined surface is slightly larger than the horizontal orientation for the first hour. This can be explained by the stochastic nature of droplet nucleation (particularly for small field-of-views) and also by the fact that the gravitational removal offered by the inclined surface is not enabled until droplets have time to grow to larger sizes.

The projected surface coverage of dropwise condensation plateaus to a self-similar value, typically about $\epsilon^2 \approx 0.6$ [96, 97]. Our horizontal surface exhibited a self-similar value of $\epsilon^2 \approx 0.7$, significantly more than the 45° inclined ($\epsilon^2 \approx 0.45$) or vertical ($\epsilon^2 \approx 0.3$) surfaces (Figure 3.7c). These findings can all be explained by the inability of the horizontal surface to shed returning jumping-droplets (or droplets that failed to jump due to size mismatch), while the inclined surfaces could shed such droplets gravitationally by the mechanisms summarized in Figure 3.6. Given that Wenzel necks remain impaled within the surface, even after droplet detachment and departure, flooding could be a concern as new droplets (and necks) form over time. Flooding was not observed here, however, as evidenced by the steady-state surface coverage. We attribute this to the lower nucleation energy barrier of the wet unit cells (i.e. necks) causing subsequent droplets to inflate in the same regions.

Using the measured values of $D_{\max}$, the condensation heat transfer coefficient can be estimated using the model established by Le Fevre and Rose [56] with modifications accounting for the superhydrophobic structured surfaces [60, 98]. The heat transferred across a single droplet of radius 'r' is expressed as:

$$q_d(r) = \frac{\pi r^2 (\Delta T - \frac{2T_{\text{sat}}\gamma}{r h_{fg} \rho})}{\frac{1}{2h_i(1-\cos\theta)} + \frac{r\theta}{4k_w \sin\theta} + \frac{1}{k_c \sin^2\theta}\left[\frac{k_p \phi}{\delta_c k_p + h k_c} + \frac{k_w(1-\phi)}{\delta_c k_w + h k_c}\right]^{-1}}, \tag{3.9}$$

where ΔT is the degree of subcooling, T_{sat} is the saturation temperature of the water vapor, h_{fg} is the latent heat of vaporization, h_i is the interfacial condensation heat transfer coefficient, δ_c is the thickness of the conformal hydrophobic coating, h is the height of the nanopillars, and k_w, k_p and k_c are the thermal conductivities of water, silicon, and the hydrophobic coating, respectively. The interfacial heat transfer coefficient is itself given by:

$$h_i = \frac{2\hat{\alpha}}{2 - \hat{\alpha}} \frac{1}{\sqrt{2\pi R_g T_{\text{sat}}}} \frac{{h_{fg}}^2}{\nu_g T_{\text{sat}}} \tag{3.10}$$

where R_g is the specific gas constant, ν_g is the water vapor specific volume at T_{sat}, and $\hat{\alpha}$ is the condensation coefficient ranging from 0 to 1 where $\hat{\alpha} = 1$ signifies the complete condensation of all vapor molecules impinging on the liquid surface. As the heat transfer coefficient does not vary widely with $\hat{\alpha}$, we have used a representative value of $\hat{\alpha} = 0.35$ in our model [99]. This results in a value of $h_i = 0.1\,\text{MW/m}^2\cdot\text{K}$, close to the value reported by

Kim and Kim [98]. The total condensation heat transfer coefficient, h_c can then be found by integrating $q_d(r)$ across the entire droplet size distribution:

$$h_c = \frac{q''}{\Delta T} = \frac{1}{\Delta T}\left[\int_{r_{min}}^{r_{col}} q_d(r)n(r)\mathrm{d}r + \int_{r_{col}}^{r_{\max}} q_d(r)N(r)\mathrm{d}r\right], \tag{3.11}$$

where $n(r)$ and $N(r)$ are the size distributions below and above the typical length scale where coalescence occurs. See Appendix A.3 for the expressions of $n(r)$ and $N(r)$ for a condensing superhydrophobic surface, which has been previously reported [28]. For the heat transfer modeling, we have neglected the effect of sweeping as there was not a significant change in the value of heat transfer coefficient and also qualitatively, the variation of h_c with maximum droplet radius remained same (see Appendix A.3 and Figure A.2).

For the simplicity of the model we have assumed a static contact angle, $\theta = \theta_A = 160^\circ$ for the droplets. Although this induces an error in the total heat flux measurement for droplets below $8\,\mu$m [28], for our purpose of providing a qualitative comparison of heat transfer performance in different surface orientations, this error in the model can be neglected. Using fixed values of $T_{\text{sat}} = 287.15\,\text{K}$, $\Delta T = 5\,\text{K}$, hydrophobic coating thickness $\delta_c = 1\,\text{nm}$ and thermal conductivity $k_c = 0.2\,\text{W/m-K}$, pillar height $h = 531\,\text{nm}$ and conductivity $k_p = 150\,\text{W/m-K}$, we can see how h_c varies with changes in the maximum droplet diameter, $D_{\max} = 2r_{\max}$. Figure 3.7d shows that with increased maximum droplet diameter on the surface, condensation heat transfer coefficient decreases exponentially. Le Fevre and Rose observed a similar trend for their model of dropwise condensation on a smooth hydrophobic surface [56].

In the inset of Figure 3.7d, theoretical values of h_c are shown corresponding to experimentally measured values of $D_{\max}$ for the different surface orientations. For the horizontal surface, the maximal droplet size is always increasing with time, so we used the final measured value of $D_{\max} \approx 1.3\,\text{mm}$ at the 3 h mark. For the 45° and vertical surface inclinations, the value of $D_{\max}$ plateaus due to gravitational shedding. For $\alpha = 45^\circ$, the plateau value of $D_{\max}$ oscillated in time, which we attribute to the small field-of-view combined with chain reactions of one jumping/sliding droplet sweeping away many others. Thus, we averaged these oscillatory plateau values together to obtain $D_{\max} \approx 498\,\mu$m. For the vertical surface, a constant plateau value of $D_{\max} \approx 167\,\mu$m was observed after the initial transient. A 3 h experiment was not conducted for the upside-down orientation, as this would have resulted in many droplets obscuring the lens. However, from the "bottom-up" imaging of an upside-down condenser, we observed the largest possible droplet size prior to coalescence-induced detachment and falling. Discounting local areas where scratches or defects were visibly present, the largest departing droplets were approximately $D_{\max} \approx 334\,\text{um}$ after at least 2 h of continuous condensation.

Due to these orientation-dependent disparities in $D_{\max}$, the condensation heat transfer was

enhanced by approximately 40% for $\alpha = 45°$ and by 100% for $\alpha = 90°$ compared to the horizontal condenser. The upside-down surface exhibited a higher h_c than both the horizontal and 45° orientation, but lower than the vertical orientation. This can be rationalized by the fact that both the upside-down and vertical orientations have a lower frequency of returning droplets compared to the 45° and horizontal surfaces. In turn, the vertical surface being slightly better than the upside-down can be explained by the beneficial sweeping effect that is exclusive to droplets sliding down an incline.

The heat transfer model used to find the theoretical heat transfer coefficient presumes that the non-condensable gases (NCGs) have been removed from the system. When NCGs are present, as in the case of our experiments, they act as a diffusive barrier to the water vapor [100, 101, 102]. This slows the growth rate of condensate and decreases the heat transfer coefficient, but is not expected to affect the orientation-dependent droplet dynamics captured here that govern the maximum droplet sizes. The droplet size distribution is also a function of the coalescence length scale, which is related to the nucleation density and depends on both the supersaturation and the concentration of NCGs. Here, we chose a value of $r_{\text{col}} = 1\,\mu$m that is representative of our surface and experimental conditions. In the absence of NCGs, the actual subcooling (within the water vapor layer) can increase for the same supersaturation, which may result in surface flooding [103]. It has recently been shown that this issue can be mitigated by using tall and dense nanowires that promote nucleation atop the surface [64].

These trends are qualitatively similar to those reported by Koch et al. for dropwise condensation on a smooth surface, where the vertical orientation performed the best and the flat surface performed the worst [58]. However, extending this concept of orientation-dependence to jumping-droplet condensation for the first time results in some interesting new insights. For example, recent experimental measurements of jumping-droplet heat transfer coefficients have found 30% [22] and 60% [65] enhancements compared to dropwise condensation on a smooth surface. The superior performance of the latter case was exclusively attributed to the addition of hydrophilic bumps to increase the nucleation density, but we suggest it could additionally be due to its vertical orientation compared to the use of a horizontal tube in the former case. Indeed, the report using a horizontal tube did very briefly mention an observation of larger droplets at the bottom of the tube compared to the sides [22], which is better understood in light of our present work. Follow-up studies should experimentally measure h_c for a superhydrophobic surface with different surface orientations, and also pay more attention to a possible time-dependence for h_c especially for the horizontal case. Finally, the measured contact angle hysteresis for Cassie droplets ($\approx 10°$) is relatively high on our present surface compared to other superhydrophobic surfaces; it is probable that the heat transfer of the vertical orientation could be even further enhanced using more advanced surface structures.

3.4 Conclusion

Here, have shown that the dynamics of jumping-droplet condensation are heavily affected by gravity and surface orientation. While larger droplets become stuck on a horizontal superhydrophobic condenser, they are capable of sliding down an inclined surface or detaching from an upside-down surface. We also identified that coalescence can serve to detach larger droplets from their pinned Wenzel necks, which substantially reduces the critical size required for gravitational sliding. These orientation-dependent shedding dynamics directly affect the resulting droplet size distribution of growing condensation, which in turn affects the heat transfer coefficient. Compared to the baseline cases of flat or upside-down condensers, a jumping-droplet surface inclined by 45° or 90° should exhibit an increase in heat transfer of 40% and 100%, respectively. These findings should have profound implications regarding our understanding of jumping-droplet condensation heat transfer, for example a vertical wall should perform better than the horizontal tubes currently used to measure efficiency. Given that jumping-droplet condensation already exhibits a higher heat transfer coefficient than any other form of condensation, the ability to increase performance even further with an optimal surface orientation should motivate future implementation in power plants and HVAC systems.

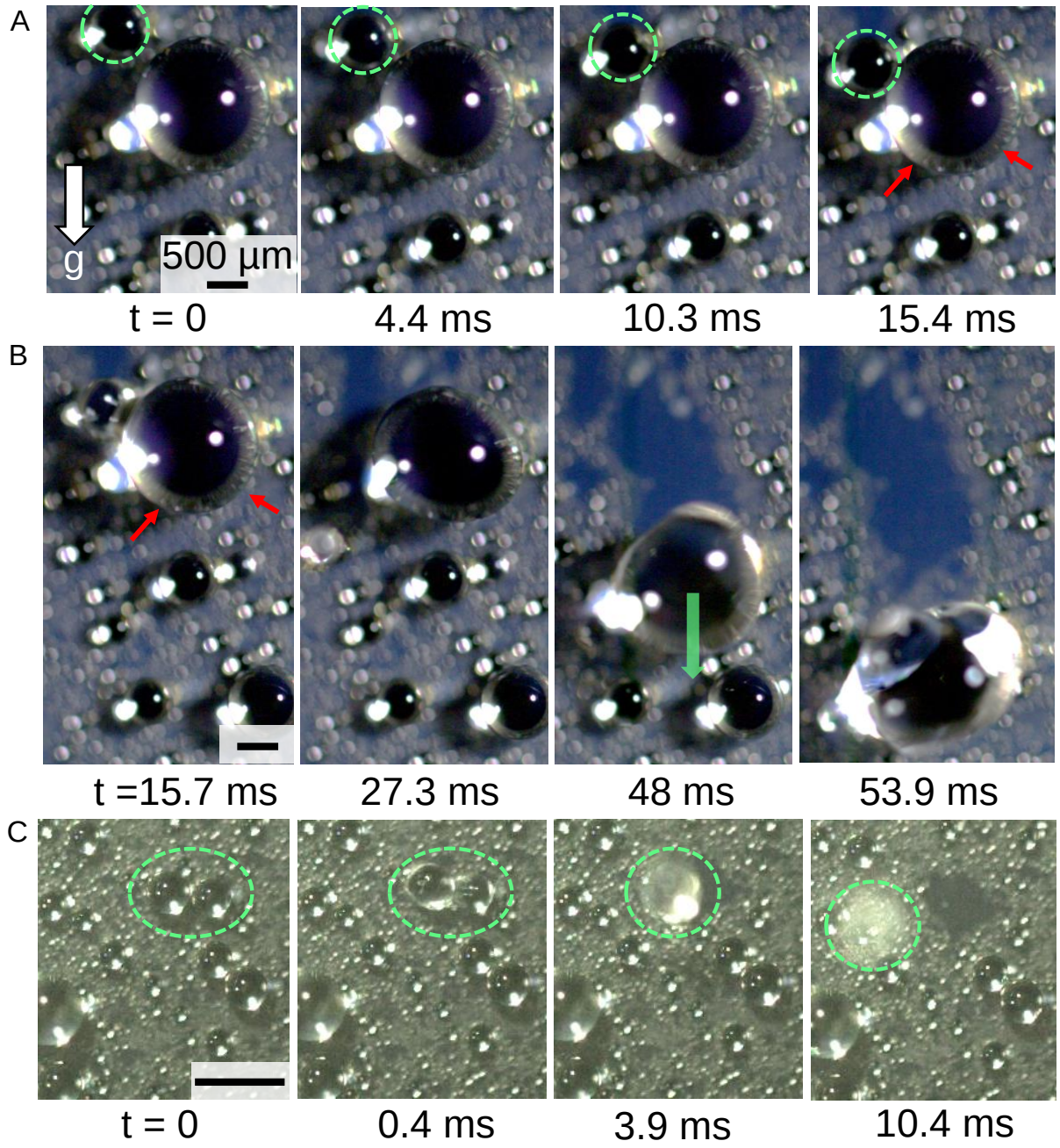

Figure 3.4: Gravitational sliding of droplets on a vertically oriented surface. a) The droplet marked in the green circle started sliding as it was near the critical departure size for Cassie droplets on the vertically oriented condenser. Even though the droplet marked in red arrows was much bigger than the sliding droplet, it was stuck due to impalement on the surface structures. b) The bigger droplet (red arrows) started sliding after coalescing with the smaller droplet (green circle). c) For an upside-down surface orientation, droplets virtually always fall or jump from the surface upon coalescence (green circle).

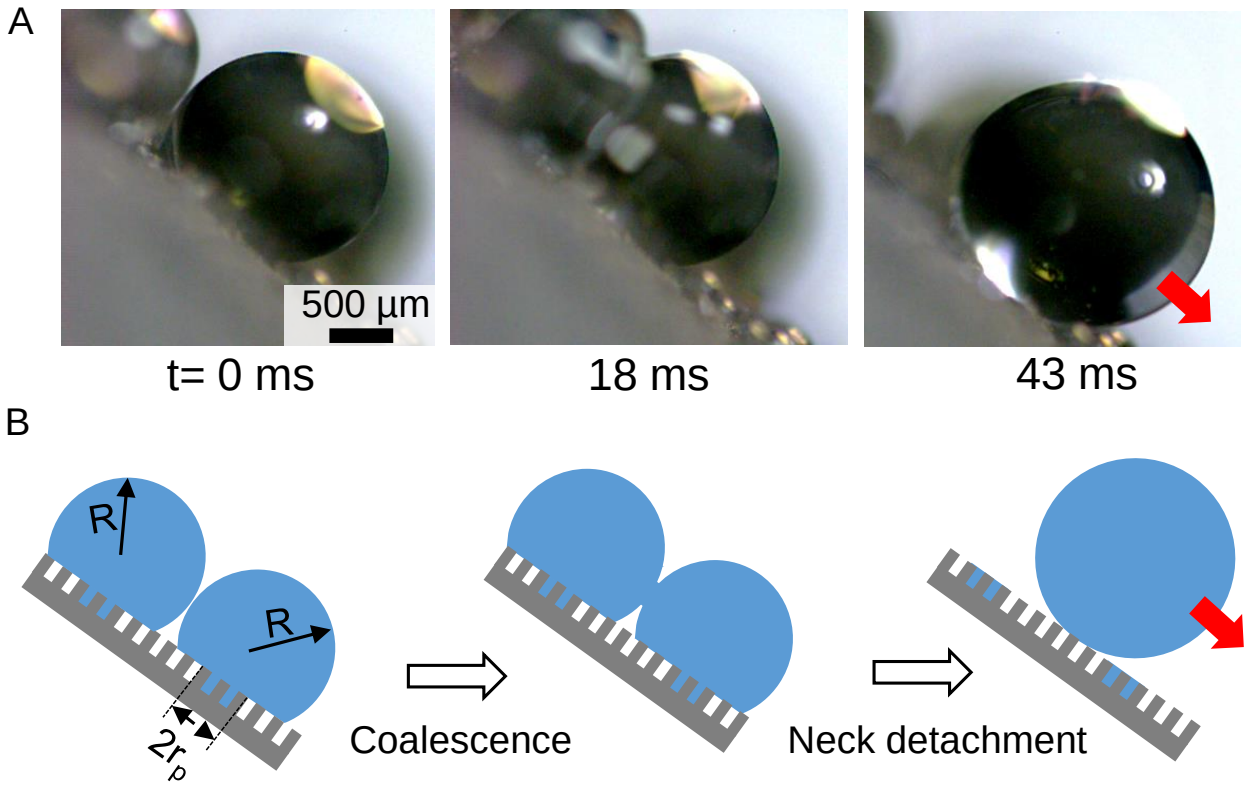

Figure 3.5: Coalescence-induced neck detachment and subsequent gravitational sliding. a) Side-view imaging of gravitational shedding facilitated by coalescence on a 45° inclined surface. Initially, the two droplets are pinned on the surface despite being millimetric in size. As the two droplets coalesce together, the released surface energy is used to detach the merged droplet from the impaled Wenzel necks, enabling sliding in a Cassie state. See also Movie S2. b) Schematic of the coalescence-induced gravitational droplet departure mechanism.

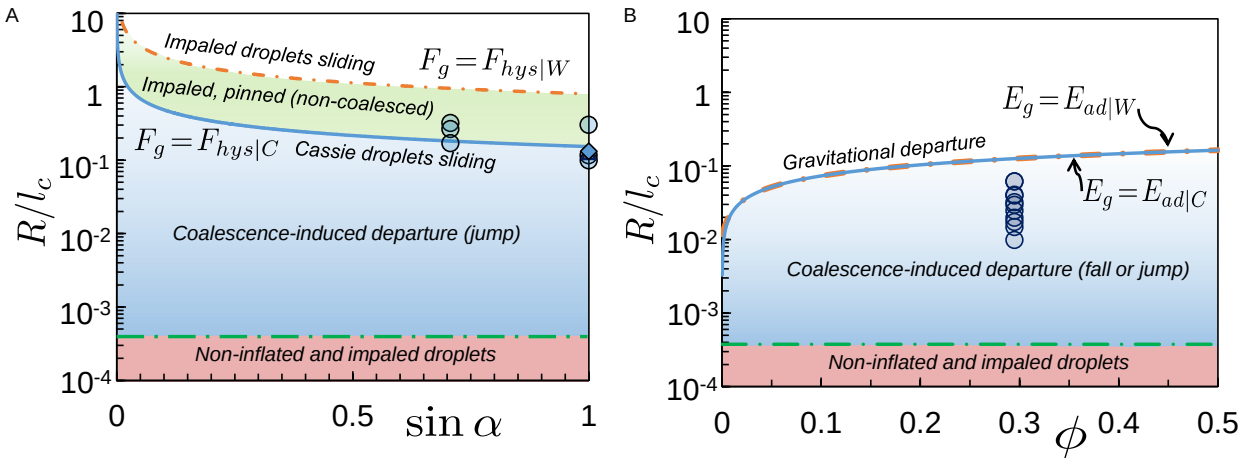

Figure 3.6: Semi-log phase maps showing the different regimes of gravity-assisted removal of condensate from superhydrophobic surfaces. Both Cassie droplets and impaled droplets with Wenzel necks are considered. a) For inclined orientations, the non-dimensionalized critical droplet radius (R/l_c) depends on the inclination angle (α). The green dashed line represents the minimum size for the coalescence-induced jumping of an inflated droplets. The blue circles are all experimental observations of droplets shedding by gravity after coalescence-induced neck detachment. The blue diamond is the only experimental case of an isolated Cassie droplet sliding by gravity upon reaching the critical size. b) For an upside-down surface, R/l_c now depends primarily upon the solid fraction governing the work of adhesion. Experimental data points for the coalescence-induced droplet detachment and falling are shown by the blue circles.

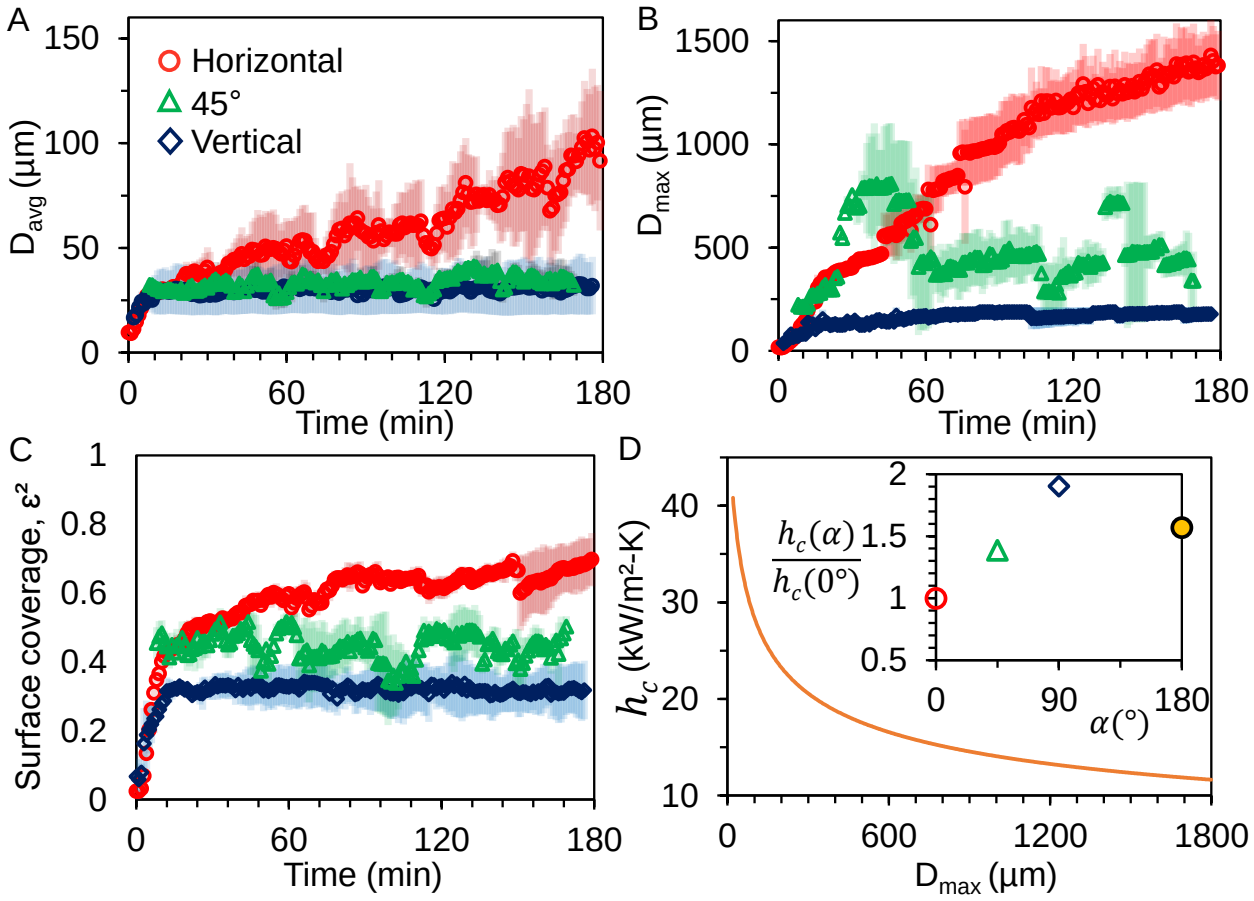

Figure 3.7: Summary of orientation-dependent droplet size distributions and their effects on heat transfer. Variation of the a) average droplet diameter; b) maximum droplet diameter and c) fraction of the condensing surface covered by the droplets with time for different surface orientations. Error bars represent one standard deviation over three trials for the horizontal and 45° orientations and over two trials for the vertical orientation. d) Exponential decay of the theoretical steady-state condensation heat transfer coefficient (h_c) with increasing maximum droplet diameter ($D_{\max}$) on the surface with $\hat{\alpha} = 0.35$ and $\Delta T = 5\,\mathrm{K}$. Inset: heat transfer coefficients at different surface inclinations with respect to that for a horizontal orientation.

Chapter 4

How Jumping-Droplet Condensation Spreads Fungal Disease with the Help of Wind

"The answer, my friend, is blowin' in the wind..."

–Bob Dylan

The content of this chapter is just accepted as an article in PNAS [104], and reproduced here with minor modifications. This chapter experimentally investigates the synergistic effect of wind and jumping-droplet condensation on the dispersal of rust spores from superhydrophobic wheat leaves.

4.1 Introduction

Spores of plant pathogenic fungi are spread in three stages: liberation from the host by some active or passive method(s), drift by biotic or abiotic factors, and deposition onto a new host [105]. Examples of active liberation mechanisms include osmotic pressure-driven ejection of ascospores of *Fusarium graminearum* (causal agent of Fusarium head blight of wheat) and ballistospore ejection from the tip of a sterigma due to the chemical secretion of a Buller's drop of the jelly fungus *Auricularia auricula* [106, 107]. In the absence of wind, the resulting dispersal distance is a function of both the weight of the spore(s) and the initial discharge velocity, with the range of discharge varying from 40 μm for basidiospores [108] to 6 m for the artillery fungus [109]. Passive liberation and dispersal mechanisms, such as wind and rainsplash, can spread fungal diseases in plants [110]. For wind to successfully liberate dry spores, an unusually strong and/or sudden gust of wind is required [105, 110, 111, 112, 113]. In contrast, rainsplash can liberate spores from a plant either through transferring momentum to the leaf to launch spores off [114, 115] or by adhering spores to splashed satellite droplets [116, 117]. Spores ejected by active methods or rainsplash can only disperse over a very short distance in the absence of wind [118], but when carried in moderate winds can travel for many kilometers [119, 120].

After liberation, dispersion of spores increases the number of infection sites and consequently, the probability of disease among susceptible hosts within a field or beyond[105, 121]. Dispersal gradients, which show the variation in spore concentration along the distance from the source, are often estimated to provide insights into the specific spore dispersal mechanisms. Wind is the most important abiotic factor for any large scale fungal disease dissemination[120] which can act singularly or concomittantly with the other active or passive dispersal mechanisms[118]. For active discharge, the dispersal distance is a function of both the weight of the spore(s) and the initial discharge velocity as the range of discharge varies from 40 μm for the basidiospores[108] to 6 m for the artillery fungus[109]. Rainsplash can also disperse spores via either dry dispersal[115, 122] or spore-laden small satelite droplets released by the impact of the raindrops on the plant surface[116]. Almost all of these active or passive dispersal mechanisms are spatially limited to few plant distances in a canopy and needs the assistance of wind for any significant travel distance.

One recent study reported an entirely new mode of pathogen liberation, where coalescing dew droplets on superhydrophobic wheat leaves jump out-of-plane with considerable velocity (0.1–1.0 m/s) and carry adhered spores of a fungal plant pathogen [24]. Mechanistically, the out-of-plane motion is a result of symmetry breaking as the expanding liquid bridge during coalescence impinges upon the bottom substrate [11, 21, 68] (Fig. 6.1A). While this initial report characterized the jumping-droplet liberation of spores in the absence of wind [24], it did not consider the subsequent dispersal or deposition which ultimately governs the rate of disease spread. Here, we characterize the dispersal of spores of leaf rust (*Puccinia triticina*) after they are liberated from a diseased wheat leaf via jumping-droplet condensation. Two different scenarios are explored: short-range and long-range drift and deposition in the

absence and presence of wind flow, respectively (Fig. 6.1B,C). We found that even a low wind speed is capable of dispersing as many as 100 jumping droplets and 25 spores to a single leaf downwind of a diseased leaf saturated in dew. Our ability to quantify both the liberation and dispersal of fungal spores from a diseased leaf during a dew cycle improves our understanding of disease spread within and among plants [105, 121, 123, 124].

4.2 Materials and Methods

Preparation of wheat leaves

A mixed seed of two winter wheat lines, Massey and VA-135, both known to be susceptible to stem rust, were provided by the Griffey lab at Virginia Tech. The growth and inoculation process of the plants are the same as that described in previous reports[24, 115]. The mature leaves were cut from the stem and used within 6 h for the experiments.

Experimental set-up

For all the condensation-induced and dry spore dispersal experiments, a section of a diseased wheat leaf was bonded with thermal grease (Thermalcote, 251G-ND) to a cold plate attached to a chilled recirculator (Fischer Scientific, 13874647). Each leaf section was approximately 3 cm long and was taken from the middle portion of a wheat leaf, where the width was fairly uniform and approximately 1 cm (see Figure B.1). The cold plate was custom machined, such that three of the leaf section's four edges perfectly aligned with the edges of the plate. Due to the varying laboratory ambient temperature and humidity, the cold plate temperatures were varied across the experiments while maintaining a supersaturation of $S = 1.49 \pm 0.26$. Jumped droplets from the leaf sections were captured on 76 mm×26 mm water-sensitive papers (Syngenta, 347456). The condensation experiments were started only after the cold plate temperature reached the set value and significant condensate droplets appeared on the leaf surface. All experimental trials were run for 1 h. A total of three trials were run for each case (No wind, $V_{\text{wind}} = 0.5$ m/s, $V_{\text{wind}} = 1.5$ m/s, and dry dispersal). Wind experiments were done using either of the two variable speed fans (AC Infinity, Multifan S1, or TerraBloom, TB-MFIF-6). In all the experiments involving wind, to achieve the desired wind speed above the leaf, the speed of the fan and the distance between the fan and the leaf were changed. Wind speed measurements were done 1 cm above the leaf and the water-sensitive papers with an anemometer (Omega, Model No.: HHF81). For the no-wind experiments,

the anemometer was used to confirm a zero wind speed in the laboratory. While there was some minor air circulation in the laboratory that sometimes boosted the lateral movement of jumping droplets, it was always beneath the anemometer's minimum measurable wind speed of 0.4 m/s. For the dry dispersal of spores with only wind and no condensation on the leaf, 3×5 in. adhesive papers (Sensor®, Yellow Pest Monitoring Cards) were used to capture the dry spores from the leaf.

Image Analysis

The stain-patterned water sensitive papers were collected at the end of a condensation experiment trial (see Figure B.3). The papers were then analyzed under an optical microscope (Nikon, Model: Eclipse LV150) with a 10X objective lens (Mitutoyo, M Plan APO). Due to the magnified field-of-view being much smaller than the paper dimensions, we used a live image-stitching software (Manual Whole Slide Imaging, Microvisioneer) to obtain a composite image of all spores and droplet stains. The stitched images were then analyzed in Qupath, an open source image analysis software. For the dry dispersal experiments, the same technique was used to count the spores.

Fungicide spraying on healthy leaves

A fungicide solution was prepared by mixing 80 ppm fungicide (Proline 480 SC Fungicide, Bayer CropScience) and 125 ppm surfactant (TopSurf, Winfield Solutions) in water. See a previous report[117] for specific details on the fungicide and surfactant constituents. An atomizer (Portable SprayerSystem, Preval 267) was used to spray this solution on the healthy wheat leaf sections. For a uniform coating, the sprayer was held about 5 cm above a leaf section and sprayed while guiding it back and forth once, along the length of the leaf. Contact angle measurements and video imaging of coalescence on these sprayed leaves were done once the leaves were dried for at least 2 h under a fume hood.

Imaging

A high-speed color camera (Vision Research, Phantom v711) was used to capture the jumping droplet liberation and drift from the healthy wheat leaves as well as the coalescence of condensing droplets on the fungicide-sprayed wheat leaves. All the videos were captured at 7,500 frames per second at 1,024×768 resolution.

Contact Angle Measurements

Advancing and receding contact angles of water droplets on healthy wheat leaves (both non-sprayed and fungicide-sprayed) were measured with a goniometer (ramé-hart, Model 590). A 10 μL water droplet was deposited on the surface and the shrink/swell method was used to find the advancing and receding contact angles.

4.3 Results

4.3.1 Range of spore dispersal via jumping-droplet condensation alone

To explore the short-range dispersal of rust spores without any wind flow, we bond a piece of a wheat leaf to a horizontal cold plate with thermal paste (Fig. 4.2A) and decreased the plate temperature below the dew point temperature. Due to the nanoscale surface asperities on the wheat leaves which render them superhydrophobic, jumping-droplet condensation was observed on the diseased wheat leaves where coalescing droplets jumped off the surface with or without spore(s) [24]. Once a sufficient (i.e. steady-state surface coverage) amount of condensates formed on the leaf (which took about 15–30 min depending on the laboratory air temperature and humidity), a water-sensitive paper was placed on a lower platform directly underneath the leaf on the upper cold plate. After each trial, the water-sensitive paper was analyzed under a top-down optical microscope. Impacted water droplets created quasi-circular dark blue stains on the paper, while adhered spores were directly visible as brown quasi-spherical objects (see Figure B.3). Three different measurements were made from the water-sensitive paper: the number of spores within each droplet stain, the final lateral distance (i.e. stain location) of a jumping droplet from the edge of the overlying leaf (l_f), and the maximum diameter of the stains (D_{max}).

With this information, a dispersal gradient was generated which showed the spatial variation in the spore number density with increasing distance from the source [125]. A modification to the classical dispersal gradient was necessary for our jumping-droplet spore dispersal, as the number of spores within each jumped droplet varied significantly. Therefore we made a three-dimensional frequency plot (Fig. 4.2B), which quantified both the number of droplets and the number of spores per droplet at any given distance from the source leaf. It is evident from the plot that the majority of droplets ($\approx 57\%$) jumping from the diseased leaf contained only one spore. About 39% of the droplets contained 2–10 spores and in rare cases ($\approx 4\%$) droplets contained more than 10 spores. In one case, a droplet contained 55 spores. In terms of the lateral jumping distance from the edge of the leaf, the spore-laden droplet counts were highest within $l_f = 7.5$ mm ($\approx 95\%$). The location of the remaining spore-laden droplets ranged from $l_f = 7.5$–17.5 mm. This shows that even without any appreciable wind, spores

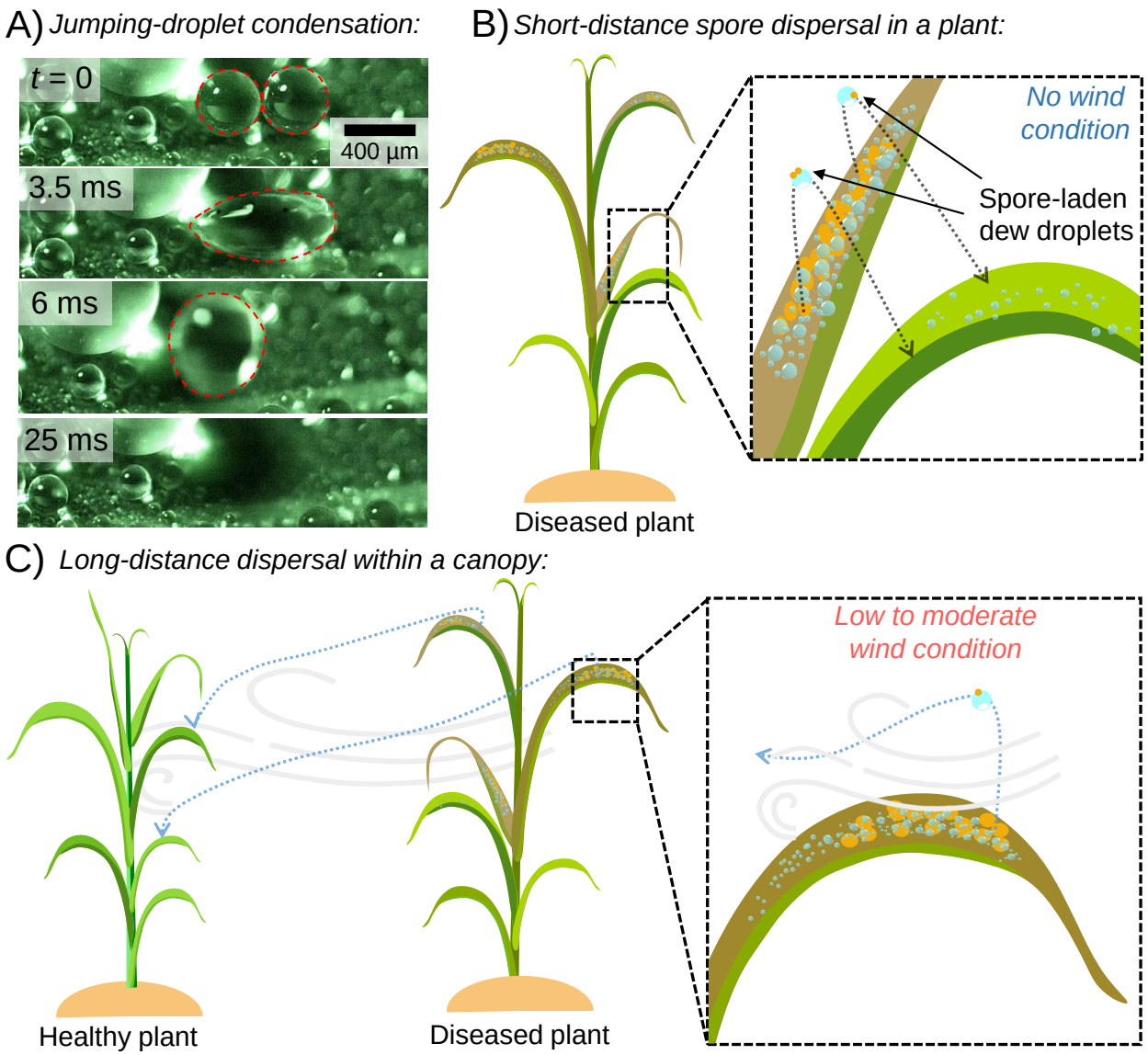

Figure 4.1: Spore dispersal via jumping-droplet condensation. (A) Jumping droplet condensation on a healthy wheat leaf. Two condensed droplets coalesce (2^{nd} frame) and jumps off from the superhydrophobic wheat leaf (3^{rd} frame). (B) Without any wind, the jumped droplets with spores can land on an adjacent healthy leaf spreading the disease within the plant. (C) in low (0.5 m/s) to moderate (1.5 m/s) wind speed the spore-laden jumped droplets can travel close to a meter which is enough to land on a different healthy plant within the field.

can disperse to other leaves of the same plant or leaves of a neighboring plant for a dense canopy [126] powered entirely by jumping-droplet condensation.

To rationalize the experimental measurements of l_f, the theoretical range of a jumped droplet

was calculated. Specifically, we solved the equation of motion for a spherical projectile (the rust spores are spheres) of radius R, launched with an initial velocity u at angle θ_j with respect to the horizontal leaf surface. The jumping velocity is capillary-inertial: $u \approx 0.22(\gamma/\rho R)^{1/2}$, where γ and ρ are the surface tension and the density of water, respectively, and the 0.22 prefactor accounts for the surface energy that is lost to oscillatory (rather than translational) kinetic energy [11, 21, 68]. It was not possible to correlate a stain on the water-sensitive paper with the angle (θ_j) of the corresponding coalesced droplet jumping from the leaf. However, previous studies of jumping-droplet condensation have reported that a wide range of jumping angles are possible: $\theta_j = 10° - 90°$, with the value depending on the number, size, and geometric arrangement of the droplets coalescing together [24, 127].

The pre-impact radius (R) of a droplet can be estimated from the stain diameter (D_{max}) using the spread factor, which is the ratio of stain diameter over the impacting droplet diameter. Spread factor values corresponding to the strain diameters on the water-sensitive papers were extracted from the plots provided with the product datasheet (see Figure B.4). Here, we have assumed all the jumped droplets have impacted the paper with terminal or sedimentation velocity, $V = 2\rho g R^2/9\mu_a$, where ρ and μ_a are the water density and air dynamic viscosity, respectively [128]. For D_{max}, we only considered non-overlapping stains with at least one spore. Using the spread factor relation, the droplet radius range was found to be $R = 11$–$147\,\mu$m.

Using the equation of motion for the specific case of $R = 80\,\mu$m (see section B.1), Fig. 4.2C graphs the lateral displacement (l) of a jumping droplet as a function of time. The three different displacement curves correspond to three different representative jumping angles: $\theta_j = 30°, 60°, 89°$. Each curve stops at a critical time of flight (t_c) where the droplet is predicted to impact the water-sensitive paper, such that $l(t_c) = l_f$. The minimum theoretical value of l_f was 0.17 mm for $\theta_j = 89°$ and the maximum value was 7.46 mm for $\theta_j = 30°$. Additionally, the experimentally measured values of l_f were plotted (green triangles), also for the case study of $R = 84 \pm 5\,\mu$m as obtained from the spread factor and stain diameter relation. For the time axis, all the experimental plot points were placed at the average time of flight value for the three launch angles. The experimental values for l_f all fall within the boundaries set by the theoretical equation of motion. Similar plots for other droplet sizes ($R = 60\,\mu$m, $100\,\mu$m) are included in the Figure B.6. For these other cases, some droplets exhibited an l_f that exceeded the theoretical boundaries, which high-speed imaging confirmed was due to the droplets getting boosted during their descent by the laboratory's air circulation.

4.3.2 Range of spore dispersal via jumping-droplet condensation in presence of wind

We showed that jumping-droplet condensation alone can liberate spores from a diseased leaf, enabling the possibility of multiple disease foci within a plant or neighboring plants

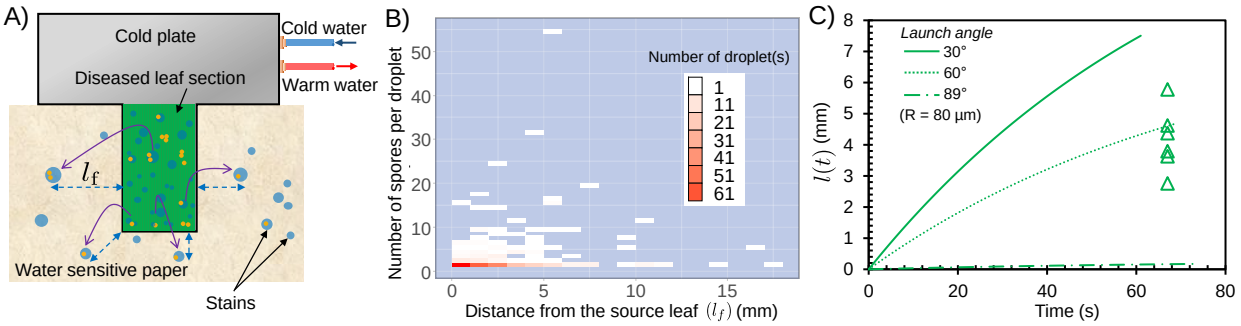

Figure 4.2: Spore dispersal in no wind condition. (A) Experimental laboratory set-up to find the range of dispersal of jumping-droplet condensates with spores in the no wind condition. The water sensitive paper was analyzed under a microscope and the distance l_f from the edge of the leaf was measured for each droplet stain containing a spore(s). (B) Frequency plot showing the number of spore-laden droplets versus the lateral impact distance from the source leaf. The y-axis shows the number of spores in each droplet. (C) Theoretical range for an 80 μm droplet with three different jumping angles: $\theta_j = 30°$ (solid curve), 60° (dotted) and 89° (dot-dashed). Experimentally obtained l_f values (green triangles) were superimposed for droplets whose splash diameter corresponded to a pre-impact radius of $R = 84 \pm 5\,\mu$m, as determined from the spread factors.

(provided optimal environmental conditions and sucseptible hosts). But it is evidently not effective in dispersing the spores beyond few millimeters. As with other passive methods of spore liberation, we should now consider how wind can enhance the range of the subsequent dispersal. In our case, the wind becomes especially relevant once a spore-laden jumping droplet clears the thin laminar boundary layer above the leaf. Thus it is important to consider the synergistic effect of condensation and wind in spore dissemination, similar to how wind affects spore dispersal by rainsplash [129]. Simulating the effect of wind in a laboratory setting is challenging for several reasons. First, the wind increases the spatio-temporal scale of the spore transport [118]. Second, higher wind speeds can be detrimental for the growth of condensate droplets on the leaf, diminishing the jumping-droplet effect. Third, a wind speed higher than a critical value can shear off the droplets from the leaf surface before they can jump *via* coalescence. In this report, we have used two separate wind speeds for the experiments, 0.5 m/s and 1.5 m/s, comparable to the maximum favourable wind speed for dew formation on radiantly cooled surfaces [130], but much lower than the critical wind speed of about 10 m/s for shearing off the spore-laden micrometric droplets off the leaf surface [24].

A previous report by Nath et al. showed that spore-laden condensate from a diseased wheat leaf can jump a vertical distance that tends to range from 1–5 mm [24]. We need to determine whether this jumping distance is enough to clear the quiescent boundary layer above the leaf's surface. The laminar boundary layer thickness δ above a horizontal leaf surface for a free stream wind velocity U can be estimated as $\delta \sim \left(\frac{\nu x}{U}\right)^{1/2}$ [24], where $x \approx 3$ cm is the leaf

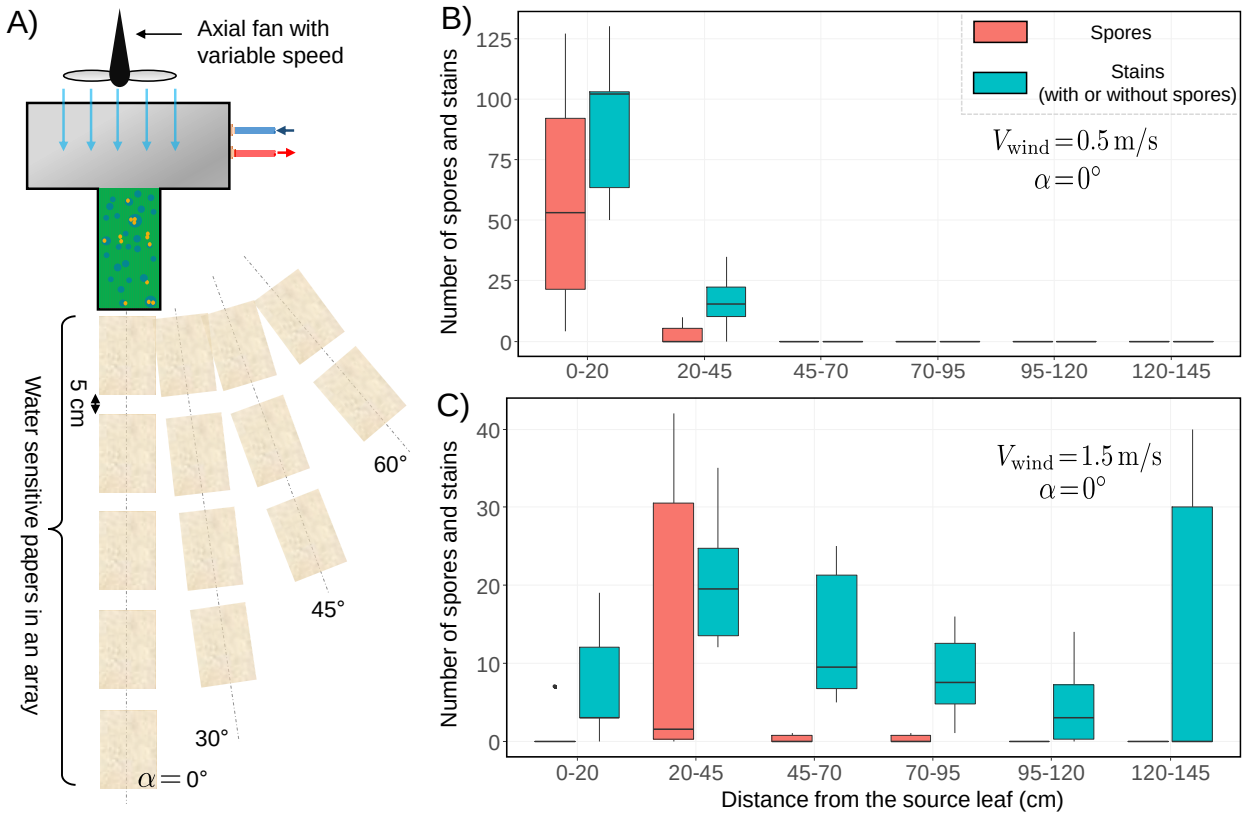

Figure 4.3: Spore dispersal in low to moderate wind condition. (A) A variable-speed axial fan was introduced in the set-up to achieve low to moderate wind condition over the leaf surface. The water sensitive papers were placed in an array with a gap of 5 cm between each paper. To cover a large area around the source, similar paper arrays were placed in 4 different angles. (B,C) Number of stains with or without spores and the number of spores per paper are plotted against the distance from the diseased leaf for two different wind speed- 0.5 m/s (B) and 1.5 m/s (C). All distances are measured horizontally (directly downwind) from the leaf on the extended cold stage platform. Each box corresponding to a distance in the plots represents individual measurements from six separate papers across the three trials.

length along the wind flow direction and $\nu = 1.5 \times 10^{-5}\,\mathrm{m^2 s^{-1}}$ is the air kinematic viscosity. With this, $\delta \approx 0.95$ mm for $U = 0.5$ m/s and $\delta \approx 0.55$ mm for $U = 1.5$ m/s, both less than the characteristic jumping height. Thus, once droplets coalesce and jump off the leaf surface, they can readily cross the slow moving boundary layer to get carried away by the overlying free stream. We will try to validate this hypothesis in the following experiments involving wind-induced dispersal.

The experimental setup involved a variable speed axial fan placed about 10 cm behind the leaf (Fig. 4.3A). Water sensitive papers were arranged in linear arrays with an edge-to-edge distance of 5 cm between each paper. One array of papers was placed directly along the axis

of the wind flow ($\alpha = 0°$), up to a maximum distance of 1.5 m in front of the leaf. Three additional linear arrays of papers were placed at $\alpha = 30°, 45°$ and $60°$ with respect to the wind flow. Once enough condensate droplets were grown on the leaf, the experiment commenced by turning the fan on. The desired wind speed above the leaf was achieved by adjusting the fan speed and/or by changing the distance between the leaf and the fan. The wind speed was measured with an anemometer placed about 1 cm above the leaf, an order of magnitude higher than the boundary layer thickness. The water sensitive papers with the blue stains were collected after 1 hr of the fan being on and analyzed under the microscope. As most of the stains (with and without spores) were found on the papers along the $\alpha = 0°$ line, only those results are plotted here. See Figures B.7 and B.8 for the results from the angled arrays.

Fig. 4.3B and C shows the results of the analysis from the synergistic wind and condensation experiments. Regardless of the wind velocities, spore-laden droplets were found mostly within 45 cm from the diseased leaf. For the higher wind speed of 1.5 m/s, a considerable number of droplets ($\approx$ 80 across three trials) with or without spores traveled as far as 1.5 m, more than three times the maximum distance traveled by droplets in 0.5 m/s wind. Conversely, with higher wind speed, the total number of dispersed droplets (with or without spores) captured by the water-sensitive papers decreased significantly ($\approx$ 640 for 0.5 m/s compared to $\approx$ 400 for 1.5 m/s wind speed, across three trials). One possibility is that the higher wind speed reduces the number of jumping droplets, by disrupting the diffusive flow field that was growing the droplets to promote coalescence. However, it is also possible the higher wind speed actually increases the number of dispersed jumping droplets, due to the decreased thickness of the laminar boundary layer over the leaf. If the latter effect outcompetes the former, the reduced number of captured droplets/spores at higher wind speeds can be rationalized by the fact that many of the droplets simply travel beyond the range of the water-sensitive papers. Wind speed measurements above the individual papers along the $\alpha = 0°$ line (see Figure B.9) for $V_{\text{wind}} = 1.5$ m/s revealed a wind speed of about 0.9 m/s over the farthest paper ($\approx$ 140 cm from the leaf). This wind speed is significant enough to carry the spores farther, validating our intuition about the spatial limitation associated with this wind study.

A control experiment was also run, for a diseased leaf without any condensation, to compare the relative importance of wind-induced dry dispersal of spores. For capturing the dry spores, we replaced the water-sensitive papers with adhesive papers. For both the 0.5 m/s and 1.5 m/s wind speeds, no spores were captured by any of the adhesive papers. This is consistent with previous reports on the removal of dry brown rust spores, which found that appreciable spore liberation occurs for wind speeds of at least 1.3 m/s when subjected to short bursts of increasing wind speeds [131] or 4 m/s for continuous wind [24]. Theoretical calculation also suggest a critical wind speed value in the range of 2–10 m/s for the dry micrometric spore removal from the leaf surface (see section B.2). It can therefore be concluded that jumping-droplet condensation is necessary for spores to get liberated under a moderate wind speed, with the wind solely assisting the subsequent dispersal.

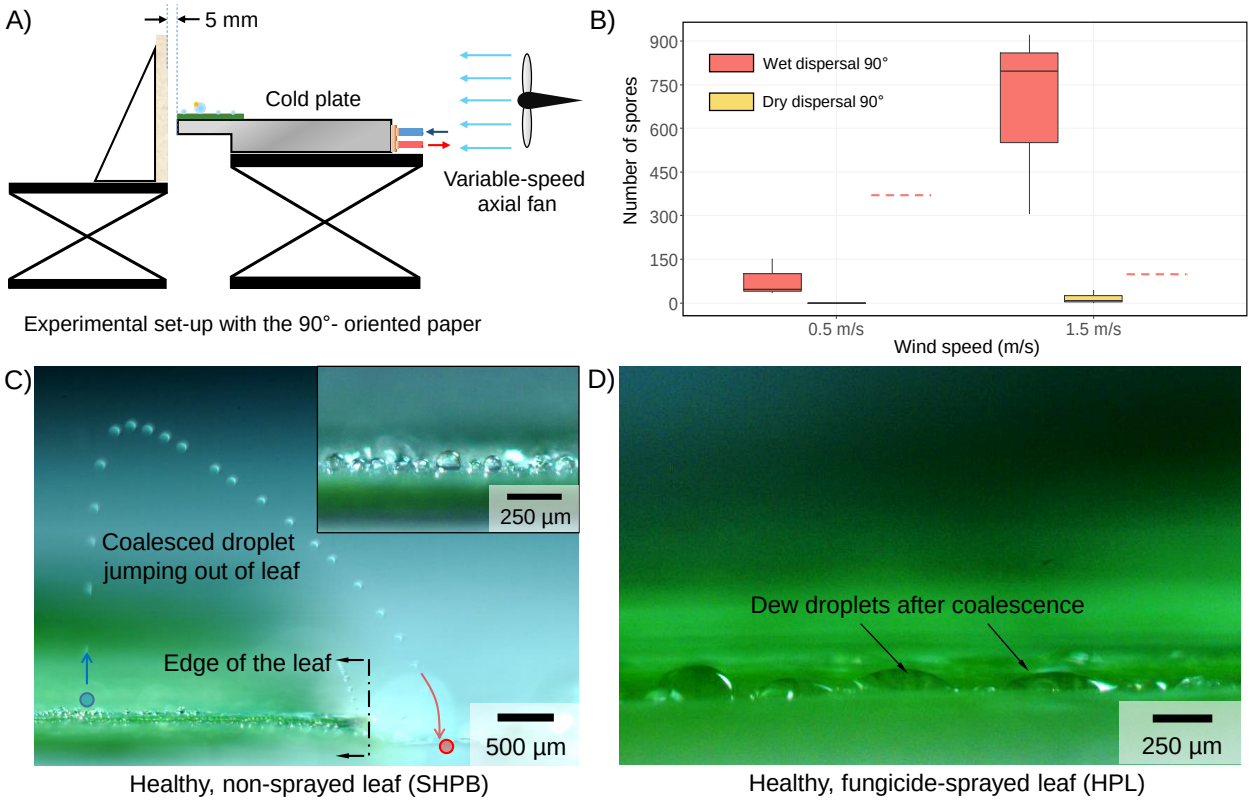

Figure 4.4: Effectiveness of wet dispersal over dry dispersal of spores. (A) A modification of the spore capturing set-up was used to maximize spore capture in wet (both wind and condensation on leaf) and dry dispersal (only wind, no condensation on leaf). A water-sensitive paper or adhesive paper was placed perpendicular to the diseased leaf on the cold stage, depending on wet or dry dispersal, respectively. A variable speed fan was placed some distance away from the leaf to ensure spore dispersal from the leaf. (B) Plot comparing the number of spores captured with jumping droplet-condensation on diseased leaves in presence of wind (wet-dispersal, red) and spore dispersal *via* wind only without any condensation (dry-dispersal, yellow). The dashed red lines for both wind speeds show the total number of captured spores in the long distance set-up of Fig. 4.3B,C. (C) Chronophotograph of a jumping dew droplet on a healthy wheat leaf. Even with no applied wind (only the lab's natural air circulation), the jumped droplet could travel over the edge of the leaf. The blue circle shows the coalescence event that initiated the droplet jumping, while the red circle shows the final impact location beyond the leaf's edge. In the inset, a magnification of the quasi-spherical dew droplets is shown, indicating the superhydrophobic contact angle. (D) Once a healthy leaf was sprayed with fungicide, the contact angle was dramatically decreased. Coalescence of growing dew droplets now resulted in filmwise condensation, rather than jumping-droplet condensation.

4.3.3 Comparison of individual effect of wind and jumping-droplet condensation on the spore dispersal

While Fig. 4.3 quantifies the number of spores dispersed to a given location downwind, it cannot capture the total number of spores being carried away from the diseased leaf. To resolve the latter, we now place a single water-sensitive paper just downwind of the diseased leaf, with the paper held perpendicular to the leaf plane (Fig. 4.4A). As before, we performed three trials for both $V_{\text{wind}} = 0.5\,\text{m/s}$ and $1.5\,\text{m/s}$, using leaves from the same diseased plant to minimize trial-to-trial variability. The fan was turned on once enough condensate droplets appeared on the diseased leaf ($\approx 30\,\text{min}$) and the water-sensitive paper was analyzed after each 1 hr experiment (Fig. S4B). As a control test, we also ran the experiment without any condensation on the diseased leaves (dry dispersal) and using a dry adhesive paper as the perpendicular surface.

The results plotted in Fig. 4.4B show a complete picture of the spore dispersal *via* condensation and wind. The median number of spores captured with $V_{\text{wind}} = 1.5\,\text{m/s}$ was about 800 compared to about 50 for $V_{\text{wind}} = 0.5\,\text{m/s}$, an order of magnitude higher. This reveals that the higher wind speed is a net benefit to the number of dispersed droplets/spores, i.e. the benefit of a thinner boundary layer out-competes the detriment of a reduced rate of condensation growth. In other words, going back to the setup in Fig. 4.3, these present findings indicate there were actually more jumped droplets traveling in the wind for $V_{\text{wind}} = 1.5\,\text{m/s}$, despite the fact that more were able to settle downward for collection onto the papers for $V_{\text{wind}} = 0.5\,\text{m/s}$. Of course, in actual crop fields, the magnitude of dew-induced spore dispersal will depend upon the supersaturation (i.e. rate of growth and coalescence events) and duration of a dew cycle.

The trend of the perpendicular paper capturing more spores at a higher wind speed was also observed for the case of dry dispersal. We found no spores on the adhesive paper for $V_{\text{wind}} = 0.5\,\text{m/s}$ and a maximum of 44 spores at $V_{\text{wind}} = 1.5\,\text{m/s}$. This is consistent with a previous study on the wind removal of brown rust spores (*P. recondita* f.sp. *tritici*, now known as *Puccinia triticina*), which reported $1.3\,\text{m/s}$ as the threshold wind velocity [131]. But perhaps the most significant aspect of the result presented in Fig. 4.4B is the stark contrast in the amount of spore collected in dry dispersal (i.e. only wind) versus a dew cycle where condensation and wind work together. For $V_{\text{wind}} = 1.5\,\text{m/s}$, comparing values of the highest amount of spores collected for the dry dispersal (44 for one trial) with the lowest amount for a dew cycle (305 for one trial) conclusively shows that jumping dew droplets are the primary liberation mechanism for moderate winds, with the wind mostly serving to boost dispersal. The importance of the dew cycle is even more stark for $V_{\text{wind}} = 0.5\,\text{m/s}$, as no spores could be collected from wind alone but a minimum of 33 spores were found during a dew cycle. The results of Fig. 4.3 and Fig. 4.4A and B conclusively show that even in the absence of any rain or strong wind (a necessary pre-condition for a moderate to heavy dew formation), fungal pathogens can still spread via jumping-droplet condensation on the wheat leaves.

For all experiments performed here, the leaves were always fixed to a horizontally-oriented cold plate. This is hardly the case for natural wheat leaves, which can be oriented in all possible inclinations and bend/twist when subjected to wind flow [132]. We suggest that this experimental limitation does not affect the key findings of this study, as it serves as a conservative estimate to spore dispersal. For the no-wind condition, an inclined leaf would increase the number of spore-laden droplets able to jump beyond the leaf's edge, while additionally enabling gravitational rolling for larger droplets [51]. Under windy conditions, the resulting oscillations would increase the number of coalescence events for enhanced droplet jumping [133] and gravitational shedding.

How does spore dispersal from jumping dew and wind compare to rain-induced dispersal? Pathogen dispersal due to raindrop impact occurs via both vortex-induced dry dispersal [115] and splashed droplets [116]. A previous study experimentally demonstrated that a 4.9 mm diameter raindrop impacting a wheat leaf liberated about 8,000 rust spores for a release height of 5 cm and 60,000 for a release height of 100 cm [122]. Their corresponding simulation indicated that for a rain intensity of 10 $\mathrm{mm\,h^{-1}}$, about 2.5^{10}–10^{10} total spores would be removed over a 5 min period. This number dwarfs the amount of spores being liberated and dispersed from jumping dew and a gentle wind, which we measured as roughly 100–1,000 spores/hr for each diseased leaf (cf. Fig. 4.4B). However, we argue that as dew cycles in nature regularly occur in the complete absence of rain, these two modes of spore dispersal are complementary rather than in direct competition.

4.3.4 Suppression of jumping-droplet condensation on wheat leaves

Now that we have identified the synergistic roles of jumping-droplet condensation and wind flow for liberating and dispersing spores, we should consider potential disease mitigation strategies. One approach is to suppress the jumping-droplet effect, which would remove the liberation mechanism that necessarily precedes wind-assisted dispersal. Previous studies of jumping-droplet condensation on engineered surfaces have shown that a superhydrophobic nanostructure is necessary for inflating dew droplets to the quasi-spherical contact angles required for coalescence-induced jumping [21, 25, 59, 68, 84]. Here, we apply a commonly used fungicide that is known to increase the leaf's wettability from superhydrophobic to hydrophilic [117]. Given that the growth and jumping hydrodynamics of dew droplets are not appreciably influenced by the presence of fungal spores [24], for simplicity, we compared condensation on healthy leaves that were either sprayed or not sprayed with the fungicide. On a healthy, non-sprayed leaf, deposited water droplets exhibited advancing and receding contact angles of $\theta_A = 142.4° \pm 1.6°$ and $\theta_R = 138° \pm 2.6°$, respectively. This low contact angle hysteresis ($\theta_A - \theta_R < 10°$) is indicative of the low-adhesion Cassie state [134], confirming the surface is effectively superhydrophobic. In contrast, when the healthy leaves are sprayed with a fungicide (Materials and Methods) and dried before condensation, the advancing contact angle ranges widely from $\theta_A = 0°$–$59°$ and the receding contact angle is almost zero.

Rather than using water-sensitive paper to indirectly characterize jumping behavior, we observed the condensing leaf directly using side-view high-speed microscopy. From the inset of Fig. 4.4C, it can be seen that the dew droplets retain the large (superhydrophobic) contact angles exhibited by deposited droplets. As expected from its superhydrophobic surface wettability, the growth and coalescence of micrometric dew resulted in the jumping-droplet effect for non-sprayed leaves (Fig. 4.4C). Even in the absence of any detectable wind, successive coalescence events resulted in jumped droplets depositing beyond the edge of the leaf. The hydrophilic sprayed leaves, on the other hand, grew dew droplets with hydrophilic contact angles that culminated in filmwise condensation (Fig. 4.4D). These high-adhesion, low-angle droplets are inherently inimical to coalescence-induced jumping. Thus, we have shown that a simple application of a fungicide can suppress the condensation-induced liberation of spores from the leaf surface.

Given that a number of previous reports have shown jumping-droplet condensation on natural surfaces, including wheat leaves [24], lotus leaves [135], and cicada wings [23], proper contextualization of our current work is warranted. While our previous study demonstrated the jumping-droplet-induced liberation of fungal spores from wheat leaves [24], liberation alone is a necessary but not sufficient condition for any disease epidemic. In this study, we have extensively looked into the subsequent dispersal/deposition of the spores on a wide spatio-temporal scale, necessary to facilitate large-scale disease dissemination [136]. We found that even without any detectable wind, rust spores can be liberated and transported to neighboring plants solely via jumping dew droplets. We also showed that long-range dispersal of spore-laden jumped droplets is possible when a light wind flow is introduced. Similar wind, on the other hand, is unable to liberate and disperse dry spores from the leaf surface. This strongly establishes the importance of the dew-induced spore liberation mechanism in wheat crops. A simple and cost-effective solution to suppress the jumping-droplet condensation on wheat leaves is also introduced in this study.

4.4 Conclusion

Jumping-droplet condensation has only recently been discovered as a fungal spore liberation mechanism for wheat leaves [24]. Here, we have shown that even in the absence of any rain or significant wind, jumping-droplet condensation is sufficient to launch pathogenic matter away from a wheat leaf for local dispersal. Further, in the presence of a low wind flow, we have shown that jumped droplets can clear the boundary layer to enable long-range dispersal in the wind. Although our discussion was centered around wheat leaves, there are a wide variety of superhydrophobic plants [135, 137, 138, 139] where jumping-droplet-induced pathogen liberation and dispersal could be similarly important. We were able to completely suppress the jumping-droplet effect by applying a common fungicide to increase the surface wettability of the wheat leaves. These findings indicate the application of a hydrophilic spray could be a simple yet effective solution for halting the ability of dew cycles to spread

disease across crops. Future research could determine whether the jumping-droplet effect could alternatively be halted by seeing how the leaf wettability varies with differing cultivar architectures.

Chapter 5

The Curious Case of Jumping Frost

"But you stand there so nice, in your blizzard of ice"
—One of us cannot be wrong, Leonard Cohen

This chapter was previously published in ACS Nano as a journal article. Adapted with minor modifications with permission from [140] Electrostatic Jumping of Frost, Ranit Mukherjee, S. Farzad Ahmadi, Hongwei Zhang, Rui Qiao, and Jonathan B. Boreyko, ACS Nano 2021 15 (3), 4669-4677, DOI: 10.1021/acsnano.0c09153. Copyright 2021, American Chemical Society. This chapter introduces and analyzes a novel physical phenomena where frost particles jump towards an opposing water droplet.

5.1 Introduction

If we bring an electrically charged rod near a water faucet, the stream of water gets deflected. This simple childhood experiment shows us the remarkable dipolar nature of water molecules, which become partially aligned in the presence of an electric field [141]. Hexagonal ice, on the other hand, cannot exhibit a net alignment even in an electric field [142]. However, colliding ice particles can acquire an electric charge due to a difference in contact potentials [143]. Further, charge separation can occur across ice that exhibits a temperature gradient [144, 145, 146], such that a particle broken off the ice can exhibit a net charge. For example, when air is blown over frost grown on a cold substrate, microscale "splinters" of ice get caught in the flow which exhibit a negative electric charge [147, 148, 149]. Similarly, when a frosted sphere was placed within a humid air flow, frost dendrites were observed to detach into the flow and even explode into multiple pieces [150]. When frost is grown on a wire set at a high voltage, simulating the conditions during a thunderstorm, it can generate charged ice splinters [151, 152, 153] or even water droplets [154].

These previous reports clearly demonstrated that ejected ice particles can carry a charge; however, either a convective air flow [147, 148, 149, 150] or high voltage [151, 152, 154] were required to cause the ejection. Here, we demonstrate that not only splinters of frost, but entire frost dendrites, can break off and jump from a growing frost sheet solely in the presence of an opposing water film or droplet (Figure 5.1a,b). No air flow or applied voltage were required, such that the jumping dynamics could be non-invasively captured with high-speed photography. We show that the attractive force between the frost dendrites and body of water can be extracted from the jumping kinematics and compared to models of charge separation in frost.

5.2 Materials and Methods

Experiments in a room temperature environment

The basic experimental setup for the jumping frost experiments in the laboratory ambient condition is shown in Figure C.1a in Appendix C. A Peltier stage was fixed to a goniometer stage (ramé-hart, Model 590) used for growing frost on different substrates. The default needle assembly with stainless steel needles (inner and outer diameters of 0.7 mm and 2.1 mm, respectively) was used to hold pendant droplets of water or other liquids over the frost sheet. The droplet volume was varied between 1-10 μL by using a syringe pump (ramé-hart, Model 100-22). Slight modifications were done to this existing setup to hold a thin water film opposite to the frosted substrates. A piece of filter paper (Sartorius) was attached with

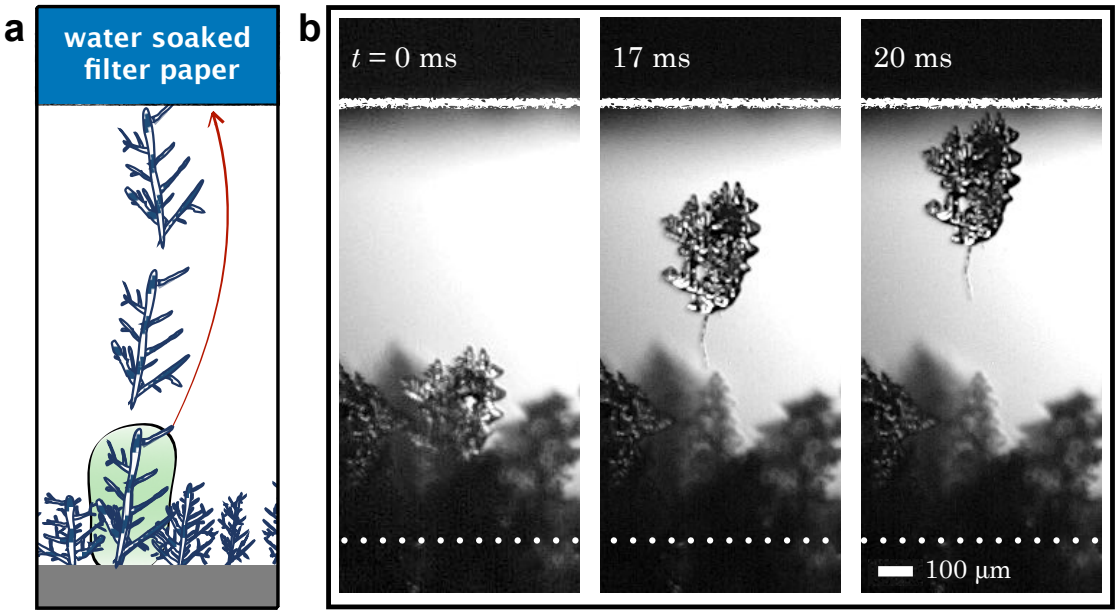

Figure 5.1: The jumping frost phenomenon. (a) When a wet piece of paper is brought above a growing sheet of frost, frost dendrites can break off from the sheet and jump toward the paper. (b) Experimental chronophotograph of a jumping frost event, where an entire frost dendrite detached from its substrate to jump toward a wet filter paper. The dotted line at the bottom visualizes the top face of the substrate from which the frost was grown.

glue to the underside of a 3D printed holder (Figure C.1b). The plastic tube attached to the holder ensured proper fitting with the needle assembly. The syringe pump supplied about 100 μL of water to the filter paper through the needle assembly and the hollow channel. The experiments were recorded from the side with a high-speed camera (Vision Research, Phantom v711) attached to a macro lens (Canon MP-E 65mm f/2.8 1-5X).

Experiments under isothermal conditions

Frost was grown on a hydrophobic silicon wafer ($T_w = -10\,°C$) in the docking room ($T_\infty = 3.2\,°C$, $RH = 73.6\%$) of a walk-in freezer ($T_\infty = -12.7\,°C \pm 0.3\,°C$, $RH = 72.6\% \pm 3\%$). The relative humidity and temperature of the freezer were measured using a humidity and temperature probe (E+E Elektronik, Model EE210). Once the silicon substrate was evenly covered with frost, it was quickly brought into the freezer and left for 10 min before running experiments, to ensure that the frosted surface reached the same temperature as the freezer. Room temperature water and the 3D-printed filter paper holder were brought into the freezer prior to the experiment, to similarly ensure that they cooled down to the freezer's air temperature. Just before the experiment, the filter paper was touched gently on the surface of

the supercooled water to create a film of water and then held over the frosted surface. No jumping was observed over a $\sim$5 min span for each of the three trials.

Effect of air flow on the jumping

A point of concern for the jumping frost experiments was whether air currents could affect the phenomenon. We addressed this issue in two different ways. First, an anemometer with a minimum resolution of 0.3 $\mathrm{m\,s^{-1}}$ (Omega, model HHF81) consistently output a zero value when held near the experimental setup, confirming that no substantive air flow was present. While it is inevitable that the chilled substrate held within a room temperature ambient will induce natural convection, we note that the convective current would be moving toward the substrate, in the opposite direction of the jumping frost. Second, a supplemental series of experiments were conducted within a closed peltier environmental chamber (ramé-hart, Model P/N 100-30, dimensions: $81\times55\times44$ mm), where the jumping phenomenon was similarly observed. These findings cumulatively indicate that the jumping frost phenomenon was not appreciable affected by convective currents for our experiments.

Effect of the substrates and the opposing liquids on the jumping

For all of the experiments reported in the main manuscript, we used hydrophobic silicon wafers to grow frost. Untreated hydrophilic glass and superhydrophilic aluminum were also attempted, all of which exhibited the same jumping frost phenomenon. This indicates that the jumping frost phenomenon can occur on substrates where wettability, electrical conductivity, and thermal conductivity widely vary. However, we do expect that the hydrophilic surface will exhibit a higher frequency of frost dendrites from the ice-substrate interface (as opposed to breaking off from mother frost) because of the reduced ice adhesion strength.[155] On the hydrophilic and superhydrophobic substrate, the dendritic frost growth was preceded by the freezing of supercooled filmwise condensation.[156] As this is not fundamentally different from growing frost from an ice sheet, we believe that the same jumping frost effect would have been observed if the substrate was initially covered in ice.

Water droplets and films were used in most of the experiments, but additional liquids such as acetone, ethylene glycol and decane were also used. For acetone and ethylene glycol, which are both polar due to the presence of more electronegative oxygen atoms, jumping dendrites were observed similar to the case of water. When a thin film of decane, a hydrocarbon, was used as the opposing liquid, no jumping was observed for as long as 5 min.

Image processing

An open-source software (Tracker) was used to track the jumped icicles over time and obtain the velocity *vs.* time plot shown in the main text Figure 6.1d. For each case, $t = 0$ is chosen as the frame preceding the complete breakage of a frost dendrite. The origin of the coordinate system was placed at the point of contact of the jumping icicle with the substrate or the mother frost.

5.3 Results

Our experimental setup involves growing frost on a substrate and placing a liquid droplet or film at some height above the substrate (Figure 6.1a,b). We used a completely dry hydrophobic silicon wafer which was thermally bonded to a Peltier stage set at $T_w = -10 \pm 1°C$ within a room temperature environment (air temperature $T_\infty = 25 \pm 0.5°C$ and relative humidity $RH = 40 \pm 10\%$). To suspend water above the silicon substrate, a 2 cm × 2 cm filter paper was attached to a 3D-printed holder which was connected to a syringe pump. The out-of-plane gap between the silicon and wetted paper was varied as $H = 1$ mm, 2.5 mm, or 5 mm. Initially, the filter paper remained dry while frost was grown on the chilled substrate *via* condensation frosting [157]. When the frost sheet grew to a desired thickness, typically in the range of $h \approx 120$–$800\,\mu$m, approximately 100 μL of water was dispensed onto the filter paper (Figure 6.1b). As soon as the paper became saturated with water, several of the dendrites within the frost sheet began to twist and turn.

Periodically, one or more of the micrometric dendritic branches or "splinters" would break off from the frost sheet and jump towards the wetted paper (Figure 6.1c). Jumping dendrites exhibited an initial acceleration of order $a \sim 10$ g and traversed the gap within $t \sim 1$–10 ms. These jumping events tended to begin around ~ 10 s after wetting the paper and continued intermittently until the frost growth began to taper off. This jumping frost effect was also observed on hydrophilic glass non-metal as with the silicon wafer) and a superhydrophilic aluminum hydroxide surface (metal), indicating that the phenomenon can occur over a wide variety of surface wettabilties and irrespective of differences in the thermal and electrical conductivities. As micrometric frost splinters jumped with greater frequency than entire (millimetric) dendrites, while also exhibiting a simpler shape, we focus our attention on the splinters as a model system to understand the mechanisms behind the jumping phenomenon. At the same time, the analysis will remain conceptually valid for the more dramatic case of whole frost dendrites jumping.

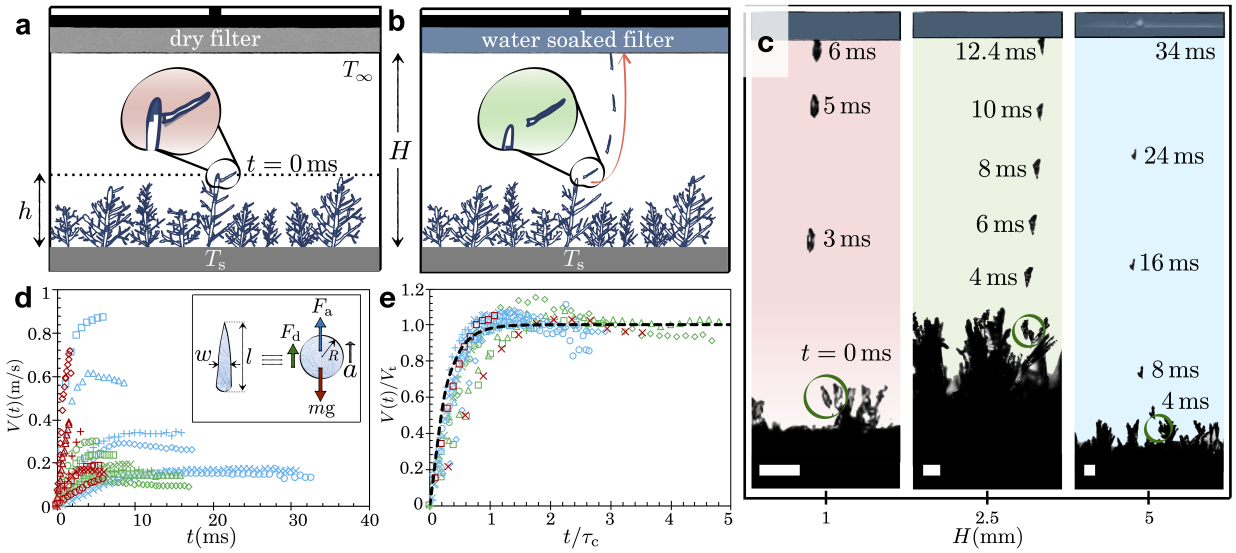

Figure 5.2: Dynamics of the jumping frost. (a) Schematic of the experiment: frost was grown to an average height h on a sub-zero temperature (T_s) substrate. A filter paper was suspended at a variable height H above the frosted substrate. (b) Shortly after adding water to the filter paper, frost particles broke off and jumped towards the water-soaked paper. (c) Chronophotography of a micrometric jumping frost particle, from the instance of break-off ($t=0$) until it reaches the wet filter paper, for three different cases of $H=1$ mm (red), 2.5 mm (green) and 5 mm (blue). All scale bars represent 100 μm. (d) Dimensional plot of jumping velocity *vs* time for frost particles jumping toward the suspended wet filter paper. The color scheme of the data points matches that of Figure 6.1c. (Inset) Free body diagram of the spherical approximation of an irregularly shaped dendrite. (e) Equivalent non-dimensional plot, where all data collapse onto a universal theory line.

5.3.1 Dynamics of Jumping Frost

The velocities of the jumping frost were plotted against time for different H (Figure 6.1d). Typical to the motion of an object in a fluid, the velocity of the frost increased continuously and then attained a terminal velocity mid-jump before reaching the wetted paper. A force balance on the jumped frost particle of mass m and velocity $v(t)$ yields $m\frac{dv(t)}{dt} = F_a - F_g - F_d$, where F_a is the attractive force between the dendrite and the water, F_g is the force of gravity, and F_d is the drag force (Figure 6.1d, inset). By approximating the jumping dendrite as a perfect sphere of radius R, we can assume a Stokes drag of $F_d = 6\pi\mu R v(t)$, where μ is the viscosity of the air. The area of the real-life dendrite was approximated as its projected area, $A \sim lw$, where l and w are the in-plane length and width and it is assumed that the dendrite is very thin. This same surface area was then mapped onto a perfect sphere to extract the effective sphere radius (R). The assumption of Stokes drag is supported by the micrometric radius of a typical jumping dendrite ($R \approx 10\,\mu$m), such that the maximum Reynolds number

of the vapor flow around the jumping dendrite is only $Re = \rho V_{\max}(2R)/\mu \approx 1.2 \approx 1$, where $\rho = 1.2\,\mathrm{kg\ m^{-3}}$ and $\mu = 18\,\mu\mathrm{Pa\ s}$ are the air density and dynamic viscosity, respectively. The maximum observed velocity of the jumped dendrites $V_{\max}$ among all trials is about $0.9\,\mathrm{m\ s^{-1}}$. Solving the force balance for $v(t)$, with the initial condition of $v(0) = 0$, we obtain:

$$v(t) = V_t \left[1 - e^{-\frac{t}{\tau_c}}\right], \tag{5.1}$$

where $V_t = (F_a - mg)/(6\pi\mu R)$ is the terminal jumping velocity and $\tau_c = m/(6\pi\mu R) = 2R^2\rho_i/9\mu$ is the characteristic relaxation time for reaching terminal velocity, with ρ_i being the density of ice. If the time to reach the water film, τ_e, is longer than τ_c, the velocity of the dendrites will reach the steady velocity. This was always the case for $H = 3$ and $5\,\mathrm{mm}$, whereas for $H = 1\,\mathrm{mm}$ a steady velocity was only reached for the smallest particle sizes (due to the R^2 dependence of τ_c). We can now non-dimensionalize the experimental time with τ_c and the velocities with the corresponding experimental steady velocity for all the experiments where the dendrites reached a steady velocity. Figure 6.1e shows all the non-dimensional experimental data collapsed over the theoretical curve from Equation 5.1. We can thus use the experimentally measured values of V_t to extract F_a. For a typical case of particle radius $R \approx 10\,\mu\mathrm{m}$, $\rho_i = 917\,\mathrm{kg\,m^{-3}}$, $\mu \approx 9.8\,\mu\mathrm{Pa\,s}$, and $V_t \approx 0.1 - 0.9\,\mathrm{m\,s^{-1}}$ we obtain an order of magnitude estimate for the attractive force $F_a \sim 10^{-10} - 10^{-9}\,\mathrm{N}$. But now we need to understand the mechanistic origins for this attractive force.

5.3.2 Charge Separation in Ice: Temperature Gradient Theory

Informed by previous reports of charge separation occurring in bodies of ice that exhibit a temperature gradient [144, 145, 146], we hypothesize that the attractive force is electrostatic in nature. This hypothesis was tested by suspending a wide variety of polar *vs* non-polar liquids above the frost sheet (see Figure C.2). The jumping frost effect was consistently observed when dangling a pendant drop of a polar liquid: water, acetone, or ethylene glycol, over the frost sheet. In contrast, no jumping frost was ever observed when suspending non-polar droplets of decane or hexadecane. Similarly, no frost dendrites fractured or propelled from the surface when using dry filter paper (or not suspending any object at all). While electrostatic charge can develop in these liquids flowing through a channel due to the streaming current phenomenon [158], this was not the primary mechanism in our case. The flow-independent electrification of our system was validated by two separate observations: jumping was observed when using static pendant droplets or by gently submerging the filter paper in water (rather than using a syringe pump). Triboelectric charging of the filter paper can also be neglected, as dry filter paper did not promote frost jumping. Cumulatively, these observations strongly indicate that the frost exhibits a charge separation that in turn

polarizes the opposing liquid to produce an electrostatic attractive force.

The spontaneous electrification of ice has been studied intensively and almost exclusively by the atmospheric community to understand thunderstorms, especially in the mid-twentieth century [144, 145, 146, 148, 159, 160]. The electrical state of chemically pure ice is dominated by its intrinsic charge carrying defects: ionic defects H_3O^+ and OH^- (denoted by m and q) and rotational Bjerrum D (positive) and L (negative) defects (d and l) [161, 162, 163, 164], all of which are formed spontaneously by thermal activation. The thermoelectric theory put forward by Latham and Mason [145, 159] described a temperature gradient-induced charge separation in an ice slab. The warmer end of the ice will have a higher concentration of thermally activated ionic defects, prompting their diffusion toward the colder end. As H_3O^+ diffuses about 3.3 times faster than OH^-, this creates a potential difference across the ice with the warm and cold ends exhibiting net negative and positive charges, respectively [146].

Let us now apply the Latham and Mason theory of charge separation to our specific case of a dendritic frost sheet grown in warm air. Upon the earliest nucleation of nanoscale frost, the temperature gradient is negligible such that the ionic defects are evenly distributed (Figure 5.3a). As the dendrites continue to grow outward from the nanoscale frost, their top ends will increasingly warm (eventually approaching the melting temperature), while the base of the frost is maintained at the temperature of the chilled substrate. As a result, the upper portion of the frost will become negatively charged while the basal frost becomes positively charged (Figure 5.3b). To validate that the charge separation in frost was required for dendrites to become attracted to the opposing water, we performed a control experiment with an isothermal frost sheet in a walk-in freezer. As expected, when the frost lacked an appreciable temperature gradient, the jumping effect was suppressed even when holding water over the frost. To apply our numerical model, we crudely approximate a three-dimensional frost sheet as an ice slab of thickness h (Figure 6.1a). The negative surface charge density on the vapor side of the frost sheet can now be estimated from the modified Latham and Mason model [145]:

$$\sigma_s = \frac{\epsilon_r \epsilon_0 k_B}{2e} \left(\frac{u^+/u^- - 1}{u^+/u^- + 1} \right) \left(\frac{\phi_e}{k_B T} + 1 \right) \frac{\Delta T}{h} \, \mathrm{C/m^2}, \tag{5.2}$$

where $\epsilon_r = 100$ is the relative permittivity of ice, k_B is the Boltzmann constant, $\phi_e = 1.08\,\mathrm{eV}$ is the activation energy to create H_3O^+ and OH^- ions in ice [164], e is the elementary charge, $\frac{\Delta T}{h} \approx \frac{dT}{dX}$ is the temperature gradient across frost of thickness $h = 100\,\mu\mathrm{m}$, and u represents the mobility of the ions within ice where the $+$ and $-$ subscripts denotes H_3O^+ and OH^- ions, respectively. In general, the H_3O^+ ions are more mobile than the OH^- ions and the mobility ratio u^+/u^- is about 3.3 [164]. For the average dendrite temperature T, we can use the average of the equilibrium ice-water interface temperature ($T_m \approx 0°\mathrm{C}$) and the substrate temperature ($T_w = -10°\mathrm{C}$) [165]. The total change in temperature across the frost is approximated by $\Delta T \approx T_m - T_w \approx 10°\mathrm{C}$. With the temperature gradient $\approx 10/10^{-4} = 10^5\,\mathrm{K\,m^{-1}}$, the negative surface charge density on the frost plate is found out to be $\sigma_s = 9.86 \times 10^{-8} \sim$

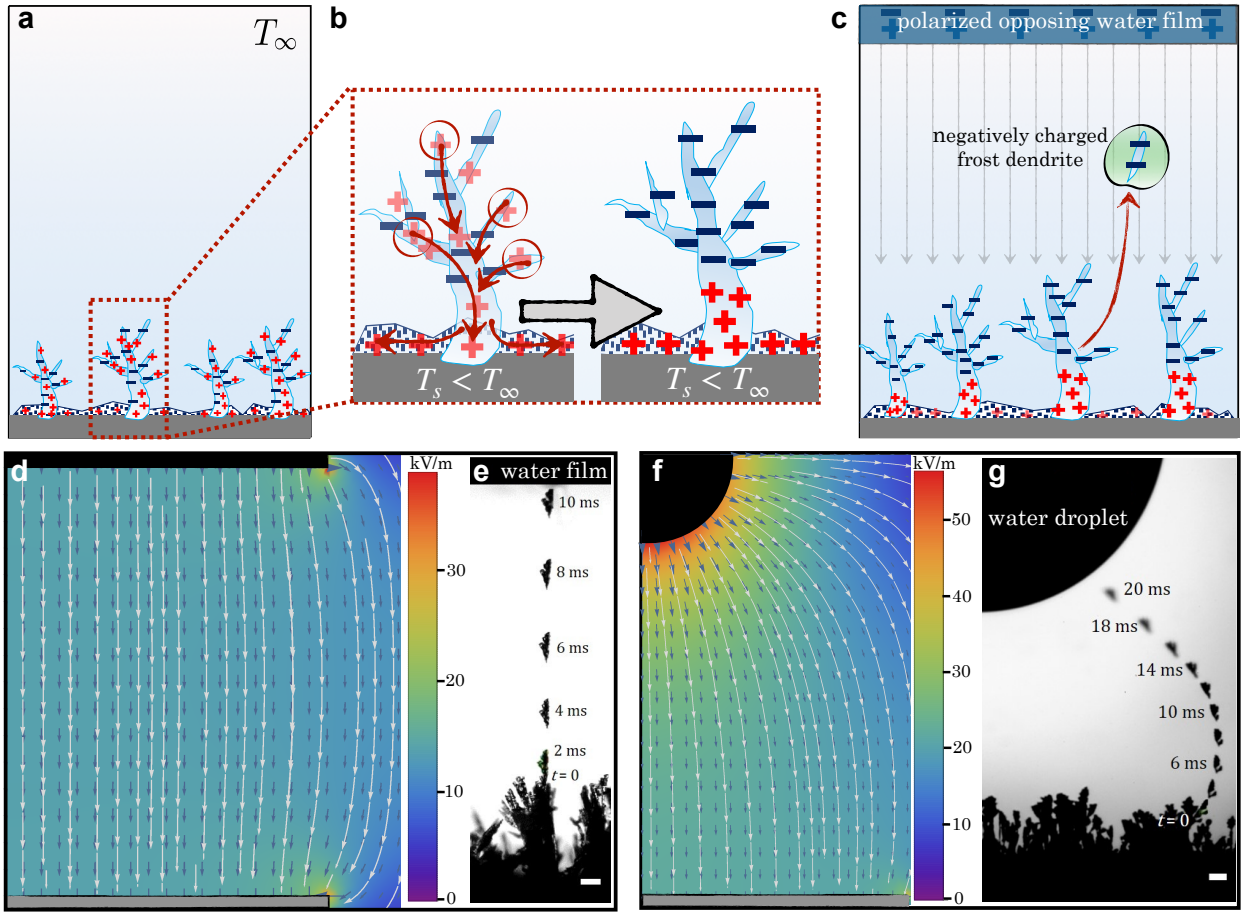

Figure 5.3: The origin of the attractive force on the frost dendrites. (a) Initial (nanoscale) frost exhibits a roughly uniform temperature and distribution of ions (defects) within the dendrites. (b) As the frost dendrites grow to a microscale, $T_\infty > T_s$, such that ions are more concentrated in the warmer upper dendrites. Positive ions then diffuse to the lower concentration basal frost at a much higher mobility than the negative ions. (c) This charge separation enables the fracture and jumping of frost in the presence of an opposing polarizable liquid. (d) Numerical simulation showing that, when the frost and opposing water film are both planar, the electric field is uniform. (e) This results in a straight trajectory and constant terminal velocity for jumping frost particles, validated here by chronophotography where the particle consistently travels $\approx 300\,\mu$m every 2 ms at terminal velocity to cross the 2.5 mm gap. (f) Numerical simulation showing that, when frost is now opposite a pendant droplet (*i.e.* plate and sphere configuration), the electric field is non-uniform with curved field lines. (g) Chronophotography (successive position of the dendrite temporally separated by 2 ms) confirms a curved trajectory for a jumped dendrite opposite a water droplet, where the sudden increase in acceleration near the droplet is confirmed by increased distance between successive positions. Both scale bars represent $100\,\mu$m.

$10^{-7}\,\mathrm{C\,m^{-2}}$.

5.3.3 Origin of the Attractive Force on the Frost

These negative charges on the upper frost induce positive charges on the nearest polarizable surface, *i.e.* the opposing water. Of course, there will be an equal amount of negative charges within the water film which will be reoriented away from the frost plate. Thus an external electric field is set up between the frosted surface and the opposing water surface (Figure 5.3c). A broken piece of frost carrying a negative surface charge [147] will move upward, as this corresponds to the opposite direction of the electric field. As the relative dielectric permittivity of water is much higher than the surrounding medium ($\epsilon_{\mathrm{water}} \approx 80, \epsilon_{\mathrm{air}} \approx 1$), the internal electric field can be neglected and we can treat the water film (droplet) as a conducting plate (sphere) with positive surface charges [166] (see section C.1 and Figure C.4).

The case of a frosted surface and an opposing water film (Figure 5.3d) can be compared with a parallel plate capacitor, as the plate areas ($\approx 100\,\mathrm{mm^2}$) are larger than the spacing between them ($H \sim 1\,\mathrm{mm}$). A uniform field of strength $E = \sigma_{\mathrm{s}}/\epsilon_0 \approx 10^4\,\mathrm{Vm^{-1}}$ was found from subsequent analysis (Figure 5.3d). The charge q_{f} on a frost dendrite broken off the frost is found to be in the range of $10^{-14} - 10^{-13}\,\mathrm{C}$ from the electrostatic force equation, $F_{\mathrm{a}} = q_{\mathrm{f}}E$ where $F_{\mathrm{a}} = 10^{-10} - 10^{-9}\,\mathrm{N}$ as found previously. We avoided any experimental setup to directly measure this charge on frost dendrite, as the measurement process would have likely induced error due to the temperature gradient and humidity in the vicinity of our frosted surface [167]. But previous reports on fragmented frost dendrites have reported similar amaount of charge from direct measurement, which gives us enough confidence in our minimal model [148, 152]. The uniform electric field lines between the substrate and the film explains the experimental observation of the straight path of the jumped dendrite (Figure 5.3e). For the case of an opposing water droplet in place of a water film, we simulated the electric field by solving Laplace's equation in the space between the substrate and the droplet (see section 2.2 in Supporting Information). The simulation results are shown in Figure 5.3f, which shows that the electric field is non-uniform and increases as we go near the droplet. Moreover, the field lines curve into the water droplet at a right angle following the rule that flux is perpendicular to the surface. This matches with our experimental observation of the curved droplet trajectory in Figure 5.3g and the increased acceleration of the dendrite near the droplet (see Appendix 3.3c). The numerically simulated electric field values also matches with the results achieved through simpler scaling analysis (see section 2.3 in Supporting Information).

5.3.4 Charge Separation in Ice: Numerical Simulation

At this point, it is important to generalize this charge separation theory for the case of an entire frost dendrite breaking off from the surface (Figure 5.1b). Generally, the three dimensional frost dendrites do not grow directly on the surface but over an icy basal layer which can be discontinuous or continuous, depending on the wettability of the substrate. Since a temperature gradient is the primary driving force of the frost jumping, the ambipolar transport of the ionic defects happens between the surfaces having the largest temperature difference, *i.e.* between the icy layer contacting the surface and the frost-air interface. This way even an entire dendrite can carry a negative charge while the positive charges stay in the basal layer. The schematic of Figure 5.3a-c shows this progression of events from the frost growth until the jumping.

To complete our understanding of charge separation in ice due to a temperature gradient, a numerical simulation approach to Equation 5.2 is presented here , for a column of ice with the same $h = 100\,\mu$m thickness and temperature increasing linearly from the right side to the left side (Figure 5.4a). Without any temperature gradient, there is a balance of H_3O^+-OH^- ions in the bulk ice, whose equilibrium is maintained by the mass action law:

$$\rho_m \rho_q = \rho^0(T)^2, \tag{5.3}$$

where ρ_m and ρ_q are the ion densities (or concentrations) of the OH^- and H_3O^+ ions in the bulk ice and $\rho^0(T) = \rho_m^0(T) = \rho_q^0(T) = Ne^{-\phi_{qm}/(2k_BT)}$ is the temperature-dependent equilibrium density of the OH^- and H_3O^+ ions. $N = 3\times10^{28}\,\mathrm{m}^{-3}$ is the concentration of water molecules in ice and $\phi_{qm} \approx 1.08\,$eV is the activation energy for the ions. Although the mass action law is strictly valid only in thermal equilibrium, as a quasi-equilibrium is maintained in the ice in the presence of the thermoelectric effect, the mass action law still holds locally across the entire ice slab.

Once a small temperature gradient is induced in the slab (increasing from right to left side of the slab), accompanying concentration gradients of H_3O^+ and OH^- ions appear in the slab. These gradients lead to the diffusive movement of H_3O^+ and OH^- ions. Due to the higher mobility of H_3O^+ ions, charge separation occurs within the ice slab with H_3O^+ (OH^-) ions enriched at ice slab's colder (warmer) side. This in turn sets up an internal ambipolar electric field which opposes the movement of the H_3O^+ ions. Eventually, the balance of electric field-driven transport and diffusion transport leads to a steady-state potential with no net current flow. The ambipolar electric field can be derived at the steady-state [168]. The governing equations for the spatio-temporal variation in the ion concentrations are:

$$\frac{\partial \rho_m}{\partial t} = \frac{\partial}{\partial x}\left[D_m \frac{\partial \rho_m}{\partial x} + \mu_m \rho_m E\right] + \frac{\rho_m^0(T)}{\tau_{mq}} - \frac{\rho_m \rho_q}{\rho_m^0(T)\tau_{mq}}, \tag{5.4}$$

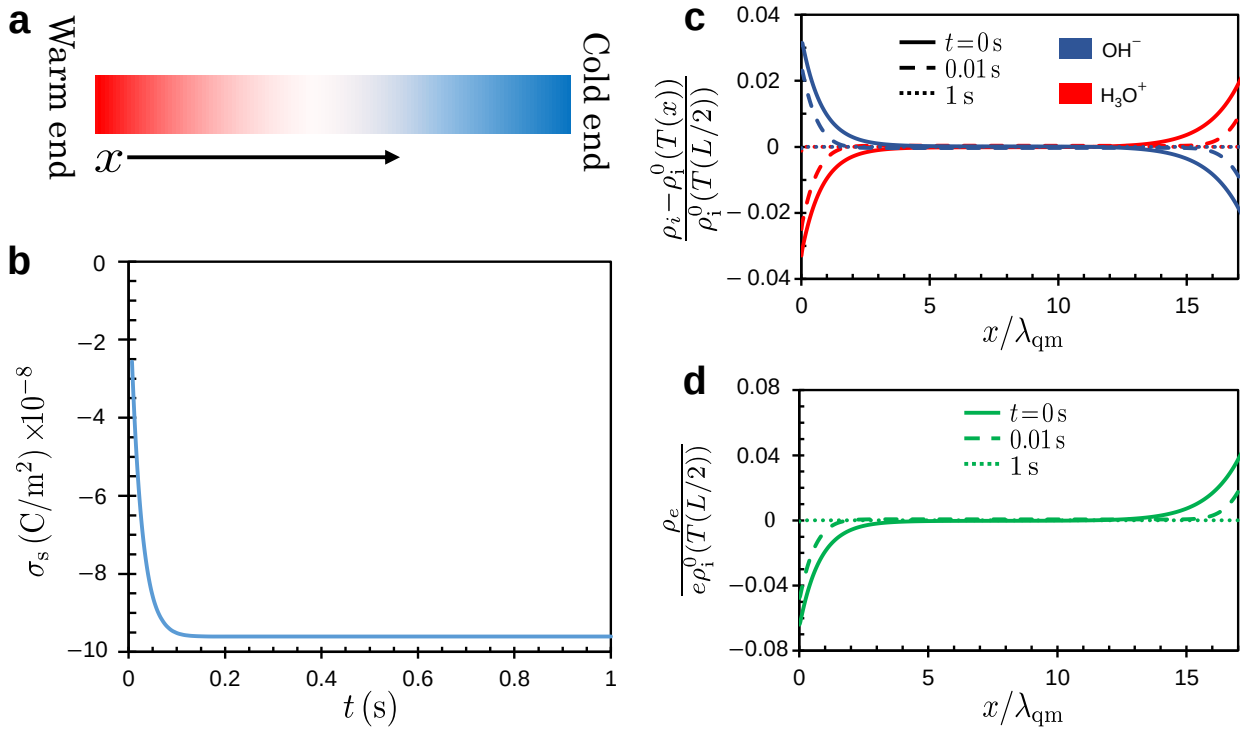

Figure 5.4: Numerical simulation for charge separation in an ice slab. (a) The one dimensional ice slab model with the temperature increasing linearly from the left to the right end. The positive x-axis is along the direction of increasing temperature. (b) Temporal variation of charge density in the slab's warmer left half, due to the mismatch in mobility of the OH^- and H_3O^+ ions. The negative sign of the charge density shows that the negative charges accumulate on the warmer end of the ice. The steady state value of the surface charge density is very close to the value obtained from Latham and Mason's original formula. (c) Spatial distribution of the non-equilibrium density of OH^- and H_3O^+ ions at representative times. (d) Spatial distribution of space charge density of the ionic defects at representative times.

$$\frac{\partial \rho_q}{\partial t} = \frac{\partial}{\partial x}\left[D_q \frac{\partial \rho_q}{\partial x} - \mu_q \rho_q E\right] + \frac{\rho_q^0(T)}{\tau_{mq}} - \frac{\rho_m \rho_q}{\rho_q^0(T)\tau_{mq}}, \tag{5.5}$$

$$\frac{\partial E}{\partial x} = \frac{e(\rho_q - \rho_m)}{\epsilon_0 \epsilon_r}, \tag{5.6}$$

where $\mu_m \approx 3\times10^{-8}\,m^2V^{-1}s^{-1}$ and $\mu_q \approx 10^{-7}\,m^2V^{-1}s^{-1}$ are the mobility of the OH^- and H_3O^+ ions, respectively, E is the intensity of the electric field set up by the space charge, e is the elementary charge, $\epsilon_r = 100$ is the relative dielectric permitivitty of ice, and $\tau_{mq} = 2\times10^{-5}\,s$ is the recombination time for the ions[164]. The first two terms on the right side of Equations 5.4 and 5.5 are simply Fick's law and Ohm's law, respectively, describing the

contribution of ion concentration and internal electric field on the transport of ions. As both of these processes are related, the coefficients of the first two terms are also related by the Einstein relation, $D_{\mathrm{m,q}} = \mu_{\mathrm{m,q}} k_{\mathrm{B}} T/e$. Although these were present in the original Latham and Mason model, a more general model of ion migration dynamics should also include a net volumetric source term[169]. The last two terms in Equations 5.4 and 5.5 account for the generation and annihilation (or recombination) of ions respectively, following the mass action law. Together they constitute the volumetric source term or the net charge produced within the ice.

These equations can now be solved simultaneously (details of simulation process and parameters are given in Appendix C.2), with the following boundary conditions defined at the left and right side of the ice slab:

$$J_{\mathrm{m}}(0) = J_{\mathrm{m}}(L) = 0, \tag{5.7}$$
$$J_{\mathrm{q}}(0) = J_{\mathrm{q}}(L) = 0, \tag{5.8}$$
$$E(0) = E(L) = 0, \tag{5.9}$$

where the fluxes of the OH^- and H_3O^+ ions are depicted by $J_{\mathrm{m}}(x) = -D_{\mathrm{m}} \frac{\partial \rho_{\mathrm{m}}}{\partial x} - \mu_{\mathrm{m}} \rho_{\mathrm{m}} \cdot E$ and $J_{\mathrm{q}}(x) = -D_{\mathrm{q}} \frac{\partial \rho_{\mathrm{q}}}{\partial x} + \mu_{\mathrm{q}} \rho_{\mathrm{q}} E$. We have assumed two mathematical planes with no charge at either ends of the slab at $t = 0$. These are not physical planes, but as the charges accumulate with time close to these planes, real planes are formed.

Figure 5.4b shows the evolution of the net charge of OH^- and H_3O^+ ions in the left half of the ice. We can see that the net charge density reaches a steady state, $\sigma_{\mathrm{s}} = 9.6 \times 10^{-8}\,\mathrm{C\,m^{-2}}$, after about 0.1 s. This is very close to the value $\sigma_{\mathrm{s}} = 9.86 \times 10^{-8}\,\mathrm{C\,m^{-2}}$ we got in the main text using the original Mason's formula. The small difference is caused by the fact that unlike Mason's model, we have not considered the thermally driven transport of the OH^- and H_3O^+ ions in Equations 5.4 and 5.5. The negative sign on the accumulated charge on the warmer left hand side of the ice slab confirms the temperature gradient-induced charge separation process in ice where the warmer end accumulates a net negative charge. The spatial distribution of the concentration of these ionic defects and net charge density is also shown at some representative times (Figure 5.4c,d). In Figure 5.4c, the non-equilibrium density of the ionic defects, $\rho_{\mathrm{i}} - \rho_{\mathrm{i}}^0(T(x))$, is non-dimensionalized by the equilibrium density of the ions at the middle of the ice slab, $\rho_{\mathrm{i}}^0(T(x = L/2)$, which is same for $\mathrm{i} = m, q$. The spatial distance is non-dimensionalized by the Debye length of the ionic defects, $\lambda_{\mathrm{qm}} = \sqrt{\epsilon_0 \epsilon_r k_{\mathrm{B}} T / 2 \rho_{\mathrm{i}}^0 e^2}$. The charge separation only happens within few Debye length distance in each end while the bulk region remains neutral. In Figure 5.4d, the spatial variation of the space charge density, $\rho_{\mathrm{e}} = e(\rho_{\mathrm{q}} - \rho_{\mathrm{m}})$, is plotted for different times which shows the concept of Debye length clearly.

5.4 Fracture of a Frost Dendrite from the Frost Sheet

The last piece of the puzzle is the fracturing of the frost dendrites, from either the substrate or "mother" frost, that is a prerequisite for the subsequent jumping. High-speed microscopy indicates two distinct modes of fracture. In one mode, the area where fracture occurs is approaching a point contact ($l_a \lesssim 1\,\mu$m length scale), such that breakage occurs instantaneously with respect to the temporal resolution of the high-speed video (Figure 5.5a–c). In contrast, when the length scale of attachment is more than $l_a \gtrsim 10\,\mu$m, the dendrite(s) twists and turns before complete breakage (Figure 5.5d–f). We hypothesize that these two seemingly different mechanisms of fracture are related by the rate of crack propagation in ice. Although finding the exact crack propagation rate in ice under tensile stress requires the precise knowledge of its grain structures, here we use scaling analysis to capture the physics.

From the Griffith condition for crack initiation, the nucleating crack length r_0 can be found by equating the attractive force with the crack initiation force [170, 171],

$$F_a = \pi {r_0}^2 \sqrt{\frac{8 E_i w_{ad}}{(1-\nu^2)\pi r_0}}, \tag{5.10}$$

where E_i =8.7 GPa is the modulus of elasticity of ice, $w_{ad} \approx 2\gamma_{i,a} = 0.2\,\mathrm{J\,m^{-2}}$ is the work of adhesion inherent to creating an ice-air double interface, and $\nu = 0.31$ is Poisson's ratio for ice. Using our previously obtained scaling estimate of $F_a = 10^{-10} - 10^{-9}$ N in Equation 5.10, the nucleating crack length can be solved as $r_0 \sim 10^{-10}$ m. We can then express the overall stress intensity factor, assuming the tensile loading of an edge crack of length r_0, as $K_I \sim \sigma_\infty \sqrt{\pi r_0}$, where $\sigma_\infty = F_a/\pi {l_a}^2$ is the applied stress [172]. The maximum applied stress due to the maximum force $F_a = 10^{-9}$ is $\sigma_\infty \sim 10^4$ Pa for a submicron contact point ($l_a \sim 100$ nm) and $\sigma_\infty \sim 1$ Pa for a micron-sized area of contact ($l_a \sim 10\,\mu$m). This translates to stress intensity factors of $K_I \sim 1\,\mathrm{Pa\,m^{1/2}}$ and $10^{-4}\,\mathrm{Pa\,m^{1/2}}$, respectively, far less than the fracture toughness of ice, $K_{Ic} = 10^5\,\mathrm{Pa\,m^{1/2}}$. We will therefore assume a subcritical crack growth velocity, which for brittle materials tends to scale as $v_c \sim 1\,\mathrm{mm\,s^{-1}}$ [173]. For such a crack to propagate and completely detach the dendrite from the substrate or the "mother" frost, it would take about $l_a/v_c \sim 10^{-7}/10^{-3} \sim 100\,\mu$s for a 100 nm attachment (Figure 5.5a,c) and about $l_a/v_c \sim 10^{-5}/10^{-3} \sim 10$ ms for a 10 μm contact length (Figure 5.5d,f). The experimental videos were recorded at $\sim$10 kHz (100 μs per frame), such that the temporal resolution was approximately equal to the crack propagation time for the case of a 100 nm attachment. This explains why complete detachment appears to be instantaneous in the case of submicron attachments. In contrast, crack propagation along a 10 μm contact length would require $\sim$100 frames to complete, which is what enabled the visualization of the twisting and turning motions prior to detachment. This scaling estimate for the crack propagation time matches with our experimental observations, where 440 frames (averaged across three

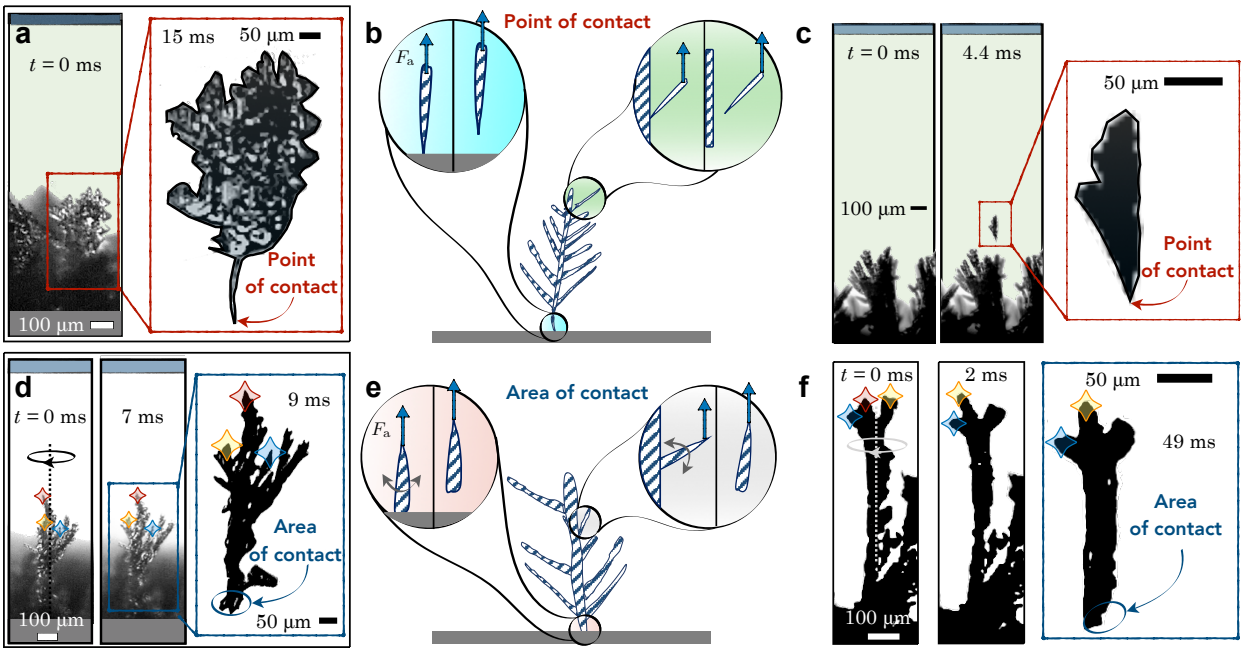

Figure 5.5: Mechanisms of frost break-off. (a) For a sub-micron point of attachment with the substrate, frost break-off occurs seemingly instantaneously. (b) Schematic showing how the point-break fracture of a dendrite can either occur from the substrate or from "mother" frost. (c) Point-break frost detachment from mother frost. (d) Area fracture (*i.e.* micro-scale attachment length scale) of a dendrite from the substrate. The twisting motion of the dendrite is evident from the change in positions of the three branches (yellow, red and blue colored) in the first two frames. The axis and direction of rotation is shown to help in the visualization. It takes about 7 ms from the beginning of the twisting motions to the completion of crack propagation and break-off. (e) Schematic showing the twisting and/or turning motion before the complete fracture of a dendrite from either the substrate or mother frost. (f) Area fracture from mother frost. $t = 0$ denotes the start of movement for the dendrite. At $t = 2$ ms, the yellow and blue dotted branches can be seen at a different location while the branch with the red dot has moved into the page and is obscured from the viewer. All zoomed-in photographs in (a), (c), (d), and (f) show the full shape of the detached frost mid-flight, with a digital outline for visual clarity. The snapshots are from Movie 5.

trials) were required from the initiation of twisting and turning to the complete detachment of $l_a \sim 10\,\mu$m attachments prior to jumping.

5.5 Conclusion

While the spontaneous charging of growing ice particles has been studied by atmospheric physicists to understand cloud electrification during thunderstorm [147, 159, 174], the analogous charge separation of frost growing on substrates has been largely ignored by surface scientists. Here, we reported that micrometric frost growing on a chilled surface can dramatically fracture and jump into the air in the presence of polarizable liquids. Our experiments and analysis, correlated with Latham and Mason's classic model, revealed that such motion results from the temperature gradient-induced charge separation within a growing layer of frost and consequent electrical attraction by the opposing liquid. Our simple approach of correlating the high-speed imaging of jumping ice particles with a dynamical model allows for the controlled laboratory study of charge separation in ice, which may help atmospheric physicists to better understand thunderstorm electrification. Conversely, the findings described here could be stepping stones for the development of an electrostatic de-icing technique, where we envisage that high voltage electrodes could replace the water film to propel larger masses of ice from their substrate.

Chapter 6

Oil-Impregnated Hydrocarbon-based Polymer Films

"I keep coming back here where everything slipped. But I won't spill my guts out"

–Slipped, The National

This chapter was published (and can be reproduced) as an article [175] (Mukherjee, R., Habibi, M., Rashed, Z.T. et al. Oil-Impregnated Hydrocarbon-Based Polymer Films. Sci Rep 8, 11698 (2018), DOI: 10.1038/s41598-018-29823-7) under the terms of Creative Commons Attribution 4.0 license. This is reproduced here with minor modifications. This chapter experimentally demonstrates a procedure to design an omni-repellent liquid-infused surface from hydrocarbon-based polymer films.

6.1 Introduction

Slippery liquid-infused porous surfaces (SLIPS) exhibit remarkable properties such as ultra-low contact angle hysteresis (CAH) for a wide variety of liquids[35, 37], excellent self-healing capability[37, 176], and stability under high pressures or temperatures[37, 177, 178]. In addition to repelling liquids, SLIPS have been shown to promote anti-fouling[179, 180, 181, 182, 183, 184, 185, 186], self-cleaning[35, 37, 187], anti-icing[45, 188, 189, 190, 191, 192], reduced drag[193, 194, 195, 196] and enhanced phase-change heat transfer[197, 198, 199, 200, 201, 202, 203].

Two primary criteria must be met to ensure stable SLIPS: 1) The surface must have nano/micro-roughness which can hold the lubricant in place by capillary action, and 2) The substrate must have a greater chemical affinity for the lubricant than the working fluid it is repelling[35, 37]. The substrate can either be an impermeable material that is roughened and/or porous[75, 180, 204, 205, 206, 207, 208, 209, 210, 211, 212] or an absorbent polymer where the "nano-roughness" is the molecular matrix itself[176, 182, 187, 213, 214, 215, 216, 217, 218, 219].

Absorbent polymer coatings are an increasingly popular choice for SLIPS because of their compatibility with a wide variety of industrial metals and practical materials[187]. However, so far the polymer choices have been limited to expensive silicone or fluorine-based polymers[176, 182, 210, 213, 214] and/or involve the complex assembly of multi-layer polymer coatings on functionalized surfaces[217, 218, 219]. There is also a class of cross-linked elastomers called organogels or fluorogels which can be swollen with oil[187, 215, 220, 221], which are practically limited by similar issues of cost and complexity. Organogels have also been cured with oil inside, but this approach requires a change in environment (heat or pressure) to release the oil toward the surface [222].

Hydrocarbon-based polymers such as polyethylene (PE) and polypropylene (PP) are the most common plastics in the world in terms of production volume and are widely used for packaging applications due to their cost effectiveness and chemical resistance[223]. Despite the obvious attraction of converting extruded film packaging directly into SLIPS to maximize product drainage, to date this has not been considered because hydrocarbon-based films like PE are generally considered resistant to impregnation by wicking oils. Indeed, PE has even been used as a backing material for SLIPS specifically because of its superb chemical and moisture resistance [224]. While oil has been impregnated within microporous PP membranes, the oil was impregnating the micropores not the PP itself[210].

Long before the invention of SLIPS, there has been a technique of mixing a molten solution of ultra-high molecular weight (UHMW) polyethylene with an oil, typically for use as roller bearings [225, 226]. However, this is fundamentally different from SLIPS in two important ways. First, this approach requires the oil to be mixed with the molten polymer prior to curing, whereas for SLIPS the lubricant is simply wicked into an already-made solid substrate. Second, the oil cured within the polymer using the molten method cannot freely

migrate to the outer surface unless subjected to a strong force, such as the centrifugal force experienced by bearings. This is in sharp contrast to the impregnated liquid of SLIPS, which can passively wick to the outer surface to replenish any lubricant that has been depleted over time. Similarly, Golovin et al. has reported plasticizing hydrocarbon-based polymers with oils, in order to tune the mechanical properties of the polymer to minimize ice adhesion [41, 227]. In short, to date there has not been any demonstration of using hydrocarbon-based polymers as SLIPS.

Here, we present the surprising finding that several extruded hydrocarbon-based polymer films such as polyethylene can be directly and stably impregnated with lubricating oil to convert them into SLIPS. Impregnation was enabled by utilizing low density polymers, such as ultra-low density polyethylene (ULDPE), in conjunction with vegetable oils that exhibit excellent chemical compatibility with the polymer film. While the wicking rate of the oil into hydrocarbon-based polymers was indeed extremely slow, we demonstrate that this is not problematic in the context of impregnating micrometric film layers. Finally, we show that our hydrocarbon-based SLIPS can durably repel both Newtonian fluids (water) and non-Newtonian fluids (ketchup and yogurt), making them ideal for a variety of packaging applications.

6.2 Materials and Methods

Infusion Method

Multilayer extruded commercial-grade polymer films (thickness $\approx 0.1\,\mathrm{mm}$) obtained from Bemis Company, Inc. (Neenah, WI) were used as substrates for infusion. Most commonly, the top and bottom layers of the films were comprised of ULDPE (thickness $\approx 10\,\mu\mathrm{m}$), while the intermediate layers were a proprietary combination of highly impermeable polymers. For oil impregnation within the ULDPE polymer matrix, cottonseed oil (Sigma Aldrich) was used. Impregnation with oil was achieved using a motorized drawdown coater (ChemInstruments, EC-100) with the smallest size coating rod (size 0). First, 100–200 μL of cottonseed oil ($\rho = 925\,\mathrm{kg/m^3}$) was pipetted on the leading edge of the polymer film. Second, the motorized rod spread the oil uniformly across the top face of the film. After waiting for a few seconds to allow for the oil to impregnate the ULDPE, any excess oil atop the film was firmly wiped away with absorbent wipes (Kim wipes). For the control case where the oil did not impregnate the ULDPE, the same process was repeated but with 10 cSt silicone oil (Sigma Aldirch) instead of cottonseed oil. Other polymer films that were also used included medium density polyethylene (MDPE), cyclic olefin copolymer (COC), polypropylene (PP), or polyethylene terapthalate (PET) as the top layer.

Details of Polymer Samples

The polymer samples used in this study were all manufactured from commercially available resins. The name, molecular weight, density, molecular weight, and degree of crystallinity of each polymer sample is shown in Table 6.1. The molecular weight of the ULDPE resin was not available, but its Melt Flow Index (MFI) is less than 0.5 g/10 min which is indicative of a very high molecular weight. Direct measurement of molecular weight distributions by gel permeation chromatography (GPC) or dilute solution viscometry is more involved and often does not correctly predict the molecular weight distribution especially for long chain branched polymers like our ULDPE sample which is an ethylene-butene copolymer. The Cyclic olefin copolymer (COC) used in this study is a cycloolefin copolymer of ethylene and norbornene (about 36 mol%). The degree of crystallinity for COC is an estimation based on the fact that this specific grade of resin is made of fully amorphous ethylene-norbornene backbone with a few percent LLDPE fraction which introduces the 2% crystallinity.

Table 6.1: Details of all the polymer samples used in the study. Product name, density, molecular weight, and approximate degree of crystallinity for different polymer samples. The blank values correspond to unknown information that is proprietary.

Polymer name	**Resin name**	**Density (g/cc)**	**M_w(g/mol)**	**Degree of crystallinity**
ULDPE	Engage®HM 7387	0.87	Very High	16%
PP	SA861	0.90	280,000	46%
COC	Topas®8007F	1.01	104,000	$\sim 2\%$
MDPE	NA272130X02	0.93	90,000	47%
PET	S2008	1.27	80000	-

Surface Characterization

The surface roughness for the dry ULDPE films was characterized by atomic force microscopy (AFM) (Multimode) analysis using a contact mode with a silicone nitride cantilever (Bruker). The scanning area was 20 μm X 20 μm. The roughness values did not change appreciably when the scan range was reduced to 5 μm and 10 μm. Two different methods were used to characterize the contact angle hysteresis of liquid droplets on dry or infused polymer samples. For water droplets, the shrink/swell method was employed using a contact angle goniometer (ramé-hart Model 590). A small (5 μL) droplet was deposited on the test surface and its volume was increased/decreased in 0.2 μL increments until the advancing/receding contact angle was obtained and measured by interfacing the camera with an automated software (DROPimage Advanced, ramé-hart). For highly viscous fluids like ketchup and yogurt, a 1.3 or 1.5 g dollop of the product was placed on the desired film, and the tilt angle was increased in 1° increments until finding the critical sliding angle where the dollop of ketchup/yogurt

could slide down the surface. The sliding angle relates the gravitational and hysteresis forces, and is therefore correlated with contact angle hysteresis.

Laser Scanning Confocal Microscopy

The oil impregnation and oil layer thickness was tested with the help of a laser scanning confocal microscope (Zeiss LSM 880). For better visualization, the cottonseed oil was dyed with a lipid soluble fluorescent dye (Bodipy FL C_5, Thermo Fisher Scientific) at a concentration of 0.1 mg/mL. The oily side of the infused ULDPE film was fixed to a glass cover slip of 150 μm thickness. A 40× objective was used which corresponds to a 1 μm vertical resolution. The green noise around the bright green fluorescent oil layer is probably due to improper dye concentration within the oil. But even without the dye, the oil layer thickness found by the reflection mode came out to be similar in thickness which confirms that the dye concentration did not affect the oil thickness measurement.

Wicking Test

To visualize oil wicking inside of ULDPE, 100 μL volume of oil (cottonseed oil or silicone oil) was mixed with 1.0% (w/v) petroleum fluorescent dye (Risk Reactor, DFSB-K175 UV Orange) using a vortex mixer. The fluorescent oil was placed in a $(50\,\text{mm})^3$ open-top borosilicate cell (Spectrocell Inc.) to avoid optical distortion and illuminated with a UV light source (Risk Reactor, 52021(SLR-004-OL)). A vertically-oriented film of ULDPE was clamped over the fluorescent oil bath and the bath was raised on a z-stage until the bottom of the film was submerged. Images of the wicking front were taken in 5 min intervals for 9 hr by a Nikon D5300 camera. The displacement of the wicking front over time was measured using the Tracker software program. For both cottonseed oil and silicone oil, three wicking trials were performed.

Pouch Fabrication

Two different types of pouch geometries were used in this study: three-walled pouches (two 18 cm × 12 cm side walls and a 6 cm × 12 cm base) and five-walled pouches (four 18 cm × 12 cm side walls and a 6 cm × 12 cm base). The pouches were constructed by bonding dry or infused multilayer ULDPE films together using a tabletop plastic film impulse sealer. The three-walled pouches were used for the long-term durability study (see Section 4.5) while the five-walled pouches were used to study the three regimes of pouch drainage (Section 2.4).

The drainage performance of the three-walled and five-walled pouches were qualitatively similar; the five-walled pouches were made in an attempt to minimize confining edge effects while studying the dynamics of drainage.

Durability Tests

The durability of oil-impregnated ULDPE films was assessed using two different types of tests.

Pressing test: Four multilayer films, all 6 cm × 6 cm in area, were stacked on top of each other. The top side of each film was comprised of an oil-impregnated ULDPE film layer, while the bottom side was a dry ULDPE layer. A 5 kg weight was placed on top of the stack for at least 24 hr, such that the impregnated ULDPE layers were in intimate contact with the opposing dry ULDPE layers. After removing the films from the stack, the contact angle hysteresis of water droplets on the impregnated ULDPE layers was measured using the shrink/swell method.

Submersion test: Three-walled pouches comprised of oil-impregnated ULDPE multilayer films were filled with ketchup and stored at room temperature for nearly two months (53 days). The drainage rate was then measured and compared to that of impregnated pouches that were drained immediately upon being filled with ketchup. There was no appreciable difference between the two, indicating the excellent stability of the cottonseed oil impregnated within the ULDPE layer even under prolonged submersion in the ketchup (See Figure D.1 in Appendix D)

6.3 Results

6.3.1 Oil-Impregnation of ULDPE Films

To demonstrate how practical extruded films can be easily converted into SLIPS, we used a drawdown coater to impregnate oil into the top layer of a multilayer commercial-grade polymer film (Fig. 6.1). As shown in Figure 6.1, the rod in the drawdown coater moved over a dry film at a constant velocity with a trace amount of oil and ensured that a smooth oil layer is formed over the film. For this initial proof-of-concept, the top layer of the film was approximately 10 μm thick and comprised of ultra low-density polyethylene (ULDPE), while the tie layers were highly impermeable to the oil in order to isolate the SLIPS to within

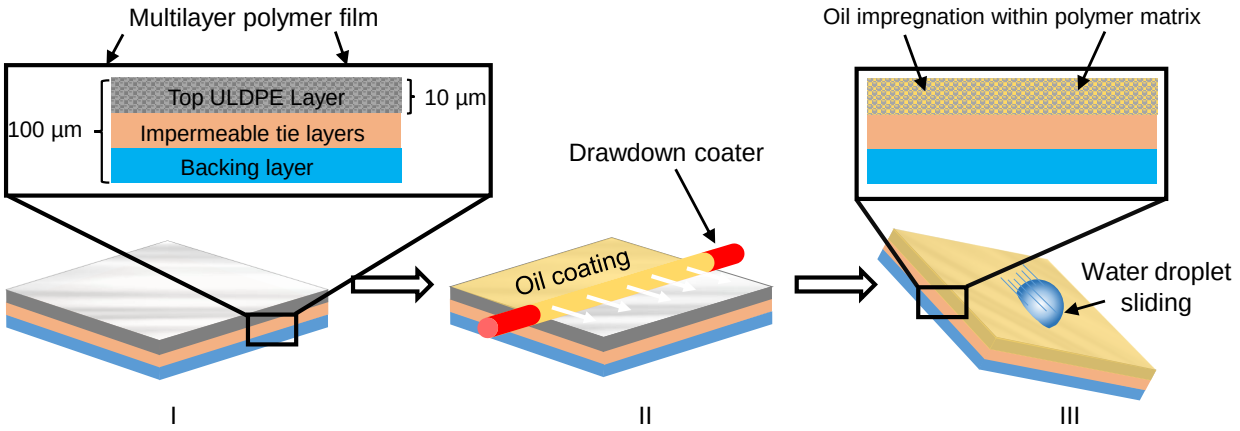

Figure 6.1: Schematic of how carbon-based polymer films such as ULDPE can be easily modified to become slippery oil-impregnated surfaces. I) A multilayer extruded polymer film is used as substrate, with ULDPE as the top layer. II) A small, controlled volume of oil is spread across the face of the ULDPE layer using a drawdown coater. III) Chemically compatible oils easily impregnate within the thin ULDPE layer to create a durable, slippery surface.

the top layer (see Experimental Section for more information). After rod-coating the top ULDPE layer of the film with a small amount of cottonseed oil, it was observed that the surface became extra slippery to deposited water droplets (i.e. low CAH) as quantified in the proceeding section.

Of course, it is possible that the slippery properties of the film were merely due to a bulk layer of oil resting atop the surface, as opposed to the oil actually impregnating within the ULDPE. This distinction is not trivial: oil in the former case is easily sheared off due to gravity or other forces, while oil for the latter case is locked within the interstitial spaces between the polymer molecules for excellent stability[38, 193, 228]. Using gravimetric measurements[206, 207], the total oil amount spread across the sample after rod-coating was found to be about $1.9\,\mathrm{g/m^2}$. Absorbent wipes were then used to firmly remove the excess oil resting atop the film. The $1.2\,\mathrm{g/m^2}$ of oil removed by the wipes corresponded to an initial excess oil layer atop the film whose thickness was approximately $1\,\mu\mathrm{m}$. Even after removing the excess, $0.7\,\mathrm{g/m^2}$ of oil remained impregnated somewhere in the ULDPE layer. The rod-coated films remained equivalently slippery even after the excess oil was removed, which further indicates that the oil is indeed impregnating the ULDPE. The similar contact angle hysteresis of droplets on impregnated films with/without an excess layer agrees with a recent study by Muschi et al., who showed that the excess layer does not tend to affect the slippery properties of SLIPS[229].

After removing the excess oil, where is the remaining oil residing? One possibility is that the exterior of the ULDPE layer exhibits a surface roughness, capable of impregnating the

oil. Atomic force microscopy (AFM) revealed a root mean square roughness of only 21.4 nm (Fig. 6.2a). In contrast, laser scanning confocal microscopy revealed that the oil was able to impregnate to a depth of 1.3 μm within the ULDPE layer (Fig. 6.2b). These findings therefore confirm that the oil is impregnated within the bulk of the ULDPE layer, as opposed to merely residing within the exterior surface roughness.

To be absolutely certain that oil impregnation is occurring, the rate of oil wicking across the ULDPE was characterized. The film was oriented vertically and its bottom end was submerged into an oil reservoir (Fig. 6.2c). This setup ensures that the propagation of oil up the film is solely due to impregnation (i.e. wicking) and cannot be caused by gravitational spreading[230, 231, 232]. A small amount of fluorescent dye was added to the oil reservoir to assist the imaging of the advancing oil front up the ULDPE film.

Figure 6.2d graphs the displacement of the oil front over time. When using cottonseed oil as the working fluid, the oil displacement followed the well-known Washburn equation that balances capillary action against viscous dissipation[233]:

$$l(t) = \sqrt{\frac{\gamma_o r t}{2\mu_o}}, \tag{6.1}$$

where γ_o =0.03 N/m and μ_o =0.07 kg/m-s are the surface tension and viscosity of the cottonseed oil, respectively, and r is the effective "pore" radius of the interstitial gaps between ULDPE molecules. The excellent fit of the data to the $l \sim t^{1/2}$ power-law slope of Equation (6.1) confirms that the oil is able to impregnate inside of the molecular spaces of ULDPE. This finding is notable given that polyolefins like PE are well-known for their chemical/moisture resistance and never before used for SLIPS. Furthermore, the effective pore radius that obtains a best fit of Equation (6.1) to the data, $r \approx 0.175$ nm, is a good match to reports measuring the interstitial spacing between PE molecules to be about 0.2 nm[234, 235]. This extremely small value of r results in extremely slow wicking rates, for example it takes roughly 10 hr for the cottonseed oil to impregnate a mere 1 mm into the ULDPE! However, we emphasize that this does not matter in the context of infusing ultra-thin extruded films. For example, if the oil is spread uniformly across the top face of the film, it will only take about $t \approx 0.05$ s to completely impregnate the 1.3 μm thickness within the ULDPE layer. While there has been some debate on the applicability of the Washburn equation at the nanoscale [236, 237], recently it has been shown that the Washburn equation holds even when the pore radius is only 10 times the size of a liquid molecule [238]. This previous finding, along with the excellent fit of our wicking dynamics to the 1/2 power law, validate our use of the classical Washburn equation.

The wicking of cottonseed oil within the ULDPE film confirms that the nanometric intermolecular spaces can hold the oil layer by capillary action, which satisfies the first criteria required for stable SLIPS. This first criteria is further validated by side-view imaging of a 10 μL

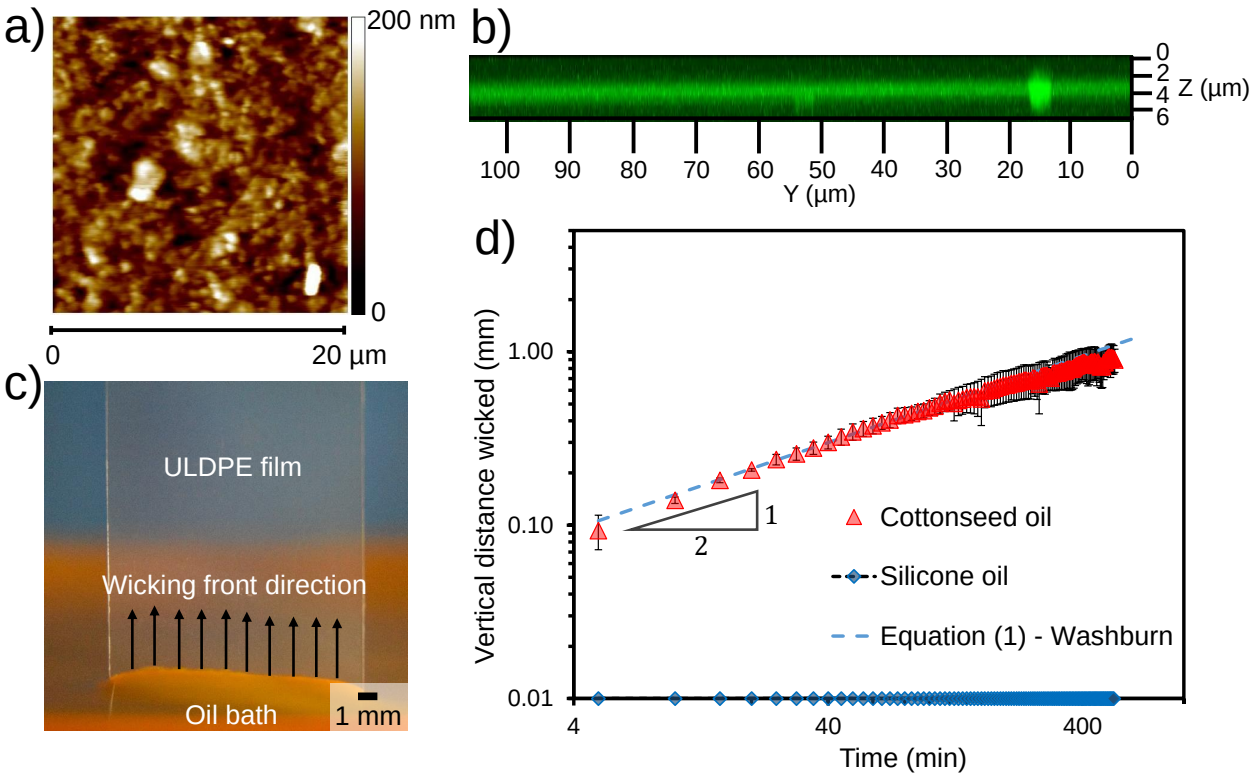

Figure 6.2: Surface characterization. a) Topographical map of the surface roughness of a dry ULDPE film. Atomic force microscopy was used over a scan area of 20 μm X 20 μm. b) Image stack of an oil-impregnated ULDPE film, as obtained by laser scanning confocal microscopy. The bright green band represents fluorescently dyed cottonseed oil, which impregnated the ULDPE film to a depth of about 1.3 μm. Excess oil atop the film was removed prior to imaging. c) Photograph of the wicking setup, where a vertical ULDPE film is partially submerged in a fluorescent-dyed bath of cottonseed oil. For oil choices where wicking is possible, an advancing front progresses up the film by capillary action (black arrows). d) Plot of the vertical displacement of the oil over a time span of 9 hr. The advancing front of the cottonseed oil followed Washburn's law (red triangles), while no wicking was observed when using silicone oil (blue diamonds). For this graph and all future graphs, each data point represents an average from three trials, while the error bars correspond to plus or minus a standard deviation.

cottonseed oil droplet on ULDPE, which revealed a static contact angle of $\theta_o \approx 43° < 90°$. Recall that the second criteria dictates the impregnated oil layer should not be displaced by a deposited test liquid. As shown by Lafuma and Quéré, the oil should not get displaced from a thermodynamic standpoint when the following inequality is satisfied [35]:

$$\gamma_o cos\theta_o - \gamma_w cos\theta_w - \gamma_{o/w} > 0, \tag{6.2}$$

where subscripts 'o' and 'w' denote the oil and water phases, respectively. Using the pendant droplet method on a goniometer, the value of the oil-water surface tension was measured to be $\gamma_{o/w} = 0.021\,\mathrm{N/m}$. After measuring $\theta_w \approx 97^\circ$ on ULDPE, the left-hand side of Equation (6.2) becomes approximately 10 mN/m which satisfies the stability criteria.

As both capillary wicking and swelling in polymers are diffusion-controlled processes which follows the familiar 1/2 power law, it is possible that the oil imbibition in the ULDPE film is actually a swelling mechanism which will eventually degrade the polymer. The Plastics Design Library (PDL) is a resource that exhaustively details the interactions of different polymer grades with a variety of mediums [239]. The ULDPE films used in this study are essentially linear low density polyethylenes (LLDPE). The PDL assigns a rating of 9 for the specific combination of LLDPE in a cottonseed oil medium which corresponds to a weight change of less than 0.5% for the LLDPE. So we can safely assume negligible swelling in the ULDPE films used here, as the mass of cottonseed oil used to infuse the ULDPE was typically only about $2\,\mathrm{g/m^2}$. In general, such limited swelling in polymers follows first-order diffusion kinetics (i.e. $\sim t^1$ dependence) in contrast to the second-order diffusion kinetics ($\sim t^{1/2}$) during severe swelling[240]. But our wicking test revealed that the oil front and consequently the mass uptake amount is following second-order kinetics without any appreciable swelling of the ULDPE film. Thus, the primary mechanism of the oil impregnation within the polymer is the capillary imbibition of the oil inside the amorphous regions of the polymer, rather than swelling of the polymer.

In addition to cottonseed oil, we also found that canola oil and soybean oil successfully impregnated the ULDPE films as evidenced by the reduced CAH of deposited water droplets (Figure D.2). This suggests that vegetable oils in general are chemically compatible with the ULDPE films. To illustrate the importance of chemical compatibility, we repeated the wicking test with silicone oil which is a synthetic oil. Even after 9 hr of the ULDPE film being in contact with the oil reservoir, there was absolutely no wicking front observed (Fig. 6.2d). This chemical compatibility between different oils and ULDPE can be explained by means of their molecular structures. Permeation of liquids in polymers can be affected by the permeant's molecular weight and polarity, as well as the polymer's free volume. From the chemical composition of cottonseed oil[241] we found out the average molecular weight of cottonseed oil is about 870 g/mol which is similar to the molecular weight of 10 cSt silicone oil[242]. Thus, the primary factor that affects permeation into ULDPE is most likely their polarity. A polar permeant will in general have a higher affinity for permeating in a polar polymer than in a non-polar polymer and vice versa[243]. Natural oils and fats are composed of complex mixtures of non-polar triglycerides, whereas silicone oil (polydimethylsiloxane) has a polar characteristic due to the presence of polar $Si - O$ bonds[244] (Figure D.3). This explains why non-polar vegetable oils wick inside non-polar ULDPE while polar silicone oils do not.

In general, we note that existing reports of SLIPS utilize polymers that are already well-known to be absorbent, while avoiding materials like ULDPE that are assumed to be impermeable. As revealed by our surprising test results with ULDPE, we suggest that wicking

tests should be conducted with a wide variety of material and oil combinations. This could not only reveal an expanding palette of material choices that are suitable for SLIPS, but even reveal which oils are able to impregnate a given material.

6.3.2 Wetting Properties of Oil-Impregnated Films

What is the minimum amount of impregnated oil required to preserve the maximal slipperiness of the ULDPE? To find the lower limit, a set of experiments was performed with various mixtures of oil and isopropyl alcohol. The isopropyl alcohol rapidly evaporated after coating the ULDPE film, resulting in oil uptake amounts of any desired value based on the mixture ratio. We used ketchup "droplets" instead of water droplets to test the slipperiness of surfaces, as ketchup exhibits larger values of hysteresis making it easier to detect variations in surface friction with changing oil amounts. Ketchup is too viscous for the shrink-swell method of CAH measurement; instead, a motorized tilt base was used to find a critical sliding angle (SA) for a fixed mass of ketchup (1.3 g). Figure 6.3 shows the results, where now the SA (and by extension the hysteresis) can clearly be seen to significantly decrease with increasing oil uptake until reaching a minimal value at a critical concentration of about 0.5 g/m^2. Any further increase in oil uptake amount does not significantly affect the SA. This critical uptake amount is in good agreement with the aforementioned gravimetric measurements, which revealed that about 0.7 g/m^2 of oil is able to actually impregnate the ULDPE. These results clearly demonstrate that only an extremely small amount of oil is required to maximize the slipperiness of the impregnated ULDPE films. For the rest of the paper, an oil uptake amount of about 2.3 g/m^2 was used, as this is above the lower limit while also removing the need to add any isopropyl alcohol for our particular drawdown coater.

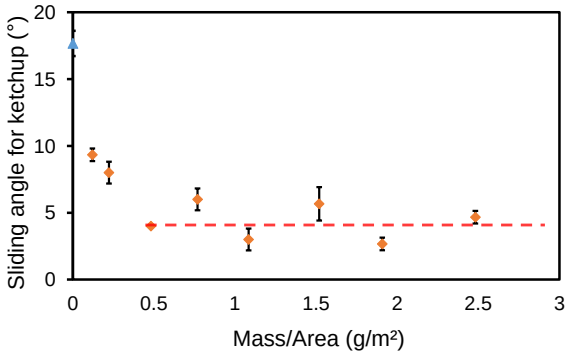

Figure 6.3: Optimum oil amount. The sliding angle for a dollop of ketchup (1.3 g) as a function of the oil amount applied to a ULDPE film. The dashed red line indicates that the tilt angle becomes constant at about 4° beyond an oil uptake of 0.5 g/m^2. For comparison, the sliding angle on a dry ULDPE film is indicated by the blue triangle.

Another germane question: besides ULDPE, can any other hydrocarbon-based polymer

films be impregnated with oil? To answer this question, the slipperiness of various types of commercial-grade extruded films were characterized, comparing dry films to equivalent films impregnated with cottonseed oil. For dry polymer films, the hysteresis of water droplets is always above CAH $> 10°$ (Fig. 6.4a). Upon oil impregnation, four of the five films: ULDPE, polypropylene (PP), cyclic olefin copolymer (COC), and medium-density polyethylene (MDPE) exhibited a significant decrease in hysteresis to CAH $< 5°$. This reveals that beyond just ULDPE, many types of hydrocarbon-based polymer films are suitable for creating SLIPS. Similar results were obtained with 1.5 g dollops of ketchup, where the sliding angle was dramatically reduced for the same four polymer films (Figure 6.4b). However, only the oil-impregnated ULDPE, COC, and MDPE were able to produce sliding angles of SA $< 10°$. The sliding angle of the infused PP was closer to SA $\approx 18°$, although this was still only half the value of the equivalently dry PP (SA $\approx 30°$). We will now return to using ULDPE films for the remainder of this report, but clearly MDPE and COC (and to a lesser extent, PP) are also suitable candidates for SLIPS.

Why do polymers like ULDPE and COC facilitate oil impregnation while PET does not? We suggest this is a result of differing free volumes in the polymers. Free volume corresponds to the amount of amorphous phase or degree of crystallinity in a polymer. Permeation of liquids or gases takes place only in the amorphous phase within the polymer[245] and in general increases with increasing free volume, as shown by Lee[246]. The degree of crystallinity is only 16% for ULDPE and 2% for COC, indicating these films are predominantly amorphous. Apart from the degree of crystallinity, the polarity of the polymer and permeant molecules also affects the penetration of a liquid into a polymer. Due to the presence of oxygen containing functional group, PET has a high level of polarity. Thus, it is much harder for non-polar vegetable oils to permeate into PET than in non-polar ULDPE or COC polymer[243, 247]. It is also possible that PET has a higher degree of crystallinity, but this information was proprietary for this particular resin product.

Using the tilt method, snapshots of sliding water droplets were taken to visually capture the difference in CAH of dry versus oil-impregnated ULDPE (Fig. 6.5a). On dry ULDPE, droplets exhibit CAH $\sim 10°$, such that the droplet shape is obviously tilted toward its advancing contact line. In contrast, the oil-impregnated ULDPE exhibits CAH $\sim 1°$, such that sliding droplets do not have any appreciable shape change. Figure 6.5b illustrates the dramatic reduction in sliding angle for ketchup on the oil-impregnated ULDPE, where a small dollop of ketchup can easily slide at low angles (SA $\approx 5°$) without having to dramatically change its shape. Finally, by holding vertically oriented films against the light, it can be seen that ketchup sliding down an oil-impregnated ULDPE film leaves much less residue on the film compared to dry ULDPE (Fig. 6.5c).

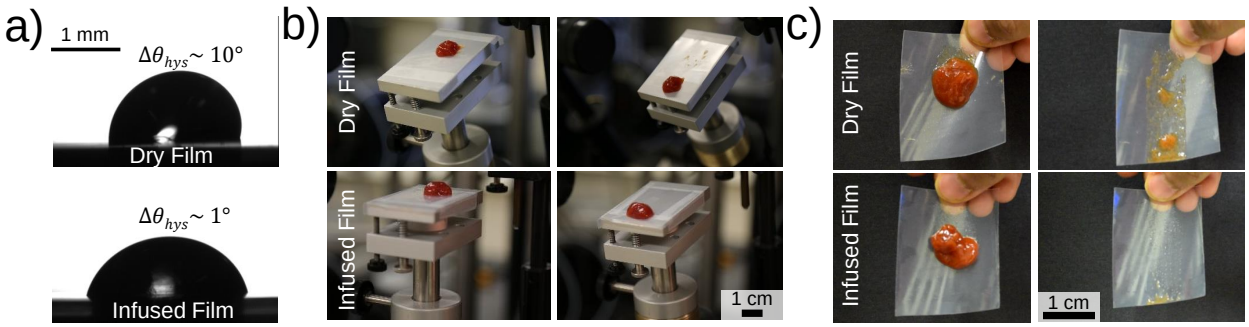

Figure 6.4: Contact angle hysteresis tests. a) The contact angle hysteresis of water droplets on five different polymer films: ultra-low density polyethylene (ULDPE), polypropylene (PP), cyclic olefin copolymer (COC), medium-density polyethylene (MDPE), and polyethylene terephthalate (PET). b) The sliding angle of a 1.5 g dollop of ketchup on the same films. In both charts, blue bars represent the CAH when the polymers were dry and untreated, while the orange bars represent the same polymers but impregnated with cottonseed oil using a drawdown coater.

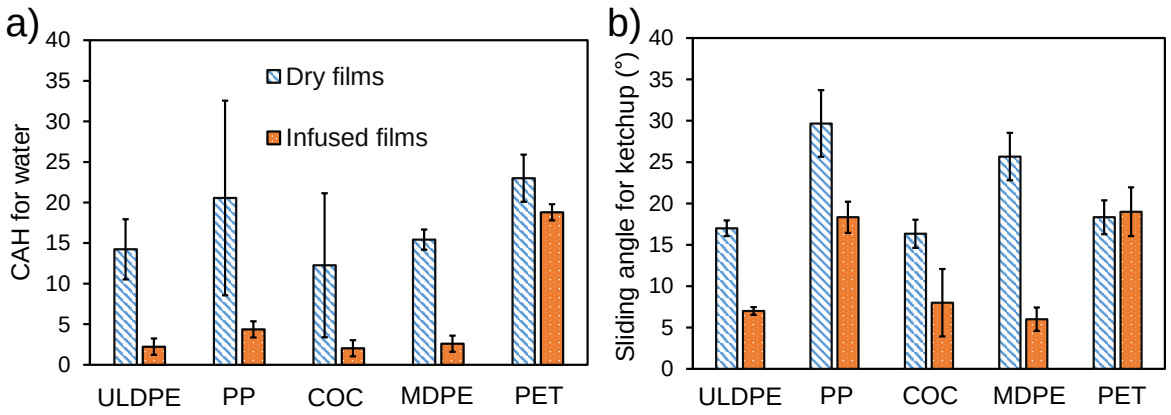

Figure 6.5: Slippery ULDPE film. a) Water droplets sliding down dry ULDPE films have a noticeable asymmetry in shape due to CAH (top), while there is no appreciable difference between the advancing and receding angles of droplets on oil-impregnated ULDPE (bottom). b) The sliding angle of a 1.3 g dollop of ketchup is 23° on dry ULDPE (top images), but only 4° on oil-impregnated ULDPE (bottom). c) On dry films (top images), sliding ketchup leaves behind considerably more residue than on infused films (bottom).

Durability tests

When long sheets of extruded polymer films are manufactured, they are commonly rolled up for storage prior to distribution. In this rolled-up configuration, the top layer of the multi-layer film is firmly pressed against the bottom layer. In packaging applications, only the top (i.e. inside) layer should be oil-impregnated, so it is important to know whether there will be an undesirable transfer of oil from the top layer to the bottom layer during

storage. This was tested by stacking four multi-layer extruded films on top of each other, where both the top layer and bottom layer of each film were ULDPE but only the top layers were oil-impregnated. A weight of 5 kg was placed on top of the stack, such that the three bottom films all had an oil-infused ULDPE layer that was firmly pressed against the dry ULDPE of the next layer.

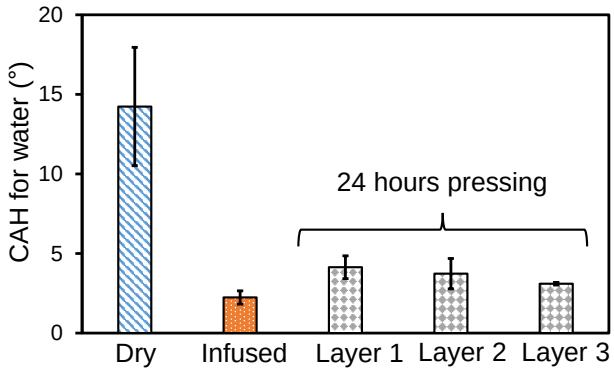

Figure 6.6: Stability of oil impregnation process. The physical stability of the oil-impregnated ULDPE was demonstrated by pressing 3 layers of oil-infused ULDPE against dry layers of ULDPE with a 5 kg weight. Even after 24 hr of pressing, the CAH of the oil-impregnated ULDPE layers remained extremely low ($< 5°$), indicative of stable SLIPS.

After 24 hr of pressing the films together, the weight was removed and the CAH of water droplets was measured on the top face of each of the three films. Figure D.1 shows that after 24 hr of pressing, the hysteresis of the water increased only by 1–2°, remaining under CAH$< 5°$ as desired for SLIPS. Most notably, this is still an order of magnitude reduction in CAH compared to the dye ULDPE films. This indicates that only a very small amount of oil drained from the top layer during pressing against the bottom layer, with the large majority of the oil remained stably locked within the top layer.

6.3.3 Drainage from Oil-Impregnated Pouches

To test the effects of oil-impregnation on product drainage, we created three-dimensional open pouches (dimension: 18 cm × 12 cm × 6 cm) by bonding together five films with an impulse sealer (see Experimental Section 4.4). Equivalent pouches were made from dry or oil-impregnated ULDPE films, filled with 170 g of ketchup, and then poured at a 45° angle using the goniometer's motorized tilt base. For the first 10 s of pouring, the drainage rates of the ketchup were similar for both the dry and oil-impregnated ULDPE. Beyond 10 s, however, the oil-impregnated pouch drained ketchup at a significantly faster rate than the dry pouch and also minimized how much residue was stuck to the films at the end of pouring (Fig. 6.7a). Similar results were obtained with yogurt (Fig. 6.7b).

The enhanced drainage of ketchup from oil-impregnated pouches was preserved even when the ketchup-filled pouch was stored for over 50 days prior to drainage. This long-term durability of our infused pouches indicates that there is negligible chemical interaction between the lubricating oil layer and ketchup over time. Moreover, it has been found that for a constant average flow velocity, the depletion of the lubricating layer is delayed if the the viscosity of the external fluid is much greater than the viscosity of the lubricating oil due to reduced interfacial velocity[248]. Given $\mu_{\text{ketchup}} \gg \mu_{\text{oil}}$ and the short drainage time, we can safely attest that the shear force exerted by the bulk ketchup or any other viscous food product will have negligible effects on the durability of the infusion.

To quantify the drainage rates, the ketchup was poured into a container placed on a digital mass balance to measure how much ketchup was still in the pouch at any given time. The oil-impregnated surface was able to drain almost 90% of the ketchup in about 50 s, which is only 1/6 of the time required for the dry pouch to drain the same amount. By plotting the drainage over time in a logarithmic plot (Fig. 6.7c), we identified three distinct power-law regimes of drainage as illustrated in Figure 8. These power laws can be independently rationalized using scaling analysis, provided that the following assumptions are made: i) Pouch deformation is neglected, such that the ketchup flows out of a rigid rectangular opening of constant width w. The mass remaining in the pouch is then given by $m(t) = \rho L w h$, where ρ is the density of the liquid, $h = h(x,t)$ is the free surface height of the flow where the x-axis runs along the tilted floor, and L is the length of the floor and by extension the flow[249], ii) the primary flow runs across only one wall of the tilted pouch (i.e. the floor). While the flow does partially interact with the side walls of the pouch, this can be neglected without significant error in our discussion.

The initial drainage rate is the same for the dry and oil-impregnated pouches at early time scales ($0\,\text{s} < t < 7\,\text{s}$). This is in agreement with previous works that observed that initial drainage was unaffected by the container shape or fluid properties[250, 251, 252]. This shows gravity is dominant over any surface effects in this brief period . By approximating the non-Newtonian ketchup as a Carreau fluid, its viscosity as a function of shear stress is given by[253, 254]:

$$\mu = \mu_\infty + (\mu_0 - \mu_\infty)\left[1 + \left(\lambda \frac{du}{dy}\right)^2\right]^{\frac{(n-1)}{2}} \tag{6.3}$$

Where, μ_0 is the zero-shear viscosity, μ_∞ is infinite-shear viscosity, λ is the relaxation time, du/dy is the shear rate, and n is the power index whose value is $n < 1$ for shear-thinning fluids like ketchup. From Eq. 6.3, a shear-thinning non-Newtonian fluid behaves as a Newtonian fluid for small or large shear rates, while behaving as a shear-thinning fluid for intermediate shear rates. The high flow rate, and consequently high shear rate, of the initial regime of pouring therefore causes the ketchup to behave as a Newtonian fluid of constant viscosity $\mu \to \mu_\infty$. The volumetric flow rate in this regime can be modeled as a simple gravity-driven

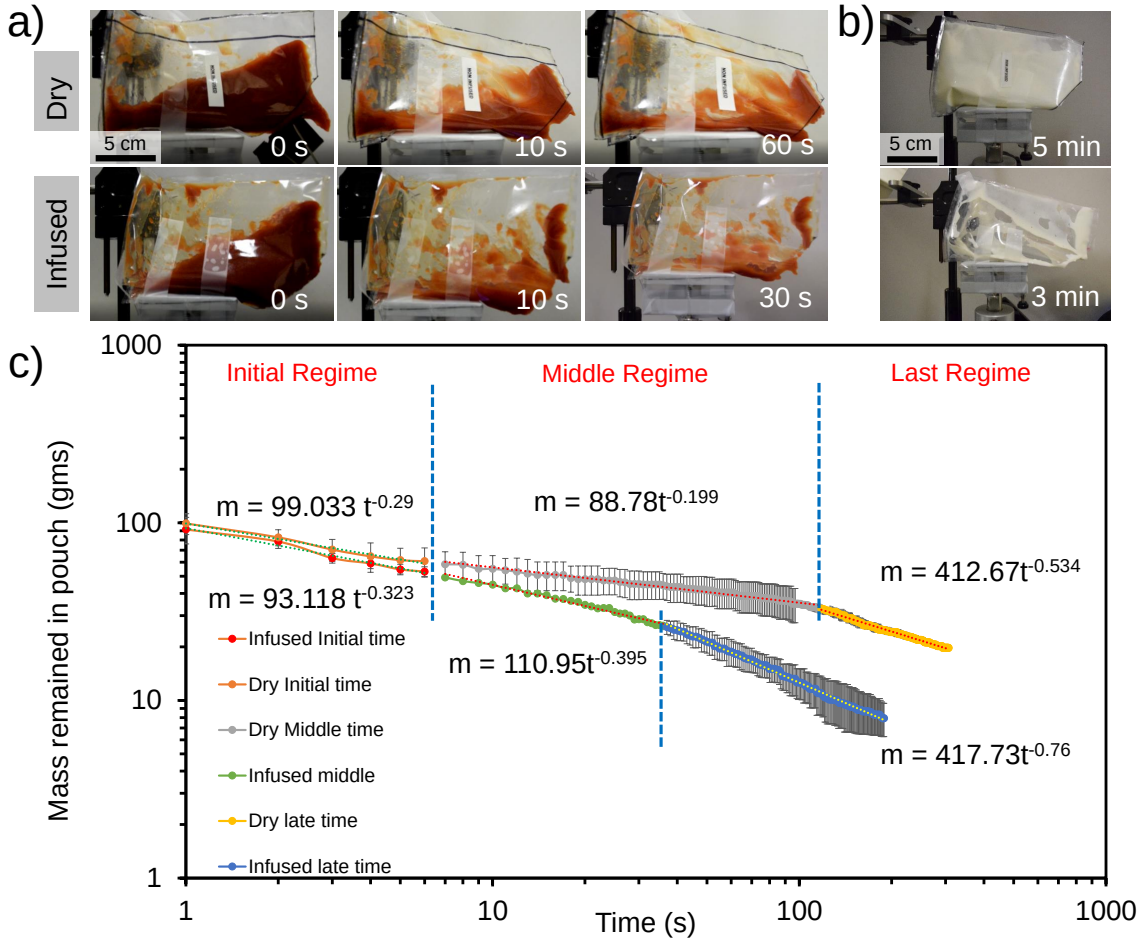

Figure 6.7: Dry *vs.* oil-impregnated ULDPE film. a) Time-lapse of ketchup draining from dry (top) and oil-impregnated (bottom) ULDPE pouches using a tilt angle of $\alpha = 45°$ (camera is also tilted). After 30 s of drainage, a large amount of ketchup is still sticking to the walls of the dry pouch, while the infused pouch is almost completely cleaned out. b) For yogurt drainage, even after 5 min of drainage there is much more yogurt trapped in a dry ULDPE pouch (top) compared to an oil-impregnated pouch (bottom) after only 3 min. c) Logarithmic plot of the mass remaining in the pouch versus time. Vertical dashed lines demarcate three different power-law regimes. For the second and third regimes, the power-law slope was more pronounced for the oil-impregnated pouch.

Poiseuille flow of uniform thickness $h = h(t)$ down an inclined plane (Figure 6.8b):

$$Q \sim \frac{\rho g \sin(\alpha) h^3 w}{\mu_\infty}, \tag{6.4}$$

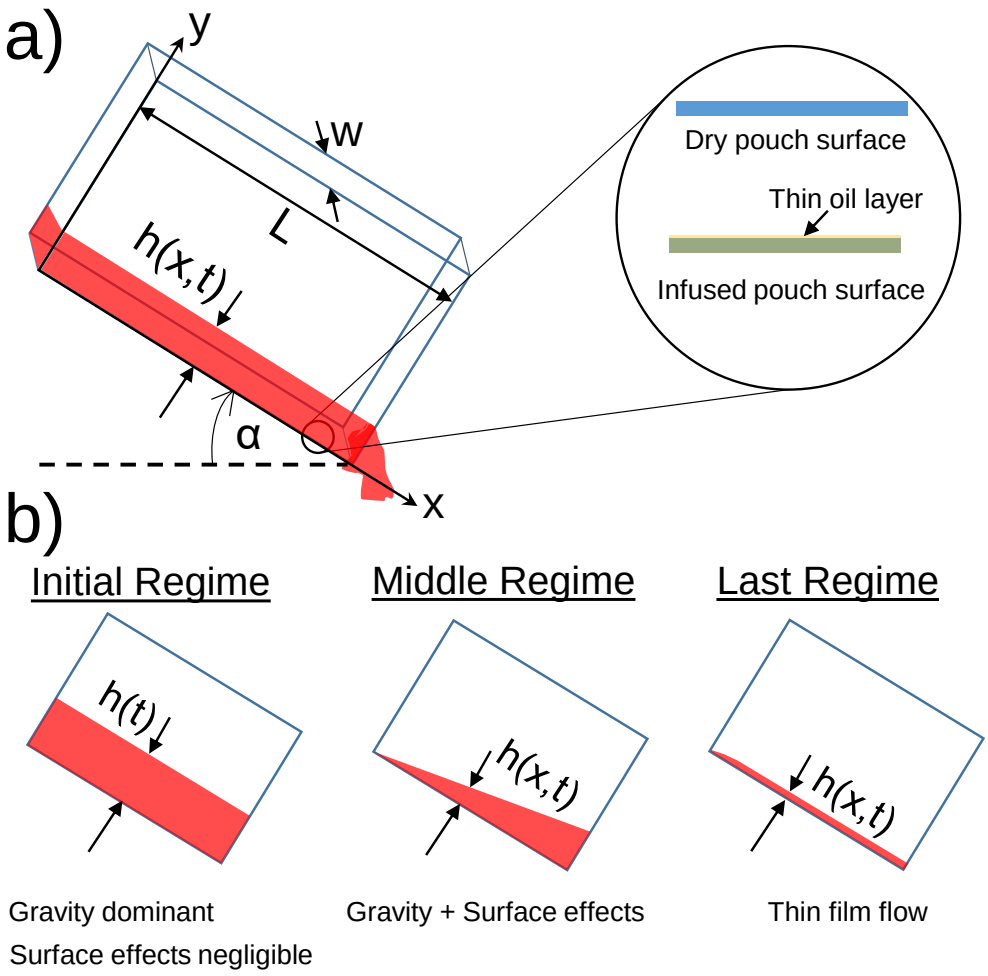

Figure 6.8: Drainage physics. a) Schematic of the pouch drainage: w and L denote the width and length of the rectangular pouch respectively, h is the height of ketchup which can be function of position and time, and α is the inclination angle. The inset depicts the difference between dry and oil-impregnated polymer films comprising the pouch. b) Schematic of the three drainage regimes, where the primary difference is the height profile.

where α is the tilt angle of the pouch. Using $\dot{m} = \rho Q \sim m_d/t$, where m_d is the mass drained after some time t, it follows that:

$$\frac{m_d}{t} \sim \frac{\rho^2 g \sin(\alpha) h^3 w}{\mu_\infty}, \tag{6.5}$$

Ali et al. has shown that at the end of the initial regime of drainage, the ratio of the mass remaining within the container to the initial mass remains fairly constant irrespective of

container shape or fluid properties[252]. This mandates a constant value of m_d/t for a time t corresponding to the end of this initial drainage regime, as the initial mass in the pouch was the same for both dry and infused pouches. Thus, from Equation (6.5), the scaling law $h \sim t^{-1/3}$ is obtained. For a container of constant width, this also means that the ketchup mass remaining in the pouch scales as $m \sim t^{-1/3}$, in excellent agreement with our experimental results for both dry and infused pouches.

In the second regime, corresponding to $10\,\mathrm{s} < t < 120\,\mathrm{s}$ for the dry pouch and $10\,\mathrm{s} < t < 40\,\mathrm{s}$ for the infused pouch, surface effects become important and the drainage rate from infused pouches ($m \sim t^{-0.4}$) greatly exceeds that of the dry ones ($m \sim t^{-0.2}$). At the moderate flow rates of this regime, the ketchup behaves like a shear-thinning fluid. The shear-thinning viscosity can be simply approximated as $\mu = \mu_0 \left(\partial u/\partial y\right)^{n-1}$[253]. Flow in this regime can still be modeled as Poiseuille flow, but now $h = h(x,t)$ is no longer uniform along the incline (Figure 6.8b). Balancing shear stress and gravity:

$$\frac{\partial \tau}{\partial y} = \frac{dP}{dx} = -\rho g \sin\alpha, \tag{6.6}$$

where $\tau = \mu_0 (\partial u/\partial y)^n$ is the shear stress acting on the fluid. We can integrate Equation (6.6) using the zero shear stress boundary condition at the free surface ($\tau|_{y=h} = 0$)[255]:

$$\tau = \mu_0 \left(\partial u/\partial y\right)^n = \rho g \sin\alpha (h - y). \tag{6.7}$$

Integrating again using the no-slip boundary condition: $u(x,0,t) = 0$, Equation (6.7) can be integrated to obtain:

$$u(y) = \left[\frac{(\rho g \sin\alpha)}{\mu_0}\right]^{\frac{1}{n}} \frac{n}{n+1} \left[h^{\frac{n+1}{n}} - (h-y)^{\frac{n+1}{n}}\right]. \tag{6.8}$$

The average flow rate per unit width down the incline can be found by integrating $Q = \int_0^h u(y)dy$, which yields:

$$Q \sim C h^{2n+1/n}, \tag{6.9}$$

where the ρ, α and n terms are collected as a constant C. By conservation of mass, $\partial Q/\partial x = -\partial h/\partial t$. The power index for ketchup is known to be approximately $n = 0.25$[256], such

that the free surface equation can be expressed as:

$$\frac{\partial(Ch^6)}{\partial x} = \frac{\partial h}{\partial t}, \tag{6.10}$$

From the chain rule, Eq. 6.10 becomes:

$$Dh^5 \frac{\partial h}{\partial x} = \frac{\partial h}{\partial t}, \tag{6.11}$$

where D is a re-defined constant. Finally, this yields the scaling law $h \sim m \sim (x/t)^{1/5}$, which is a perfect match with the measured rate of $m \sim t^{-0.2}$ for the dry pouch during this second regime.

Due to the presence of a thin oil-layer, in the oil-impregnated pouch, ketchup can slip at the infused wall[253, 257], resulting in a slip velocity of[193, 253, 258]:

$$u_s = \frac{\mu}{\beta}\left(\frac{\partial u}{\partial y}\right)_{y=0}, \tag{6.12}$$

where β is the slip coefficient. Integrating Equation (6.6) with the new "slip" boundary condition, the velocity profile becomes[253, 254, 259]:

$$u(y) = \left[\frac{(\rho g \sin\alpha)}{\mu_0}\right]^{\frac{1}{n}} \frac{n}{n+1}\left[h^{\frac{n+1}{n}} - (h-y)^{\frac{n+1}{n}} + u_s\right]. \tag{6.13}$$

Note the extra term on the right-hand side compared to the drainage velocity over dry surfaces (Eq. 6.8), which is the likely cause of the enhanced drainage rate of the oil-impregnated pouch in this second regime ($m \sim t^{-0.4}$).

In the third regime, the ketchup draining from the pouch has diminished to become a thin film (Figure 6.8b). As with the second regime, there is a marked improvement in the measured drainage rate for the oil-impregnated pouches ($m \sim t^{-0.8}$) compared to dry pouches ($m \sim t^{-0.5}$). Given the low flow rates of this third regime, the ketchup can be modeled as a Newtonian fluid with constant zero-shear viscosity μ_0. For dry pouches, the flowing ketchup is akin to the classical thin-film flow of a Newtonian fluid down an inclined surface as shown by Jeffreys nearly a century ago[260]. A simple scaling analysis of the problem has been done by Quéré et al. which considers a balance between viscous resistance to the flow $\mu_0 U/h^2$

(where $U \sim \Delta x/t$ is the average flow velocity) and gravitational force ρg to find the evolution of film thickness h with time[261]:

$$h \sim (\mu_0 \Delta x/\rho g t)^{1/2}. \tag{6.14}$$

This results in a power law for drainage of $m \sim t^{-1/2}$ for the third regime, which again agrees with the experimental results. For the oil-impregnated pouches, the aforementioned slippage at the interface, in addition to the reduced hysteresis of any emerging contact lines, explains the larger drainage rate of $m \sim t^{-0.8}$ for the third regime of drainage. While it is possible that shear exerted by a test liquid flowing over an oil-impregnated surface can drain the oil [209], the enhanced drainage of the ketchup from the infused pouches at this last stage of drainage indicates this is not happening appreciably for our system. This is intuitive given our very small effective pore size and the prior observation that shear-induced drainage is more problematic for larger, micro-scale pores [228].

6.4 Conclusion

We have demonstrated that hydrocarbon-based polymers, such as polyethylene, can be easily impregnated with oils to create slippery packaging materials. While polymers such as polyethylene have long been considered impermeable to oils, we demonstrated that impregnation is possible when: 1) The polymer exhibits low density and degree of crystallinity (ex: ULDPE), 2) The lubricant is a vegetable oil for maximal chemical compatibility, and 3) The polymer layer is sufficiently thin (i.e. micrometric) to wick the oil inside of the molecular matrix by Washburn's Law within a practical time scale ($t \sim 1\,\mathrm{s}$). The process of impregnation is as simple as coating a thin ($10\,\mu\mathrm{m}$) pre-made polymer film with at least $0.5\,\mathrm{g/m^2}$ of oil and does not require any surface functionalization. Once the polymer film is impregnated with oil, it is highly slippery to a variety of test liquids such as water, ketchup, or yogurt. By using commercial-grade multilayer films with impermeable tie layers, the oil can be confined to one face of the film but not the reverse face. The oil-impregnation was quite stable, both to mechanical pressing against dry films and to long-term submersion under ketchup. When assembling the films into pouches, both the drainage rate and total drainage amount were significantly enhanced using the oil-impregnated films. Our recipe for easily imparting slippery and anti-fouling properties to commercial-grade extruded films should be highly useful for the packaging industry, particularly for food-release or pharmaceutical applications. More broadly, we expect that these findings will greatly expand the material palette used for creating slippery liquid-impregnated porous surfaces (SLIPS), as to date the polymer choices were restricted to expensive silicone-based polymers or complex multi-layer polymer assemblies on functionalized surfaces.

Chapter 7

Conclusions and Future Work

"'In the end?' Nothing ends, Adrian. Nothing ever ends."

—Dr. Manhattan, Watchmen

7.1 Conclusions

In conclusion, our objectives outlined in Chapter 3 have been accomplished. First, we found out, quite surprisingly, that the gravity-independent jumping-droplet phenomena is also susceptible to the orientation of the condenser surface. A vertically oriented superhydrophobic surface shows the least surface coverage by the condensing droplets and consequently, the best heat transfer performance. We also did a comparative study of heat transfer performance for all the different surface orientations based on the experimental droplet distribution pattern on the surface. Secondly, we established jumping-droplet condensation as an important agent for short-range dispersal of fungal plant pathogens. The spatial scale of dispersal improves drastically when a gentle wind flow is introduced over the leaf surface. We then shifted our attention to another phase-change induced phenomena where we discussed the jumping frost phenomena through extensive experiments and numerical-analytical modeling. Finally, we design a durable slippery liquid-infused surface from hydrocarbon-based polymer films which showed remarkable repellency to both water droplets and dollops of ketchup.

Although our discussion here spanned across apparently disconnected fields of phase-change phenomena, pathogen dispersal, or hydrocarbon-based polymers, we looked at these problems from the viewpoint of interfacial mechanics. The same surface tension which creates the beautiful pearly beads of water droplets can engender high adhesion strength for ice and

frost on a surface. The same event of condensate jumping from superhydrophobic surfaces can enable higher heat transfer efficiency in man-made condensers but can be detrimental for plants if they also carry spores. Our work focused on these often neglected aspects of wetting (and de-wetting) phenomena and answer questions which are deceptively simple, yet useful for future design or disease mitigation strategies. Often we have used simple scaling analysis in place of detailed mathematical models. This helps in presenting only the essential bare bone physics as well as engaging the readers in the discussion. But our understanding in no way is complete as can be plainly understood by the mere 200 page length of this dissertation. Below I present some future works related to few projects that we described in the earlier chapters. Hopefully, our pedagogical approach to understand these problems will inspire other people to work on them.

7.2 Future Directions

7.2.1 Spore dispersal via Jumping-droplet Condensation

In this work we have established the importance of jumping-droplet condensation as a passive spore dispersal mechanism. We have also provided an easy and effective method of suppressing the effect via the application of any hydrophilic fungicide on the leaves. But this study is still far from comprehensive as several challenges still remain as outlined below:

The case against the use of hydrophilic fungicide: Rendering the wheat leaves hydrophilic might have some undesired side effects, as the wax coating on wheat leaves helps them conserve water in dry conditions [262]. Moreover, rendering the leaves hydrophilic changes the dynamics of raindrops impacting the leaves. For example, Park et al. observed that splashed droplets tended to rebound from unsprayed leaves but stick to leaves treated with fungicide [117]. When splashed droplets contain spores, this increased surface adhesion might therefore enhance disease spread. Thus, although the application of a hydrophilic spray has the clear benefit of inhibiting spore transport via jumping-droplet condensation, future studies could explore whether this has the unintended consequence of enhancing spore transport by rainsplash.

Extending the study to other natural surfaces and spores: Wheat leaves are superhydrophobic in nature, as shown by the quasi-spherical condensing droplets in the inset of Fig. 4C in Chapter 3. More detailed contact angle measurements in previous reports also point towards such superhydrophobicity [24, 117]. The superhydrophobic jumping-droplet effect is enabled by the nanometric surface asperities on the leaf surface (Appendix, Fig. B.2), which

are coated with leaf wax. Coalescence-induced droplet jumping has been observed on both artificial [11, 25, 59, 60] and natural substrates [23, 135, 263] comprised of nanostructures or hierarchical micro/nano-structures [264]. During the initial stages of condensation, nanometric ($\approx 1-10$ nm for water) embryos tend to nucleate within the nano-roughness [25, 60]. How these nanometric embryos grow within the cells surrounded by the nanotextures dictates the condensation-induced adhesion as well as occurrence of droplet jumping. If the embryos grow laterally and fill the texture voids before protruding upwards, highly adhesive Wenzel droplets are formed. On the other hand, the jumping-droplet effect is observed when these nucleating embryos can stably inflate into a Cassie state without flooding the surface textures beneath [59, 60]. Naturally, only the Cassie (or partial Cassie) wetting morphologies show jumping-droplet condensation. Thus, the degree of droplet adhesion to the surface (i.e. Wenzel state *vs.* Cassie state) is the more important indicator of the ability to promote jumping-droplet condensation, as opposed to a simple measurement of a droplet's contact angle [59].

The above general discussion sheds some light into how the wax-coated hierarchical nanostructured geometry in both wheat and lotus leaves [135] gives rise to the superhydrophobicity and jumping-droplet condensation behavior. As a natural extension to this, other plant surfaces with hierarchical features should also exhibit similar condensate jumping behavior. Indeed, Mockenhaupt et al. observed coalescence-induced dislodging of dew droplets on the superhydrophobic leaves of eight different plants [135, 137]. Extensive lists of plant surfaces with varying degrees of hierarchical micro and nano-textures has been compiled by Barthlott et al. [138, 139] which can be useful for future studies looking into the importance of dew formation in fungal pathogen transport in other plants.

Field study: By performing the experiments in Chapter 4 in laboratory conditions, we could avoid a lot of the complexities otherwise associated with natural field conditions. First of all, the wind flow in actual field might not be always parallel to the leaf surface, but can come perpendicularly also. Along with this, the real leaves are not fixed in one place but behave as cantilever beams with the ability to twist and bend. All of these factors will affect the jumping angles for the coalescing dew droplets and the subsequent dispersal. During the time of maximum dew formation in natural conditions, we can place spore trapping papers at the canopy level to collect the depositing spores. We can also put spore collectors at different locations in a canopy which take air samples to understand the spore density during a dew cycle. We can compare these data with similar studies done in the same filed after rain events.

7.2.2 Jumping Frost

While in this work, our main objective was to understand the physics behind the jumping frost phenomenon, we are still a long way from a comprehensive understanding. Moreover,

our final goal of utilizing this event in a novel electrostatic de-icing construct is yet to be achieved. Below we list these in detail:

Inclusion of Bjerrum defects in the theoretical modeling – Latham and Mason's model for charge separation in ice [145], adapted in Chapter 4 to estimate the surface charge density, did not consider the effect of Bjerrum defects. This may seem a curios omission, considering that Bjerrum defects are 10^4–10^6 times more abundant than ionic defects. However, attempts to include Bjerrum defects in our thermal migration model (as well as attempts by others) [169] resulted in a positive charge on the warmer end of the frost. This contradicts clear experimental evidence of the frost splinters exhibiting a negative charge, validated by using charged copper electrodes (Figure C.3 in Appendix) and measured directly by others [147, 148, 149]. We hypothesize that the Bjerrum defects do not appreciably contribute to the charge separation because the preferential top-to-bottom thermal migration of negative L defects is largely cancelled out by the migration of positive D defects from the outer surface of the frost to the interior, as suggested by recent density functional theory simulations (see section 3 of the Appendix) [265]. A recent study [266] has shown that the thermoelectricfication process occurs in two distinct stages: an initial fast stage which is dominated by the Bjerrum defects. In the slow stage, ionic defect motions modify the electric field set up by the Bjerrum defects during the initial fast stage. While this is a much welcome report to shed some light into this field plagued by debates, more such studies are required to fully understand this complex interaction between the two kinds of defects. It would also be interesting to vary the ambient gas phase and/or humidity, which was beyond the scope of this initial study. Higher humidity cause faster frost growth which in turn can affect the charge separation process in the frost layer. The impurities in the ambient gas can also affect the charge on the outer frost layer [143].

Investigating practical applications for the jumping frost phenomenon – We also aim to exploit our findings by maximizing the extent of charge separation in ice and applying an opposing charge to rapidly detach and remove the ice from its substrate. Using such constructs in place of existing de-icing methods, such as defrosting or antifreeze chemicals, would save time, money, and be more environmentally friendly. Potential applications could include de-icing aircraft wings or periodically harvesting ice from the intake of a jet turbine, to prevent large chunks of ice from forming that can break off into the turbine and cause mechanical damage. The basic experimental set up involves using a surface with ultra-low ice adhesion ($\tau_{\text{ice}} \sim 1\,\text{kPa}$) to grow frost and a high voltage DC power supply to be used opposite to the frosted substrate. Initial observations suggested by gradually increasing the opposing voltage, the intensity of the frost 'storm' is increasing. Further experimental trials are required to properly conclude if intensity of frost jumping is directly related to the amount of voltage or charge on the opposing metal plate.

Appendices

Appendix A

Effect of Surface Orientation on Jumping-droplet Condensation

A.1 Finding Wenzel neck radius of impaled droplets:

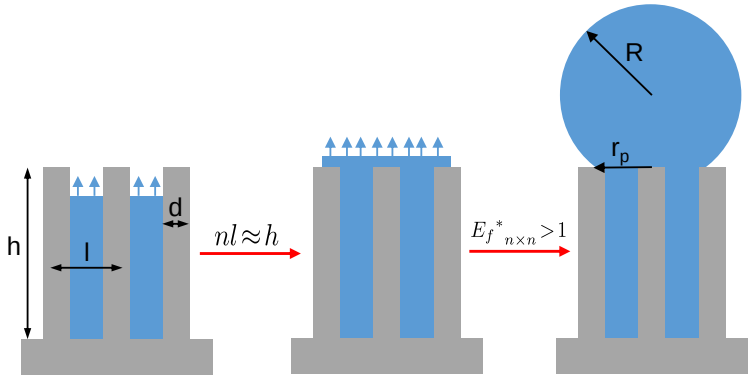

Figure A.1: Schematic of droplet growth from the nano-cavities on the superhydrophobic surface used in the condensation experiments.

For determining the neck radius of an impaled droplet with Wenzel neck, we have followed the three-stage growth model developed by Mulroe et al. [25] Initially a nanometric droplet nucleates within the pillars and grows by direct condensation. In the first stage of the model, we compare the energy required for lateral expansion to adjacent unit cells ($\Delta E_{i,s}$) and for upward droplet growth to reach the pillar top of the current unit cell ($\Delta E_{i,u}$). For a droplet constrained by $n \times n$ unit cells, this energy comparison can be written as a ratio-

$$(\Delta E_i{}^*)_{n\times n} = \frac{(\Delta E_{i,s})_{n\times n}}{(\Delta E_{i,u})_{n\times n}} = \frac{(l-d)(1-\cos\theta_a) - 2nl\cos\theta_a}{4(l-d) - n\pi d\cos\theta_a}. \tag{A.1}$$

A droplet will preferentially grow upward if either $\Delta E_i{}^*$ is greater than 1 or the height of the droplet reaches the pillar tops ($nl \approx h$) before $\Delta E_i{}^* > 1$. With our specific surface geometries, $nl \approx h$ was first satisfied for $n = 5$. Thus, the constrained droplet will grow laterally within 5 unit cells before reaching pillar tops. In the second stage, the droplet now flushed with the pillar tops can either grow sideways or can inflate upward as a Cassie droplet. An energy comparison similar to stage 1 can be used to find out the energetically favorable mode of growth-

$$(\Delta E_f{}^*)_{n\times n} = \frac{(\Delta E_{f,i})_{n\times n}}{(\Delta E_{f,u})_{n\times n}} = \frac{(nl - d)(1 - \cos\theta_a) - 2nh\cos\theta_a}{n\pi l}. \tag{A.2}$$

For our surface, $\Delta E_f{}^* > 1$ is immediately satisfied for the $n = 5$ value obtained from stage 1. Thus as soon as the droplet reaches the pillar tops, it will grow upward. This critical value of n can now be used to find out the neck radius r_p as depicted in Figure A.1. The neck radius is found out to be $r_p \approx 0.5nl = 297.5$ nm for our surface.

A.2 Model of coalescence-induced impalement:

In the main manuscript, the theoretical model assumed that coalescence caused droplet detachment and/or departure from the surface. However, it should also be considered whether coalescence could induce the opposite effect, namely, impalement into the texture. There are three possible mechanisms for coalescence-induced impalement: i) the excess surface energy is much higher than the merged droplet's work of cohesion, such that only a portion of the droplet rips off the impaled necks, ii) the Wenzel state is more favorable than the Cassie state, or iii) the dynamic pressure exerted by the liquid bridge during coalescence exceeds the Laplace pressure required to invade the nanopillars. Each of these will now be considered in turn.

The work of cohesion to break the merged droplet into two pieces is $W_c \approx 2\gamma A$, where A is the surface area of the merged droplet. From volume conservation, $A = 2^{\frac{4}{3}}\pi R^2(2 - 3\cos\theta_{app} + \cos\theta_{app}{}^3)^{\frac{2}{3}}$. With $\theta_{app} = \theta_{adv} \approx 160°$ and initial droplet radius, R= 867 μm we find that $W_c \approx 10^{-6}$. As the work of adhesion to detach two droplets from their respective Wenzel necks ($\Delta E_{ad|N}$) is considerably lower than the work of cohesion, the excess surface energy released during coalescence would first supply the energy required for droplet detachment from the impaled neck before supplying energy for breaking up the merged droplet.

If the Cassie state were merely metastable, then the energy released by coalescence could overcome the energy barrier to switch to the more stable Wenzel state. The Cassie state is energetically favorable over the Wenzel state when [87]:

$$\theta_c = \cos^{-1}\left(\frac{\phi - 1}{r - \phi}\right). \tag{A.3}$$

With $\phi = 0.295$ as the solid fraction and $\theta_a \approx 113°$, we find that $\theta_c = 94.6°$ which indicates that the Cassie state is energetically more favorable in our surface.

During coalescence, a liquid bridge rapidly expands against the substrate due to symmetry breaking. The dynamic pressure due to bridging (ΔP_d) can be approximated by $\rho {v_b}^2$, where $v_b \approx 2{D_0}^2(\gamma/\rho R)^{1/2}$ is the bridging velocity and $D_0 \approx 1.62$ is a prefactor found from numerical simulations [53]. The capillary pressure barrier (ΔP_c) is scaled as $|2\gamma cos\theta_{app}|/p$, where p is the pitch distance between the nanopillars. With $p = 119$ nm, we found that ΔP_c is three orders of magnitude higher than ΔP_d for any micrometric droplets. Thus, in the modeling of the coalescence-induced droplet rolling, we can neglect the work of cohesion or impalement of the merged droplet after coalescence and only compare the excess surface energy of coalescence with the work of adhesion required to detach the merged droplet from the nanostructures.

A.3 Condensation heat transfer coefficient model:

For a condensing superhydrophobic surface, droplet size distribution $n(r)$ for non-interacting droplets is given by [28]:

$$n(r) = \frac{1}{3\pi {r_{col}}^3 r_{max}} \left(\frac{r_{col}}{r_{max}}\right)^{-2/3} \frac{r(r_{col} - r_{min})}{r - r_{min}} \frac{A_2 r + A3}{A_2 r_{col} + A_3} exp(B_1 + B_2) \tag{A.4}$$

and for droplets bigger than the coalescence radius, the droplet size distribution, $N(r)$ is simply given by:

$$N(r) = \frac{1}{3\pi r^2 r_{max}} \left(\frac{r}{r_{max}}\right)^{-2/3} \tag{A.5}$$

Here the constants B_1 and B_2 can be further defined as-

$$B1 = \frac{A2}{\tau A1} \left[\frac{{r^2}_{col} - r^2}{2} + r_{min}(r_{col} - r) - {r^2}_{min} ln\left(\frac{r - r_{min}}{r_{col} - r_{min}}\right)\right]$$

$$B2 = \frac{A3}{\tau A1} \left[r_{col} - r - r_{min} ln\left(\frac{r - r_{min}}{r_{col} - r_{min}}\right)\right]$$

with the sweeping period, τ expressed as-

$$\tau = \frac{3 r_{col}^2 (A_2 r_{col} + A_3)^2}{A_1 (11 A_2 r_{col}^2 - 14 A_2 r_{col} r_{min} + 8 A_3 r_{col} - 11 A_3 r_{min}}$$

and A_1, A_2, A_3 are denoted by-

$$A1 = \frac{\Delta T}{\rho h_{fg} (1 - \cos\theta)^2 (2 + \cos\theta)}, A2 = \frac{\theta}{4 k_w \sin\theta}$$

$$A3 = \frac{1}{2h_i(1 - \cos\theta)} + \frac{1}{k_c \sin^2\theta} \left[\frac{k_p \phi}{\delta_c k_p + h k_c} + \frac{k_w (1 - \phi)}{\delta_c k_w + h k_c}\right]^{-1} \tag{A.6}$$

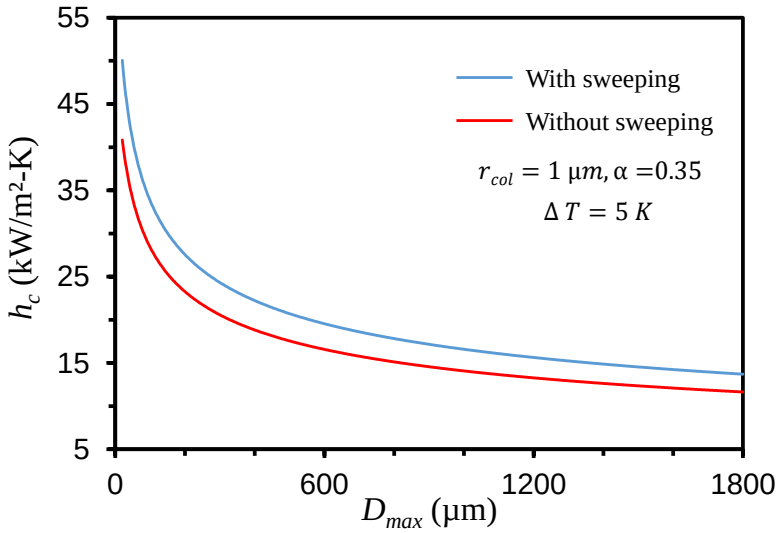

Figure A.2: Effect of sweeping on the condensation heat transfer coefficient. If all other variables are kept constant, the surface with sweeping shows slightly better heat transfer performance. As the two curves are qualitatively same, we have used the model with no sweeping in the main paper.

Here, r_{col} is the coalescence radius above which droplet growth occurs mainly by coalescence. In general, the coalescing length-scale can be optimized by surface structure design. For our surface, this coalescing lengthscale is assumed to be 1 μm which is similar to the coalescing and deparing size observed on an equivalent surface by Mulroe et al. r_{min} is the critical nucleation radius of the condensing droplets on a structured surface which can be taken as 10 nm for water in ambient conditions [6]. The upper bound of the droplet distribution, r_{max} is the maximum droplet radius on the surface. In all previous jumping-droplet heat transfer models it was considered constant as the departure radius of the droplets does not depend on surface inclination in jumping droplet condensation. But even though the critical jumping droplet size is dependent on the surface structures only, the orientation of the surface ultimately controls the maximum droplet size on the surface for long-time condensation. So, in our model, r_{max} is varied within a range of 10 μm to 900 μm, which includes the maximum droplet size seen on our surfaces in our experiments for all three orientations. A key point to note here is that for pure jumping droplet condensation the droplet sweeping is non-existent or the sweeping period, τ is infinite. But, as seen in our experiments, during long term condensation, the surface shows both jumping and sweeping removal of condensing droplets. In such cases the sweeping terms B_1 and B_2 can not be neglected. In Figure A.2, we have compared the heat transfer coefficient with and without sweeping term. As the difference is not substantially large and both of the curves are qualitatively similar, we have neglected the sweeping term in our model.

Appendix B

Spore Dispersal via Jumping-Droplet Condensation

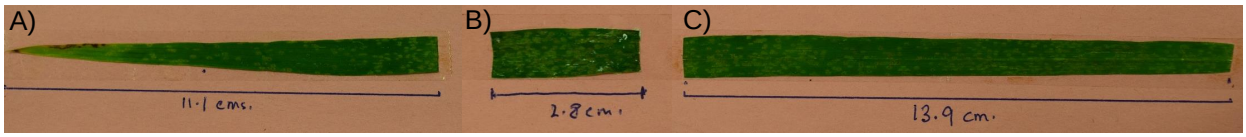

Figure B.1: Dimensions of a healthy wheat leaf cut from the stem. (A) The tip section is of variable width. (B) In the middle, the leaf width is almost uniform ($\approx 1\,\mathrm{cm}$). This $\approx 3\,\mathrm{cm}$ long middle section was used for all of the experiments. (C) The leaf again tapers off toward the end near the stem.

B.1 Derivation of the projectile motion of a jumped droplet (without air flow)

The equation of motion for a droplet jumping off the leaf at an angle θ and initial jumping velocity $u = 0.22(\gamma/\rho R)^{1/2}$ is given by:

$$m\frac{du_x(t)}{dt} = -cu_x(t), \tag{B.1}$$

$$m\frac{du_z(t)}{dt} = -mg - cu_z(t), \tag{B.2}$$

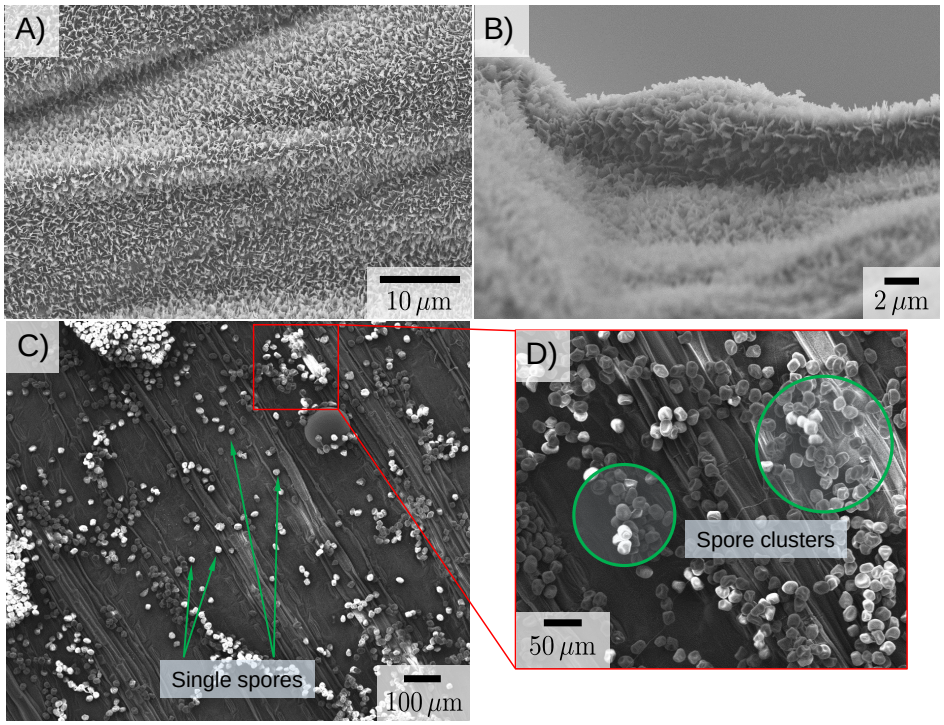

Figure B.2: Scanning electron micrograph (SEM) images of a healthy wheat leaf. (A) 5 kX magnification and (B) 10 kX magnification. The nanometric surface asperities, clearly visible in these images, are generally coated with wax which render the wheat leaves superhydrophobic. (C) SEM images of single spores and spore clusters on a diseased wheat leaf. (D) Careful examination of the spores in the magnified image confirms that they are adhered to the leaf surface.

where $m=(4/3)\rho_{\mathrm{w}}\pi R^3 g$ is the mass of the water droplet of density ρ_{w} and radius R, $c=6\pi\mu R$ is the Stokes drag coefficient, and $v_x(t)$ and $v_z(t)$ are the x and z components of velocity of the airborne droplet. The assumption of Stokes drag is borne out when considering the Reynolds number ($Re=2\rho_{\mathrm{air}}uR/\mu_{\mathrm{air}}$) for the flow around the droplet is low for the range of R values chosen here ($Re\approx 1.6-3.2$). By defining $k:=c/m$, we can rewrite the above differential equations as-

$$\frac{d}{dt}\begin{pmatrix}u_x\\u_z\end{pmatrix}=\frac{d}{dt}\begin{pmatrix}-ku_x\\-g-ku_z\end{pmatrix} \tag{B.3}$$

Using the initial conditions $u_x(0)=u\cos\theta$, $u_z(0)=u\sin\theta$, we can solve for the horizontal and the vertical position of the jumped droplet as a function of time-

$$x(t)=\frac{u_x(0)}{k}(1-e^{-kt}) \tag{B.4}$$

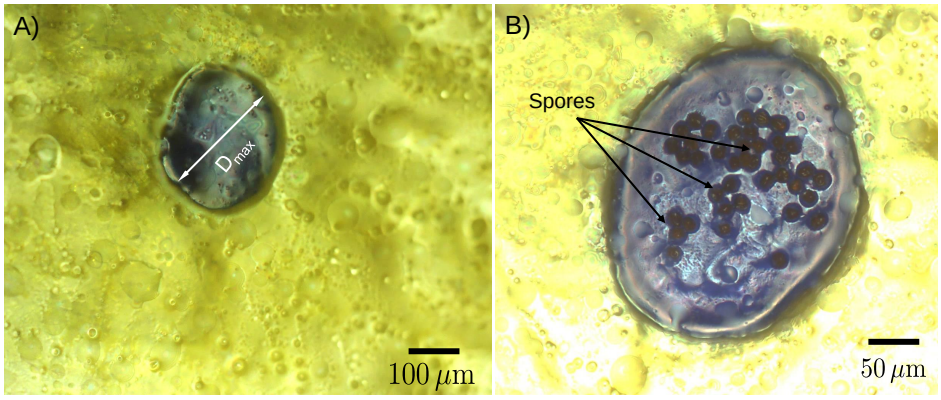

Figure B.3: Stain and spore under microscope. (A) Magnified view of a blue stain caused by a jumping dew droplet landing on water-sensitive paper (yellow). No spores were inside of this particular jumped droplet. The maximum diameter of the stain ($D_{\max}$), shown here, was used for Eq. 1 in the main manuscript. (B) Another example of a stain from a jumped droplet, where in this case there were 39 spores adhered to the droplet. In both cases, there was no wind above the diseased leaf, such that the droplets jumped over the edge of the leaf onto the underlying paper.

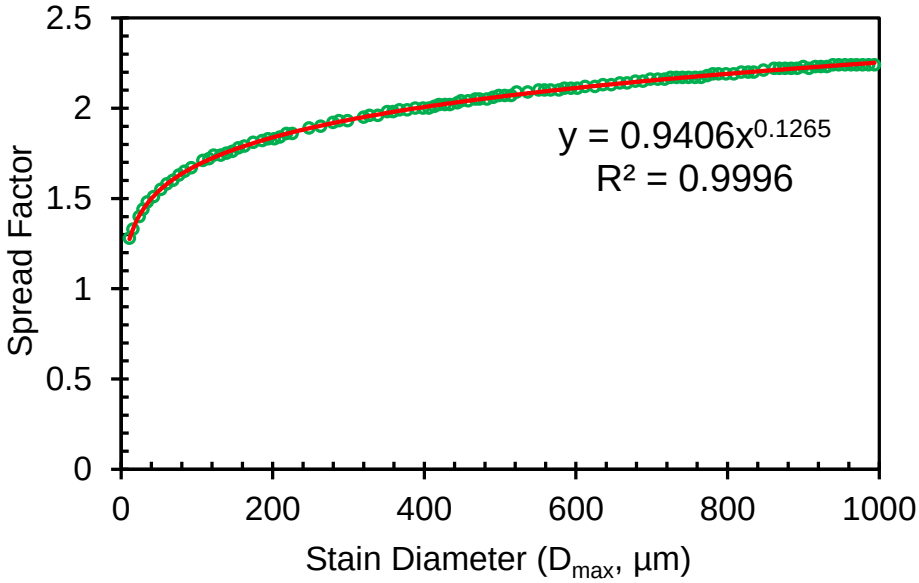

Figure B.4: Spread factor calculation. Spread factor of water droplets on the water-sensitive papers, defined as the ratio of the maximum stain diameter ($D_{\max}$) to the pre-impact droplet diameter. The green data points are extracted from the product datasheet by using a plotting software (WebPlotDigitizer). The smooth red curve is the fitted power-law which was used to obtain the spread factor corresponding to any given stain diameter.

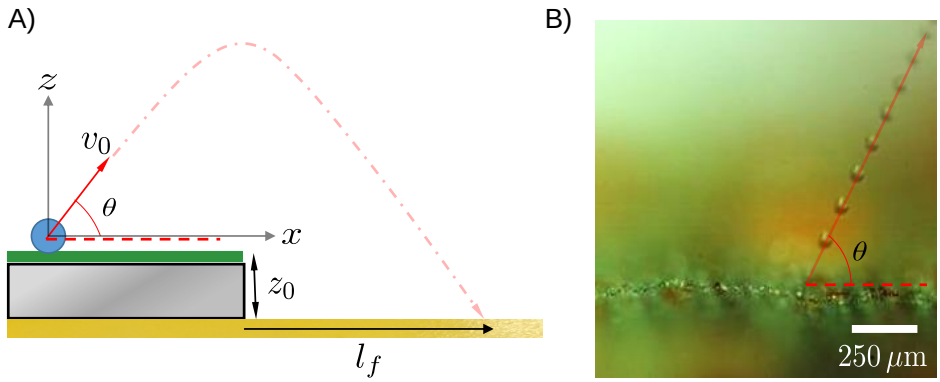

Figure B.5: Projectile motion schematic. (A) Schematic of the projectile motion of a droplet jumping off the leaf. The coordinate axes ($x-z$), jumping velocity (v_0), the angle of the jump (θ), and the trajectory of the airborne droplet is shown. The vertical distance between the leaf and the water-sensitive paper is shown by z_0 which is 1 cm. The distance of the stains on the paper from the edge of the leaf is shown by l_f which is the same as that shown in Fig. 2a in the main text. (B) Chronophotograph of a jumping droplet from a diseased wheat leaf is shown along with the jumping angle θ. Successive positions of the jumped droplet are temporally separated by 40 μs.

$$z(t) = -\frac{g}{k}t + \frac{1}{k}\left(u_z(0) + \frac{g}{k}\right)(1 - e^{-kt}) \tag{B.5}$$

By choosing a value for the droplet radius R, we can plot $x(t) \equiv l(t)$ lines for different values of the jumping angle $\theta = 30°, 60°, 89°$, as shown in Fig. 2c in main text and in Fig. S4. We can also solve for the total time of flight (t_c) for a droplet of radius R by using $z = -0.01$ m in Eq. B.5, which accounts for the droplet returning to the water sensitive paper $y_0 = 1$ cm below the leaf. Three different t_c values were obtained corresponding to the three different θ where the corresponding curves were end.

B.2 Critical speed of removal of dry spores from wheat leaves

The hydrodynamic force exerted by wind with a mean speed of U, on a spherical spore of radius R_p, can be defined as-

$$F_{\text{shear}} \approx 1.7 \times 6\pi\mu_a\dot{\gamma}{R_p}^2, \tag{B.6}$$

where μ_a is the viscosity of air and $\dot{\gamma} \approx U/\delta$ is the velocity gradient within a boundary layer of thickness δ [267]. The boundary layer thickness is again related to the leaf section size x and the free stream wind speed U as $\delta \sim \left(\frac{\nu x}{U}\right)^{1/2}$. This shear force has to overcome the adhesion force exerted by the surface on the particle. For a completely dry leaf with uncharged spores, this adhesion force is mainly due to the van der Waals force:

$$F_{\text{vdW}} \approx (A/6z^2)R_{\text{p}}, \tag{B.7}$$

where A is the Hamaker constant and z is the closest possible separation distance between the awn surface and the spore [268]. For most organic molecules, $A \sim 10^{-20}$ J [268] and z is taken as 1 nm due to the nanoscopic surface asperities.

The theoretical critical wind speed for the removal of the dry spores ($R_{\text{p}} \sim 10\,\mu$m) can then be found by combining all of the above equations:

$$U_{\text{c}} = \left(\frac{(A/6z^2)}{1.7 \times 6\pi\mu_{\text{a}}R_{\text{p}}(\nu x)^{-1/2}}\right)^{2/3}, \tag{B.8}$$

which comes out to be about 10 m/s taking $x \sim 1$ cm which is in general the width of a wheat leaf, and $\mu_{\text{a}} = 1.81 \times 10^{-5}$ Pa·s and $\nu = 1.5 \times 10^{-5}$ m^{2}s^{-1}. While this is larger than the experimental threshold wind speed for dry spore removal [131], this discrepancy comes from the assumption of a fixed Hamaker constant and the separation distance values. A Hamaker constant of $A \sim 10^{-21}$ J, which is still within the acceptable range of values for a wide varitey of surface and particle combination and a slightly increased separation distance of 2 nm gives $U_{\text{c}} \approx 2.9$ m/s which is very close to the experimental critical wind speed value reported in Ref. [131].

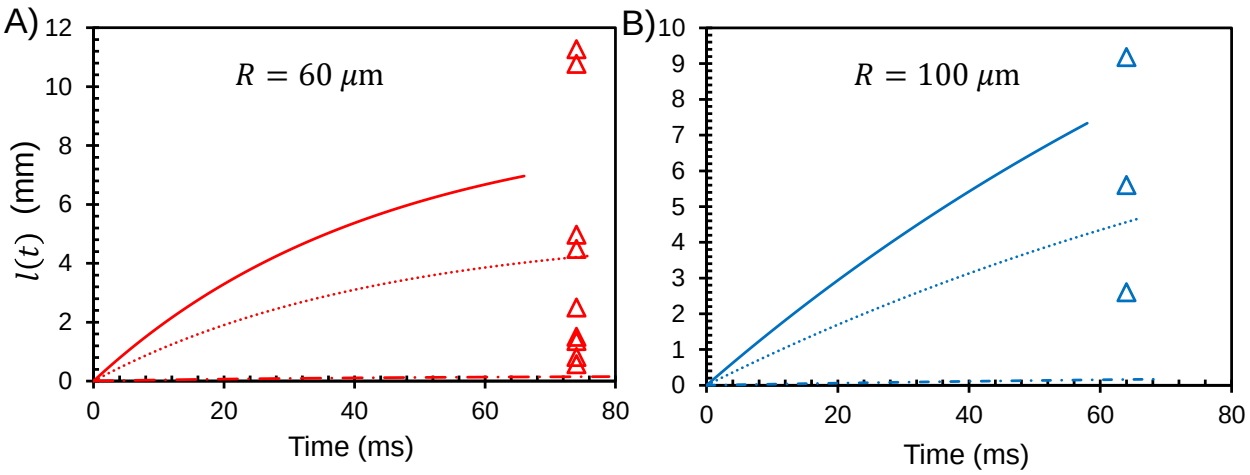

Figure B.6: The lateral displacement versus time for a jumping droplet of radius $R = 60\,\mu$m, and $100\,\mu$m, respectively. Each graph shows the displacement curves for three different jumping angles with respect to the horizontal: 30° (solid curve), 60° (dotted), and 89° (dash-dotted). The maximum lateral displacement for a jumped droplet (l_f) is represented by the terminal end of each curve. The value of l_f corresponds to the critical time when the projectile motion equation predicts the droplet will impact on the water-sensitive paper below (mimicking a neighboring leaf). For these plots, the paper was placed 1 cm beneath the leaf. Experimental values of l_f are also overlaid on the same plot as symbols. The jumped droplet radius were calculated from the stain diameters on the papers via the spread factors (see Section 2). Although the majority of the experimental data points fall within the theoretical limits, some droplets did travel farther than the theoretical l_f. This can be explained by droplets getting boosted by the air circulation in the laboratory, as can be seen in Supporting Video S1 where the lateral displacement of jumping droplets is several times larger during the downward descent compared to the upward launch. This air circulation was quite mild, as it was less than the 0.4 m/s resolution of the anemometer, but this is sufficient in the context of affecting micrometric droplets.

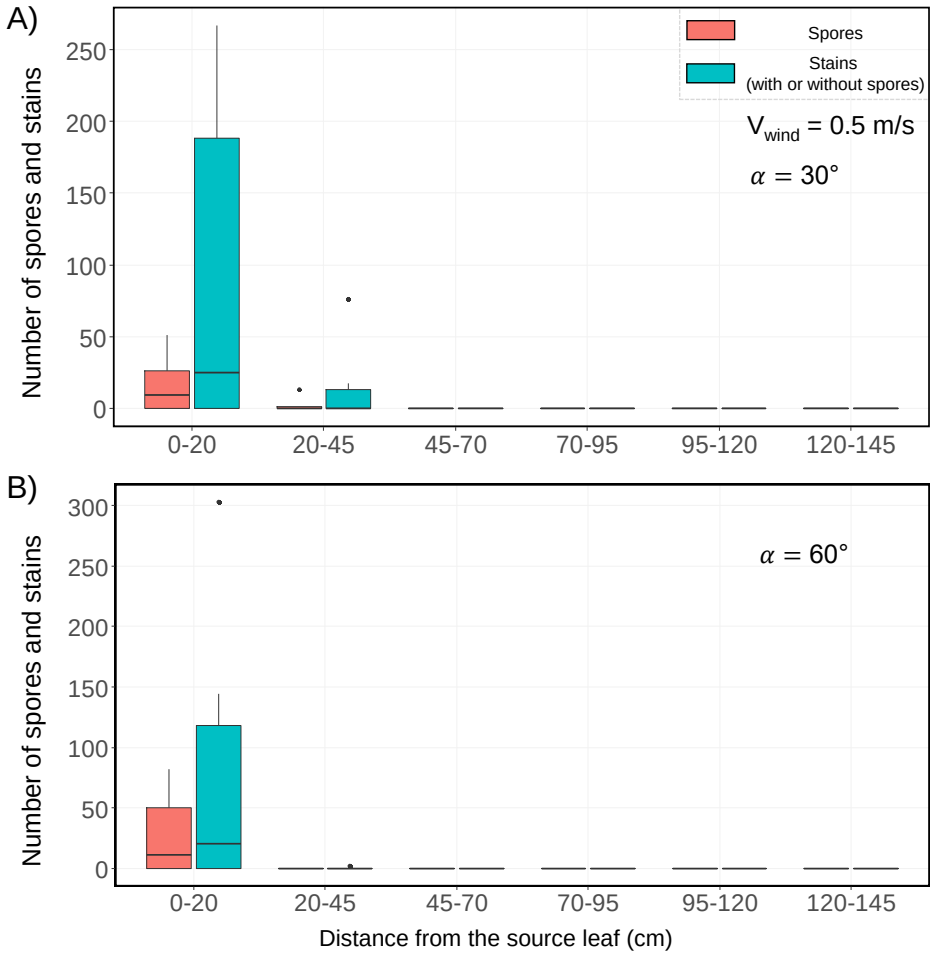

Figure B.7: The number of impacted droplets (with or without spores) and the number of spores per paper are plotted against the distance from the source leaf for $V_{\text{wind}} = 0.5\,\text{m/s}$. All distances are measured along the (A) $\alpha = 30°$ and (B) $\alpha = 60°$ lines. No droplets were captured on the papers placed along the $\alpha = 45°$ line.

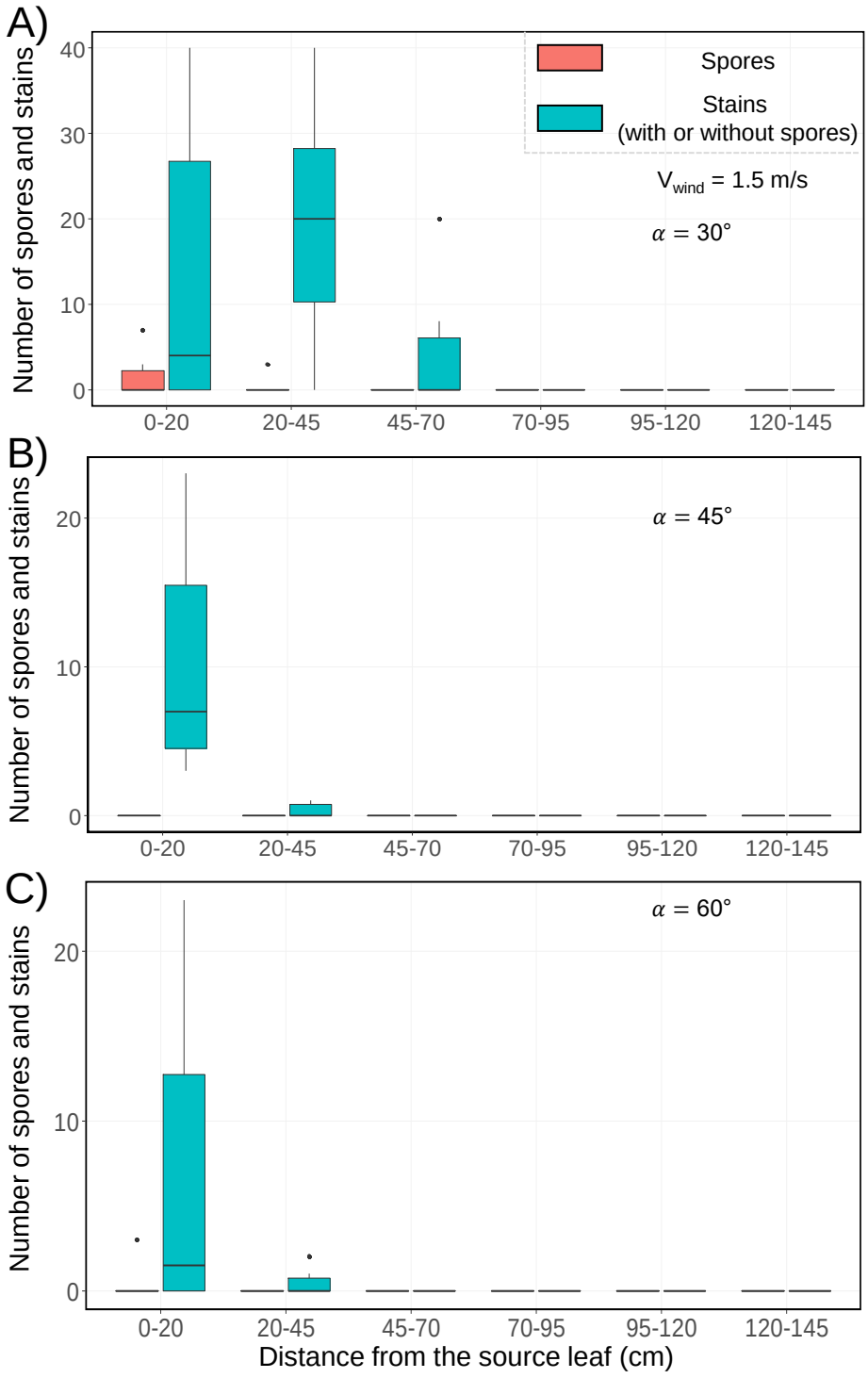

Figure B.8: The number of impacted droplets (with or without spores) and number of spores per paper are plotted against the distance from the source leaf for $V_{\text{wind}} = 1.5\,\text{m/s}$. All distances are measured along the (A) $\alpha = 30°$, (B) $\alpha = 45°$, and (C) $\alpha = 60°$ lines.

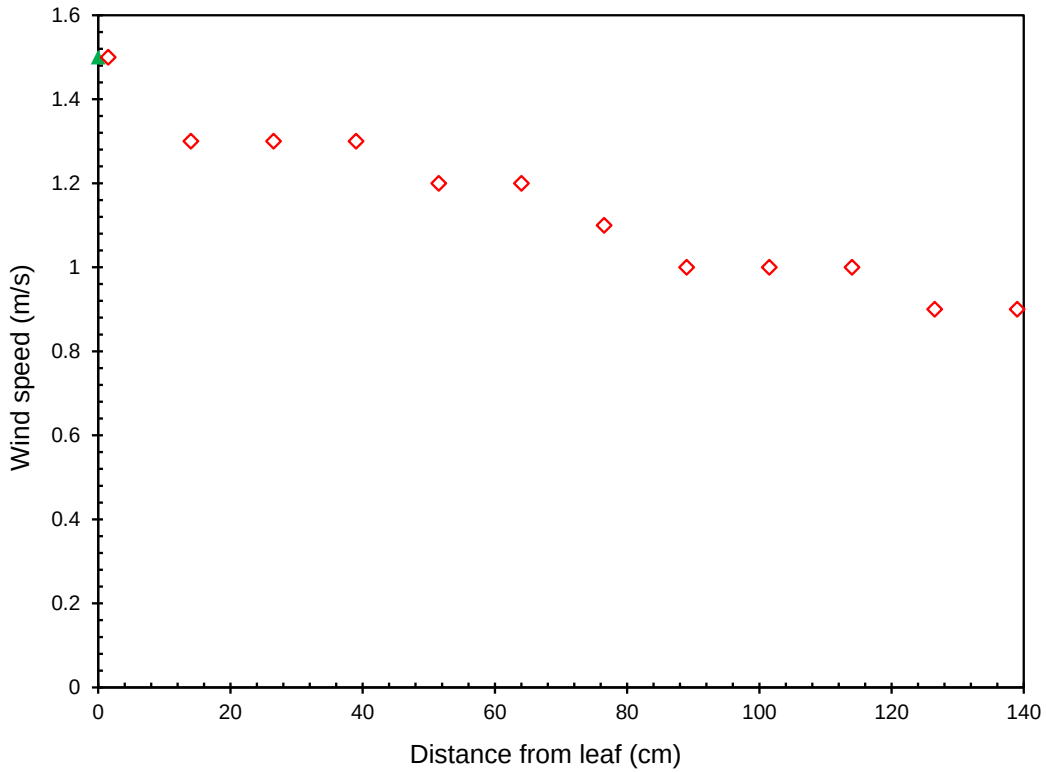

Figure B.9: Spatial variation of the wind speed downwind of the leaf, as measured 1 cm above the array of water-sensitive papers. This plot is only for the papers placed along the $\alpha = 0°$ line downstream of the leaf. The green triangle indicates the wind speed ($V_{\text{wind}} = 1.5\,\text{m/s}$) 1 cm above the leaf. A similar plot is not available for $V_{\text{wind}} = 0.5\,\text{m/s}$, as equivalent drop in the wind velocity with distance resulted in a wind speed lower than 0.3 m/s, below the minimum measurable value for the anemometer used in our study.

Appendix C

Jumping Frost

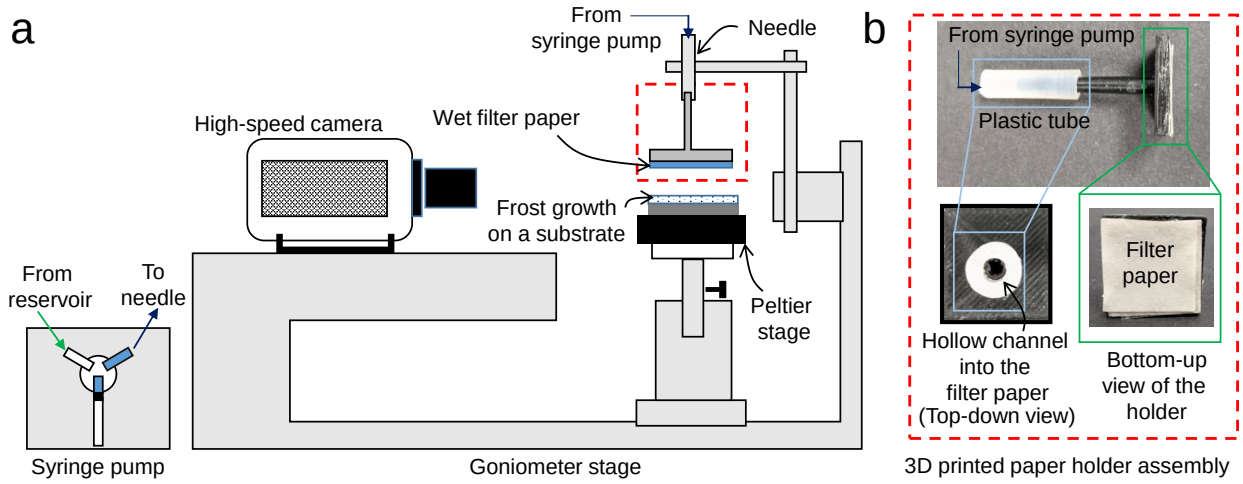

Figure C.1: (a) Experimental setup for jumping frost experiments in a room temperature environment. The syringe pump supplied a known volume of water to the needle assembly, where a 3D-printed paper holder was attached in place of a needle. (b) Details of the 3D-printed paper holder assembly. The white plastic tube was attached to the paper holder for proper fitting with the needle holder. Water from the syringe pump came directly to the needle reservoir, flowed through the hollow channel, and finally wetted the filter paper at the base.

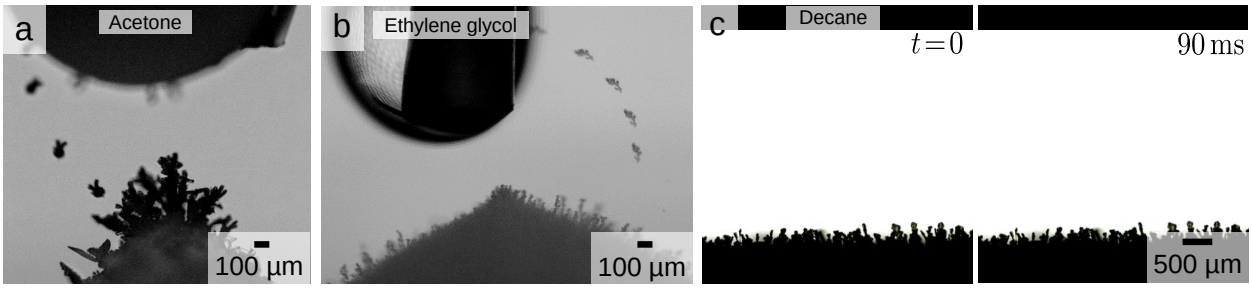

Figure C.2: Frost jumping for different polar and non-polar liquids. Chronophotograph of frost jumping opposite to (a) an acetone droplet and (b) an ethylene glycol droplet. The frost in both cases was grown on top of the pointy tip of a frozen droplet, which was in turn resting on a $T_s \approx -40$ °C substrate. (c) No jumping was observed between the two frames separated by 90 ms when a thin film of decane was placed opposite to the frosted substrate. The total time for which we observed the system was about 5 min, to ensure that no jumping was occurring.

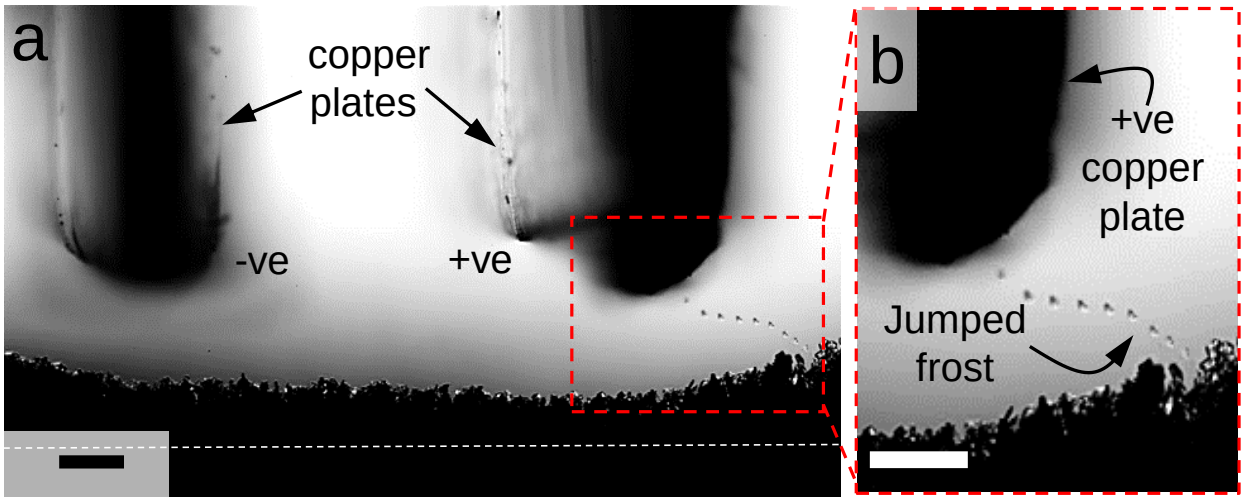

Figure C.3: Charged copper plate above frost. When two parallel copper plates were connected to the positive and negative terminals of a 36 V DC power supply and held over a frosted substrate, the frost preferentially jumped into the positive plate. The same behavior shown here was observed for five different trials. This preliminary experimental result confirms that broken frost dendrites carry negative charges, in agreement with the Latham and Mason theory we adapted in this manuscript. The white dashed line shows the substrate at the base of the frost layer. Scale bars represent 500 μm.

C.1 Dielectric material in an external electric field

Before discussing the electric field simulations in detail, it is important to point out the difference in behavior of a dielectric object and a conductor in an external electric field. As a conductor is also a dielectric with infinite permitivitty, we can generalize and obtain the electric field inside and outside of a dielectric sphere of radius a and relative permitivitty ϵ in an external electric field E_0 from the electric potential relation in a two dimensional field $r-z$ [166]:

$$\phi_{\text{in}} = -\frac{3E_0}{\epsilon/\epsilon_m + 2} z, \tag{C.1}$$

$$\phi_{\text{out}} = -E_0 z + \frac{\epsilon/\epsilon_m - 1}{\epsilon/\epsilon_m + 2} \frac{a^3 E_0}{\left(r^2 + z^2\right)^{3/2}} z, \tag{C.2}$$

where ϵ_m is the relative permitivitty of the medium around the sphere. The electric field now can be obtained simply by taking the gradient of the potential with $E = -\nabla\phi$. When a conducting sphere is placed in an external electric field, no field can exist inside the sphere, as the free charges inside the conductor move until the internal field is neutralized (Fig. SC.4(a)). Surprisingly, when we replaced the conducting sphere with a water droplet ($\epsilon \approx 80$), we found the internal field to be very weak due to a high ϵ/ϵ_m ratio (Fig. SC.4(b)). For our purposes we have thus neglected this field and have treated the water droplet and the water film as a conductor with surface potentials for the electric field calculations. For the demonstrations we have used an open source *Mathematica* code which uses C.1 and C.2.

C.2 Details of the numerical simulation

The numerical simulation in Chapter 5.3.4 is performed using COMSOL® Multiphysics. Within the simplified one dimensional domain, the equation set (Eq. 5.3-5.9) is solved with the built-in finite element method based solver. To capture the ions' evolving near the boundary characterized by the Debye length and save computational cost, a non-uniform mesh is utilized. The domain length is set to be 0.1 mm. The element size close to the wall is set as 0.3 μm which is 20 times smaller than the relevant Debye length and the growth rate is set to be 1.2. Total 53 elements were used with the maximum element size in bulk set at 2.5 μm. The total simulation time is 5 s with 1 ms as the time interval.

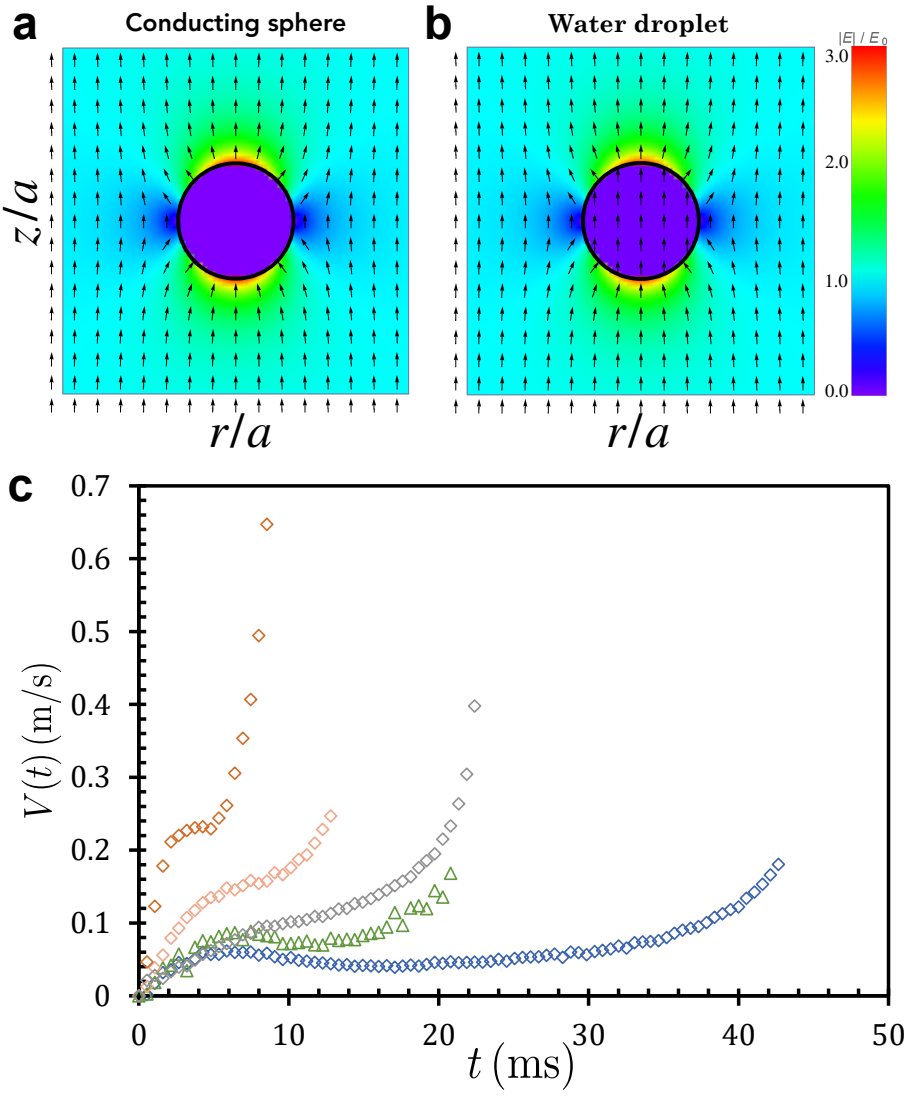

Figure C.4: Electric field theory. Electric field inside and just outside a (a) conducting sphere and (b) water droplet of radius a when placed in a uniform field of strength E_0. The field lines inside the water droplet shows the existence of a very weak internal field compared to zero internal field for the conducting sphere. (c) $V(t)$ *vs.* t plot for the jumped frost particles when a water droplet was placed opposite to the frosted substrate. The second acceleration period is evident at later times when the jumped frost particles come near the hanging droplet. The diamonds and the triangles are experimental data with $H \geq 2\,\text{mm}$ and $H < 2\,\text{mm}$, respectively.

Appendix D

Hydrocarbon-based Polymer SLIPS

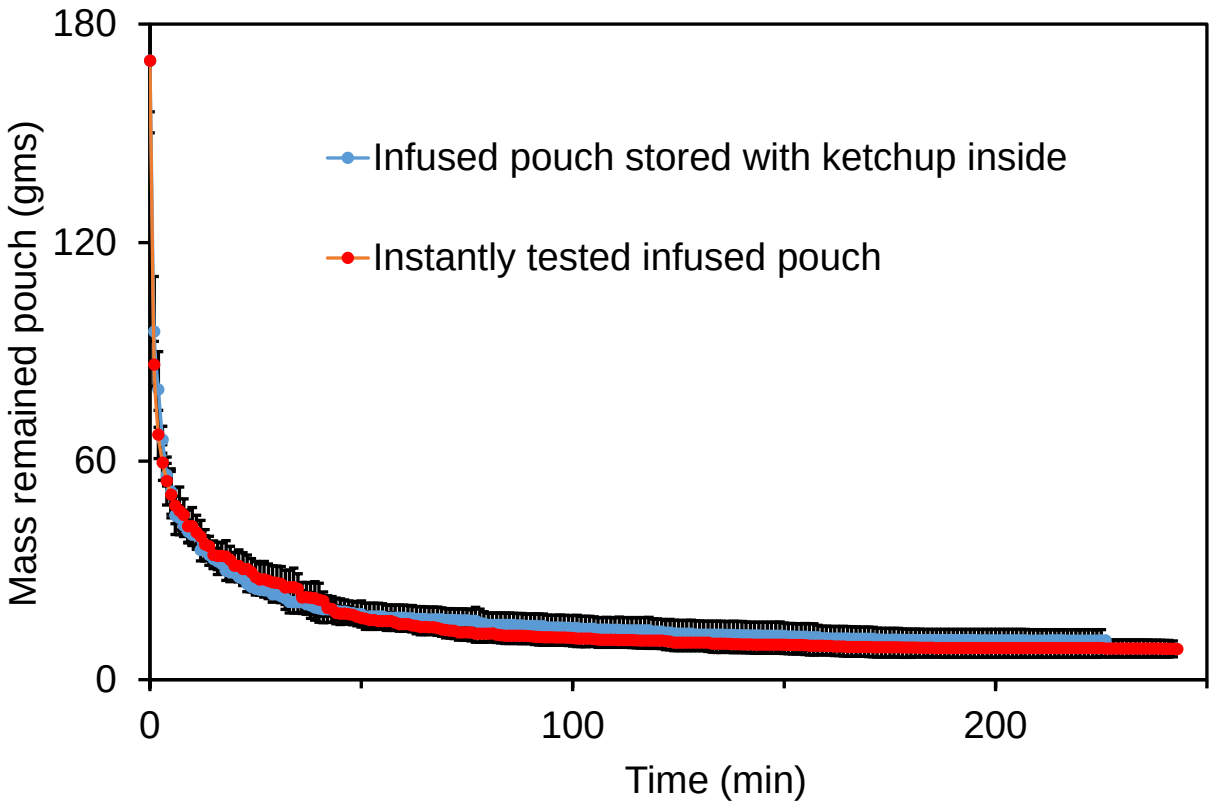

Figure D.1: Submersion test. Drainage rates of ketchup being poured out of pouches comprised of oil-impregnated ULDPE films (see Section 4.5 in main text). There was no change in performance when draining pouches freshly filled with ketchup (red line) with pouches that were stored with ketchup for 53 days (blue line). This indicates the excellent stability of the impregnated oil within the ULDPE films. All error bars represent a standard deviation obtained from three trials.

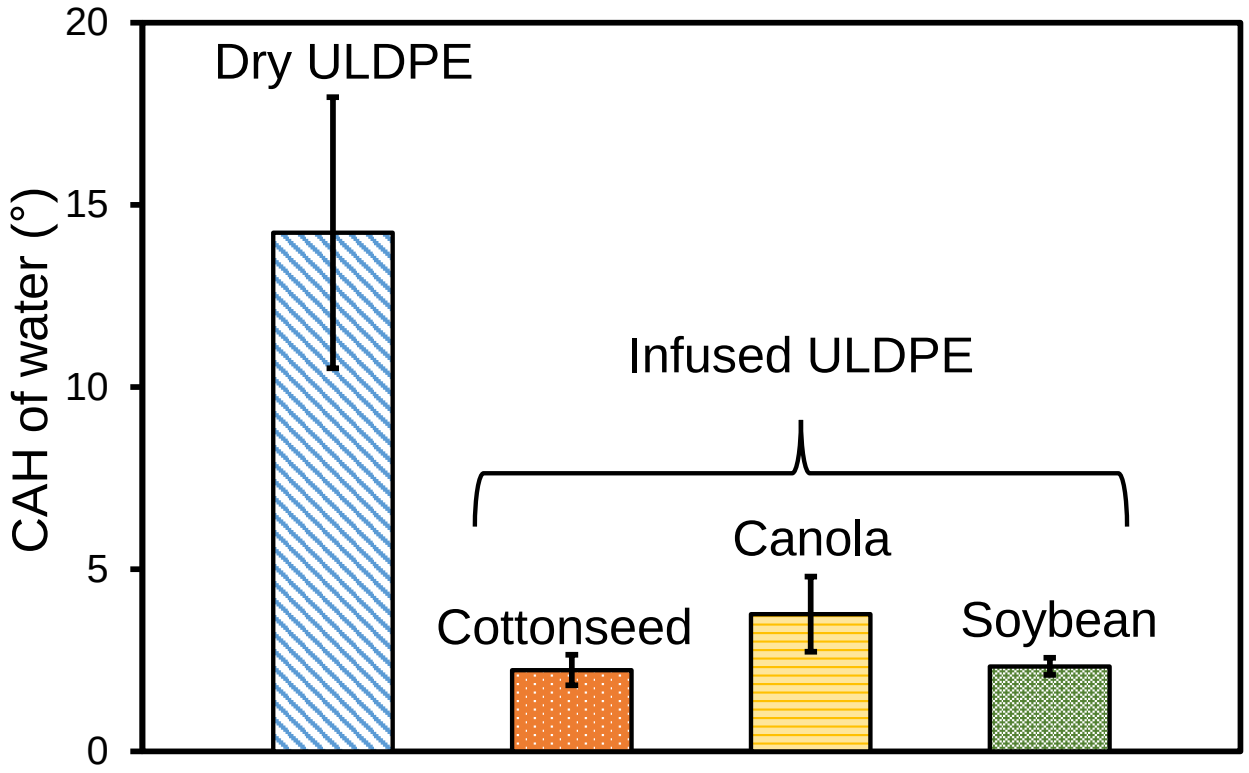

Figure D.2: Testing with different oils for infusion. When ULDPE films were impregnated with chemically compatible vegetable oils, the contact angle hysteresis (CAH) of water droplets was reduced to $<5°$.

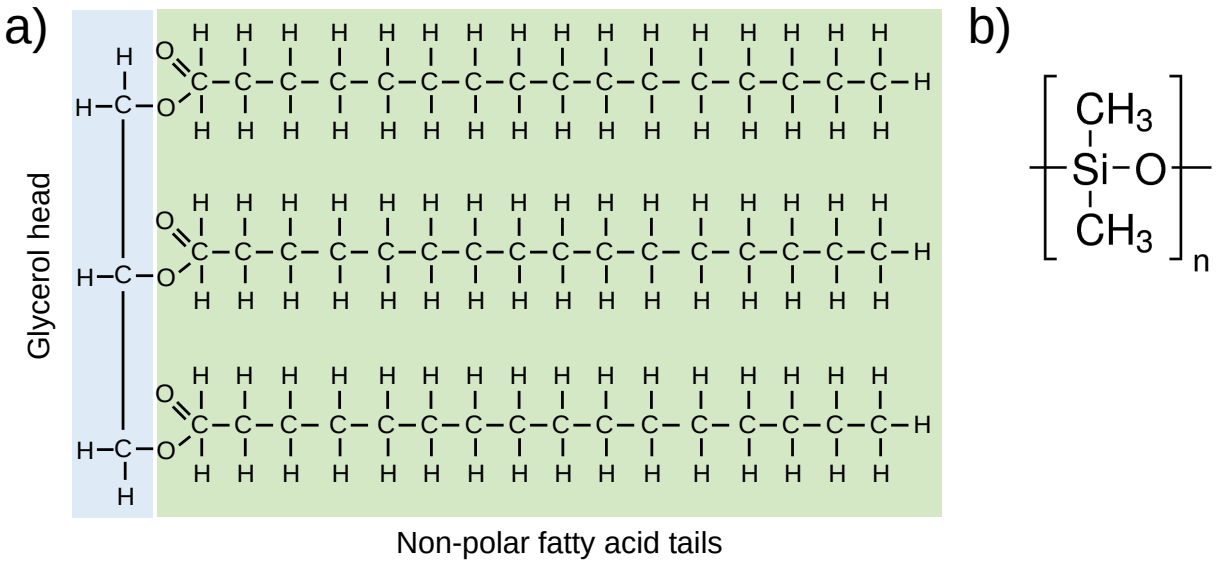

Figure D.3: Molecular structure of two oils. a) Typical molecular structure of a saturated triglyceride. Triglycerides are the main components in vegetable fats and oils. A triglyceride molecule consists of three fatty acid molecules (shown in light green) connected to a glycerol backbone (shown in light blue). Due to the presence of these long hydrocarbon tails, triglycerides are non-polar in nature. b) A silicone oil (PDMS) molecular structure consists of Si-O bond and adjacent methyl groups. Due to the presence of this polar Si-O bond, silicone oil is polar in nature.

Bibliography

[1] V. Fayod. Prodrome d'une histoire naturelle des agaricine`s. *Ann. Sci. Ser.*, 9:181–411, 1889.

[2] A. Buller. *Researches on Fungi, Vol. 1.* Longmans, Green, and Co., 1909.

[3] JJ. Webster, R. A. Davey, and C. T. Ingold. Origin of liquid in buller's drop. *Trans. British Mycol. Soc.*, 83:524–527, 1984.

[4] J. C. R. Turner and J. Webster. Mass and momentum transfer on the small scale: how do mushrooms shed their spores? *Chem. Eng. Sci.*, 46:1145–1149, 1991.

[5] D. Beysens. Dew nucleation and growth. *C. R. Physique*, 7:1082–1100, 2006.

[6] V. P. Carey. *Liquid–Vapor Phase-Change Phenomena, 2^{nd} ed.* CRC Press, Boca Raton, FL, 2007.

[7] W. Thomson. On the equilibrium of vapor at a curved surface of liquid. *Phil. Mag.*, 42:448–452, 1871.

[8] R. von Helmholtz. Untersuchungen über dämpfe und nebel, besonders über solche von lösungen. *Annalen der Physik*, 263:508–543, 1886.

[9] N. N. D. Gupta and S. K. Ghosh. A report on the wilson cloud chamber and its applications in physics. *Rev. Modern Phys.*, 18:225–290, 1946.

[10] M. Kollera and U. Grigull. Über das abspringen von tropfen bei der kondensation von quecksilber (The bouncing off phenomenon of droplets with condensation of mercury). *Heat and Mass Transfer*, 2:31–35, 1969.

[11] J. B. Boreyko and C. H. Chen. Self-propelled dropwise condensate on superhydrophobic surfaces. *Phys. Rev. Lett.*, 103:184501, 2009.

[12] E. Schmidt, W. Schurig, and W. Sellschopp. Versuche uber die kondensation von wasserdampf in film- and tropfenform. *Forsch. Ingenieurwes.*, 1:53–63, 1930.

[13] J. W. Rose. Dropwise condensation theory and experiment: a review. *Proc. Inst. Mech. Eng., Part A*, 216:115–128, 2002.

[14] E. J. Le Fevre and J. W. Rose. An experimental study of heat transfer by dropwise condensation. *Int. J. Heat Mass Transfer*, 8:1117–1133, 1965.

[15] E. Citakoglu and J. W. Rose. Dropwise condensation -the effect of surface inclination. *Int. J. Heat Mass Transfer*, 12:645–651, 1969.

[16] C. P. Migliaccio. Resonance-induced condensate shedding for high-efficiency heat transfer. *Int. J. Heat Mass Transfer*, 79:720–726, 2014.

[17] A. J. B. Milne and A. Amirfazil. Drop shedding by shear flow for hydrophilic to superhydrophobic surfaces. *Langmuir*, 25:14,155–14,164, 2009.

[18] P. hao, C. Lv, and Z. Yao. Droplet detachment by air flow for microstructured superhydrophobic surfaces. *Langmuir*, 29:5160–5166, 2013.

[19] M. S. Bonab, R. Kempers, and A. Amirfazil. Determining transient heat transfer coefficient for dropwise condensation in the presence of an air flow. *Langmuir*, 173:121278, 2021.

[20] Y. T. Cheng and D. E. Rodak. Is the lotus leaf superhydrophobic? *Appl. Phys. Lett.*, 86:144101, 2005.

[21] F. Liu, G. Ghigliotti, J. J. Feng, and C. H. Chen. Numerical simulations of self-propelled jumping upon drop coalescence on non-wetting surfaces. *J. Fluid Mech.*, 752:39–65, 2014.

[22] N. Miljkovic, R. Enright, Y. Nam, K. Lopez, N. Dou, J. Sack, and E. N. Wang. Jumping-droplet-enhanced condensation on scalable superhydrophobic nanostructured surfaces. *Nano Lett.*, 13:179–187, 2012.

[23] K. M. Wisdom, J. A. Watson, X. Qu, F. Liu, G. S. Watson, and C. H. Chen. Self-cleaning of superhydrophobic surfaces by self-propelled jumping condensate. *Proc. Natl. Acad. Sci. U.S.A.*, 110:7992–7997, 2013.

[24] S. Nath, S. F. Ahmadi, H. A. Gruszewski, S. Budhiraja, C. E. Bisbano, S. Jung, D. G. Schmale III, and J. B. Boreyko. 'sneezing' plants: pathogen transport via jumping-droplet condensation. *J. Royal Soc. Interface*, 16, 2019.

[25] M. D. Mulroe, B. R. Srijanto, S. F. Ahmadi, C. P. Collier, and J. B. Boreyko. Tuning superhydrophobic nanostructures to enhance jumping-droplet condensation. *ACS Nano*, 1:8499—8510, 2017.

[26] H. Cha, C. Xu, J. Sotelo, J. M. Chun, Y. Yokoyama, R. Enright, and N. Miljkovic. Coalescence-induced nanodroplet jumping. *Phys. Rev. Fluids*, 1:064102, 2016.

[27] J. B. Boreyko, Y. Zhao, and C. H. Chen. Planar jumping-drop thermal diodes. *Appl. Phys. Lett.*, 99:234105, 2011.

[28] N. Miljkovic, R. Enright, and E. N. Wang. Modeling and optimization of superhydrophobic condensation. *J. Heat Transfer*, 135:111004, 2013.

[29] D. Quéré. Wetting and roughness. *Annu. Rev. Mater. Res.*, 38:71–99, 2008.

[30] T. Onda, S. Shibuichi, N. Satoh, and K. Tsujii. Super water-repellent surfaces resulting from fractal structure. *J. Phys. Chem.*, 100:19,512–17, 1996.

[31] T. Onda, S. Shibuichi, N. Satoh, and K. Tsujii. Super water-repellent fractal structures. *Langmuir*, 12:12125–2127, 1996.

[32] G. Dupeux, P. Bourrianne, Q. Magdelaine, C. Clanet, and D. Quéré. Propulsion on a superhydrophobic ratchet. *Sci. Rep.*, 4:5280, 2014.

[33] R. N. Wenzel. Resistance of solid surfaces to wetting by water. *Ind. Eng. Chem.*, 28:988–994, 1936.

[34] J. Bico, U. Thiele, and D. Quéré. Wetting of textured surfaces. *Colloid Surface A*, 206:41–46, 2002.

[35] A. Lafuma and D. Quéré. Slippery pre-suffused surfaces. *Europhys. Lett.*, 96:56001, 2011.

[36] C. Ishino, M. Reyssat, E. Reyssat, K. Okumura, and D. Quéré. Wicking within forests of micropillars. *Europhys. Lett.*, 79:56005, 2007.

[37] T. S. Wong, S. H. Kang, S. K. Y. Tang, E. J. Smythe, B. D. Hatton, A. Grinthal, and J. Aizenberg. Bioinspired self-repairing slippery surfaces with pressure-stable omniphobicity. *Nature*, 477:443–447, 2011.

[38] J. D. Smith, R. Dhiman, S. Anand, E. Reza-Garduno, R. E. Cohen, G. H. McKinley, and K. K. Varanasi. Droplet mobility on lubricant-impregnated surfaces. *Soft Matter*, 9:1772–1780, 2013.

[39] D. Quéré. Rough ideas on wetting. *Physica A*, 313:32–46, 2002.

[40] D. K. Sarkar and M. Farzanehc. Superhydrophobic coatings with reduced ice adhesion. *J. Adhes. Sci. Technol.*, 23:1215–1237, 2009.

[41] K. Golovin, S.P. Kobaku, D. H. Lee, E. T. DiLoreto, J. M. Mabry, and A. Tuteja. Designing durable icephobic surfaces. *Sci. Adv.*, 2:e1501496, 2016.

[42] X. Sun and K. Rykaczewski. Suppression of frost nucleation achieved using the nano-engineered integral humidity sink effect. *ACS Nano*, 11:906–917, 2016.

[43] K. R. Murphy, W. T. McClintic, K. C. Lester, C. P. Collier, and J. B. Boreyko. Dynamic defrosting on scalable superhydrophobic surfaces. *ACS Appl. Mater. Interfaces*, 9:24308–24317, 2017.

[44] D. L. Beemer, W. Wang, and A. K. Kota. Durable gels with ultra-low adhesion to ice. *J. Mater. Chem. A*, 4:18253–18258, 2016.

[45] C. Stamatopoulos, J. Hemrle, D. Wang, and D. Poulikakos. Exceptional anti-icing performance of self-impregnating slippery surfaces. *ACS Appl. Mater. Interfaces*, 9:10233–10242, 2017.

[46] K. Rykaczewski, S. Anand, S. B. Subramanyam, and K. K. Varanasi. Mechanism of frost formation on lubricant-impregnated surfaces. *Langmuir*, 29:5230–5238, 2013.

[47] D. Torresin, M. K. Tiwari, D. D. Col, and D. Poulikakos. Flow condensation on copper-based nanotextured superhydrophobic surfaces. *Langmuir*, 29:840–848, 2013.

[48] T.M. Schutzius, S. Jung, T. Maitra, G. Graeber, M. Kohme, and D. Poulikakos. Spontaneous droplet trampolining on rigid superhydrophobic surfaces. *Nature*, 527:82–85, 2015.

[49] G. Graeber, T. M. Schutzius, H. Eghlidi, and D. Poulikakos. Spontaneous self-dislodging of freezing water droplets and the role of wettability. *Proc. Natl. Acad. Sci. U.S.A.*, 114:11040–11045, 2017.

[50] S. F. Ahmadi, S. Nath, G. J. Iliff, B. R. Srijanto, C. P. Collier, P. Yue, and J. B. Boreyko. Passive anti-frosting surfaces using microscopic ice patterns. *ACS Appl. Mater. Interfaces*, 10:32874–32884, 2018.

[51] R. Mukherjee, A. S. Berrier, K. R. Murphy, J. R. Vieitez, and J. B. Boreyko. How surface orientation affects jumping-droplet condensation. *Joule*, 3:1360–1376, 2019.

[52] J. W. Rose. Some aspects of condensation heat transfer theory. *Int. Commun. Heat Mass*, 15:449–473, 1988.

[53] J. Oh, R. Zhang, P. P. Shetty, J. A. Krogstad, P. V. Braun, and N. Miljkovic. Thin film condensation on nanostructured surfaces. *Adv. Funct. Mater.*, 1707000:1–10, 2018.

[54] D. Beysens and C. M. Knobler. Growth of breath figures. *Phys. Rev. Lett.*, 57:1433–1436, 1986.

[55] D. Fritter, C. M. Knobler, and D. A. Beysens. Experiments and simulation of the growth of droplets on a surface (breath figures). *Phys. Rev. A*, 43:2858–2869, 1991.

[56] E. J. Le Fevre and J. W. Rose. A theory of heat transfer by dropwise condensation. In *Proceedings of the Third International Heat Transfer Conference*, pages 362–375, Chicago, IL, August 7–12 1966.

[57] I. Tanasawa. Critical size of departing drops. In *Proceedings of the Fifth International Heat Transfer Conference*, volume 7, page 188, Tokyo, Japan, September 3–7 1974.

[58] G. Koch, D. C. Zhang, and A. Leipertz. Condensation of steam on the surface of hard coated copper discs. *Heat and Mass Transfer*, 32:149–156, 1997.

[59] T. Mouterde, Gaélle Lehoucq, Stéphane Xavier, A. Checco, C. T. Black, A. Rahman, T. Midavaine, C. Clanet, and D. Quéré. Antifogging abilities of model nanotextures. *Nat. Mater.*, 16:658–663, 2017.

[60] N. Miljkovic, R. Enright, and E. N. Wang. Effect of droplet morphology on growth dynamics and heat transfer during condensation on superhydrophobic nanostructured surfaces. *ACS Nano*, 6:1776–1785, 2012.

[61] J. Zhu, Y. Luo, J. Tian, J. Li, and X. Gao. Clustered ribbed-nanoneedle structured copper surfaces with high-efficiency dropwise condensation heat transfer performance. *ACS Appl. Mater. Interfaces*, 7:10660–10665, 2015.

[62] N. Miljkovic, D. J. Preston, R. Enright, and E. N. Wang. Electric-field-enhanced condensation on superhydrophobic nanostructured surfaces. *ACS Nano*, 7:11043–11054, 2013.

[63] P. Birbarah, Z. Li, A. Pauls, and N. Miljkovic. A comprehensive model of electric-field-enhanced jumping-droplet condensation on superhydrophobic surfaces. *Langmuir*, 31:7885–7896, 2015.

[64] R. Wen, S. Xu, X. Ma, Y. C. Lee, and R. Yang. Three-dimensional superhydrophobic nanowire networks for enhancing condensation heat transfer. *Joule*, 2:269–279, 2018.

[65] Y. Hou, M. Yu, X. Chen, Z. Wang, and S. Yao. Recurrent filmwise and dropwise condensation on a beetle mimetic surface. *ACS Nano*, 9:71–81, 2015.

[66] E. Olceroglu and M. McCarthy. Self-organization of microscale condensate for delayed flooding of nanostructured superhydrophobic surfaces. *ACS Appl. Mater. Interfaces*, 8:5729–5736, 2016.

[67] J. B. Boreyko and C. H. Chen. Self-propelled jumping drops on superhydrophobic surfaces. *Phys. Fluids*, 22:091110, 2010.

[68] R. Enright, N. Miljkovic, J. Sprittles, K. Nolan, R. Mitchell, and E. N. Wang. How coalescing droplets jump. *ACS Nano*, 8:10352–10362, 2014.

[69] T. Mouterde, T. V. Nguyen, H. Takahashi, C. Clanet Christophe, I. Shimoyama, and D. Quéré. How merging droplets jump off a superhydrophobic surface: Measurements and model. *Phys. Rev. Fluids*, 2:112001, 2017.

[70] K. Rykaczewski, A.T. Paxson, S. Anand, X. Chen, Z. Wang, and K. K. Varanasi. Multimode multidrop serial coalescence effects during condensation on hierarchical superhydrophobic surfaces. *Langmuir*, 29:881–891, 2013.

[71] C. Lv, P. Hao, Z. Yao, and F. Niu. Departure of condensation droplets on superhydrophobic surfaces. *Langmuir*, 31:2414–2420, 2015.

[72] M. He, X. Zhou, X. Zeng, D. Cui, Q. Zhang, J. Chen, H. Li, J. Wang, Z. Cao, Y. Song, and L. Jiang. Hierarchically structured porous aluminum surfaces for high-efficient removal of condensed water. *Soft Matter*, 8:6680–6683, 2012.

[73] K. Wang, R. Li, Q. Liang, R. Jiang, Y. Zheng, Z. Lan, and X. Ma. Critical size ratio for coalescence-induced droplet jumping on superhydrophobic surfaces. *Appl. Phys. Lett.*, 111:061603, 2017.

[74] J. Wasserfall, P. Figueiredo, R. Kneer, W. Rohlfs, and P. Pischke. Coalescence-induced droplet jumping on superhydrophobic surfaces: Effects of droplet mismatch. *Phys. Rev. Fluids*, 2:123601, 2017.

[75] J. B. Boreyko, G. Polizos, P. G. Datskos, S. A. Sarles, and C. P. Collier. Air-stable droplet interface bilayers on oil-infused surfaces. *Proc. Natl. Acad. Sci. U.S.A.*, 111:7588–7593, 2014.

[76] C. Dietz, K. Rykaczewski, A. G. Fedorov, and Y. Joshi. Visualization of droplet departure on a superhydrophobic surface and implications to heat transfer enhancement during dropwise condensation. *Appl. Phys. Lett.*, 97:033104, 2010.

[77] X. Chen, J. Wu, R. Ma, M. Hua, N. Koratkar, S. Yao, and Z. Wang. Nanograssed micropyramidal architecture for continuous dropwise condensation. *Adv. Funct. Mater.*, 21:4617–4623, 2011.

[78] J. B. Boreyko and C. P. Collier. Delayed frost growth on jumping-drop superhydrophobic surfaces. *ACS Nano*, 7:1618–1627, 2013.

[79] X. Chen, J. A. Weibel, and S. V. Garimella. Exploiting microscale roughness on hierarchical superhydrophobic copper surfaces for enhanced dropwise condensation. *Adv. Mater. Interfaces*, 2:1400480, 2015.

[80] E. Olceroglu, C. Y. Hsieh, M. M. Rahman, K. K. S. Lau, and M. McCarthy. Full-field dynamic characterization of superhydrophobic condensation on biotemplated nanostructured surfaces. *Langmuir*, 30:7556–7566, 2014.

[81] J. B. Boreyko and C. H. Chen. Vapor chambers with jumping-drop liquid return from superhydrophobic condensers. *Int. J. Heat Mass Transfer*, 61:409–418, 2013.

[82] P. Birbarah and N. Miljkovic. External convective jumping-droplet condensation on a flat plate. *Int. J. Heat Mass Transfer*, 107:74–88, 2017.

[83] C. G. L. Furmidge. Studies at phase interfaces i. the sliding of liquid drops on solid surfaces and a theory for spray retention. *J. Colloid Sci.*, 17:309–324, 1962.

[84] R. Enright, N. Miljkovic, A. Al-Obeidi, C. V. Thompson, and E. N. Wang. Condensation on superhydrophobic surfaces: the role of local energy barriers and structure length scale. *Langmuir*, 28:14424–14432, 2012.

[85] K. Rykaczewski. Microdroplet growth mechanism during water condensation on superhydrophobic surfaces. *Langmuir*, 28:7720–7729, 2012.

[86] J. B. Boreyko, C. H. Baker, C. R. Poley, and C. H. Chen. Wetting and dewetting transitions on hierarchical superhydrophobic surfaces. *Langmuir*, 27:7502–7509, 2011.

[87] A. Lafuma and D. Quéré. Superhydrophobic states. *Nat. Mater.*, 2:457–460, 2003.

[88] E. Bormashenko, R. Pogreb, G. Whyman, Y. Bormashenko, and M. Erlich. Vibration-induced Cassie-Wenzel wetting transition on rough surfaces. *Appl. Phys. Lett.*, 90:201917, 2007.

[89] T. Verho, J. T. Korhonen, L. Sainiemi, V. Jokinen, C. Bower, K. Franze, S. Franssila, P. Andrew, O. Ikkala, and R. H. A. Ras. Reversible switching between superhydrophobic states on a hierarchically structured surface. *Proc. Natl. Acad. Sci. U.S.A.*, 109:10210–10213, 2012.

[90] J. B. Boreyko and C. P. Collier. Dewetting transitions on superhydrophobic surfaces: when are Wenzel drops reversible? *J. Phys. Chem. C*, 117:18084–18090, 2013.

[91] R. Enright, N. Miljkovic, N. Dou, Y. Nam, and E. N. Wang. Condensation on superhydrophobic copper oxide nanostructures. *J. Heat Transfer*, 135:091304, 2013.

[92] X. Qu, J. B. Boreyko, F. Liu, R. L. Agapov, N. V. Lavrik, S. T. Retterer, J. J. Feng, C. P. Collier, and C. H. Chen. Self-propelled sweeping removal of dropwise condensate. *Appl. Phys. Lett.*, 106:221601, 2015.

[93] C. Lv, P. Hao, Z. Yao, Y. Song, X. Zhang, and F. He. Condensation and jumping relay of droplets on lotus leaf. *Appl. Phys. Lett.*, 103:021601, 2013.

[94] C. Dorrer and J. Ruhe. Condensation and wetting transitions on microstructured ultrahydrophobic surfaces. *Langmuir*, 23:3820–3824, 2007.

[95] C. Lv, P. Hao, X. Zhang, and F. He. Dewetting transitions of dropwise condensation on nanotexture-enhanced superhydrophobic surfaces. *ACS Nano*, 9:12311–12319, 2015.

[96] J. L. Viovy, D. A. Beysens, and C. M. Knobler. Scaling description for the growth of condensation patterns on surfaces. *Phys. Rev. A*, 37:4965–4970, 1988.

[97] H. Zhao and D. Beysens. From droplet growth to film growth on a heterogeneous surface: condensation associated with a wettability. *Langmuir*, 11:627–634, 1995.

[98] S. Kim and K. J. Kim. Dropwise condensation modelling suitable for superhydrophobic surfaces. *J. Heat Transfer*, 133:081502, 2011.

[99] K. Nabavian and L. A. Bromley. Condensation coefficient of water. *Chem. Eng. Sci.*, 18:651–660, 1963.

[100] D. W. Tanner, C. J. Potter, D. Pope, and D. West. Heat transfer in dropwise condensation—part i the effects of heat flux, steam velocity and non-condensable gas concentration. *Int. J. Heat Mass Transfer*, 8:419–426, 1965.

[101] W. J. Minkowycz and E. M. Sparrow. Condensation heat transfer in the presence of noncondensables, interfacial resistance, superheating, variable properties, and diffusion. *Int. J. Heat Mass Transfer*, 9:1125–1144, 1966.

[102] Y. Zhao, D. J. Preston, Z. Lu, L. Zhang, J. Queeney, and E. N. Wang. Effects of millimetric geometric features on dropwise condensation under different vapor conditions. *Int. J. Heat Mass Transfer*, 119:931–938, 2018.

[103] D. J. Preston and E. N. Wang. Jumping droplets push the boundaries of condensation heat transfer. *Joule*, 2:205–207, 2018.

[104] R. Mukherjee, H. A. Gruszewski, L. T. Bilyeu, D. G. Schmale III, and J. B. Boreyko. Synergistic dispersal of plant pathogen spores by jumping-droplet condensation and wind. *Proc. Natl. Acad. Sci. U.S.A.*, 2021 (Just Accepted).

[105] D. E. Aylor. The role of intermittent wind in the dispersal of fungal pathogens. *Annu. Rev. Phytopathol.*, 28:73–92, 1990.

[106] C. T. Ingold. *Spore discharge in land plants*. Clarendon Press, Oxford, 1939.

[107] F. Liu, R. L. Chavez, S. N. Patek, A. Pringle, J. J. Feng, and C. H. Chen. Asymmetric drop coalescence launches fungal ballistospores with directionality. *J. Royal Soc. Interface*, 14(132):20170083, 2017.

[108] M. W. F. Fischer, J. L. Stole-Rybczynski, Y. Cui, and N. P. Money. How far and how fast can mushroom spores fly? physical limits on ballistospore size and discharge distance in the basidiomycota. *Fungal Biology*, 114:669–675, 2012.

[109] L. Yafetto, L. Carroll, Y. Cui, D. J. Davis, M. W. Fischer, A. C. Henterly, J. D. Kessler, H. A. Kilroy, J. B. Shidler, J. L. Stolze-Rybczynski, Z. Sugawara, and N. P. Money. The fastest flights in nature: high-speed spore discharge mechanisms among fungi. *PloS one*, 3:e3237, 2008.

[110] H. A. McCartney. Dispersal of spores and pollen from crops. *Grana*, 33:76–80, 1994.

[111] A. Bainbridge and B. J. Legg. Release of barleymildew conidia from shaken leaves. *Trans. Brit. Mycol. Soc.*, 66:495–498, 1976.

[112] D. E. Aylor. Force required to detach conidia of *Helminthosporium maydis*. *Plant Physiology*, 55:99–101, 1975.

[113] K. D. Srivastava, L. M. Joshi, and S. Nagarajan. Liberation of uredospores of *Puccinia recondita tritici* under varying wind speeds. *Indian Phytopathol.*, 40:474–477, 1987.

[114] J.M Hirst and O.J. Stedman. Dry liberation of fungus spores by raindrops. *J. Gen. Microbiol*, 33:335–344, 1963.

[115] S. Kim, H. Park, H. A. Gruszewski, D. G. Schmale III, and S. Jung. Vortex-induced dispersal of a plant pathogen by raindrop impact. *Proc. Natl. Acad. Sci. U.S.A.*, 116:4917–4922, 2019.

[116] T. Gilet and L. Bourouiba. Fluid fragmentation shapes rain-induced foliar disease transmission. *J. Royal Soc. Interface*, 12:20141092, 2015.

[117] H. Park, S. Kim, H. A. Gruszewski, D. G. Schmale III, J. B. Boreyko, and S. Jung. Dynamics of splashed droplets impacting wheat leaves treated with a fungicide. *J. Royal Soc. Interface*, 17:20200337, 2020.

[118] I. Sache. Short-distance dispersal of wheat rust spores. *Agronomie*, 20:757–767, 2000.

[119] B. D. L. Fitt, H. A. McCartney, and P. J. Walklate. The role of rain in dispersal of pathogen inoculum. *Annu. Rev. Phytopathol.*, 27:241–270, 1989.

[120] S. Nagarajan and D. V. Singh. Long-distance dispersion of rust pathogens. *Annu. Rev. Phytopathol.*, 28:139–153, 1990.

[121] D.E. Aylor. A framework for examining inter-regional aerial transport of fungal spores. *Agr. Forest Meteorol.*, 38:263–288, 1986.

[122] L. Geagea, L. Huber, and I. Sache. Dry-dispersal and rain-splash of brown (*Puccinia recondita* f.sp. tritici) and yellow (*P. striiformis*) rust spores from infected wheat leaves exposed to simulated raindrops. *Plant Pathol.*, 48:472–482, 1999.

[123] C. L. Campbell and L. V. Madden. *Introduction to plant disease epidemiology*. Wiley, 1990.

[124] J. K. M. Brown and M. S. Hovøller. Aerial dispersal of pathogens on the global and continental scales and its impact on plant disease. *Science*, 297:537–541, 2002.

[125] H. A. McCartney and B. D. L. Fitt. *Dispersal of foliar fungal plant pathogens: mechanisms, gradients and spatial patterns*. Springer, 1998.

[126] M. Abichou, B. de Solan, and B. Andrieu. Architectural response of wheat cultivars to row spacing reveals altered perception of plant density. *Front. Plant Sci.*, 10:999, 2019.

[127] X. Yan, L. Zhang, S. Sett, L. Feng, C. Zhao, Z. Huang, H. Vahabi, A. K. Kota, F. Chen, and N. MIljkovic. Droplet jumping: effects of droplet size, surface structure, pinning, and liquid properties. *ACS Nano*, 13:1309–1323, 2019.

[128] H. Lamb. *Hydrodynamics*. Dover Publications, New York, 1994.

[129] R. C. Faulwetter. Wind-blown rain, a factor in disease dissemination. *J. Agric. Res.*, 10:639–648, 1917.

[130] R. D. Narhe and D. A. Beysens. Water condensation on a super-hydrophobic spike surface. *Europhys. Lett.*, 75:98–104, 2006.

[131] L. Geagea, L. Huber, and I. Sache. Removal of urediniospores of brown (puccinia recondita f.sp. tritici) and yellow (p. striiformis) rusts of wheat from infected leaves submitted to a mechanical stress. *Eur. J. Plant Pathol.*, 103:785–793, 1997.

[132] S. Gart, J. E. Mates, C. M. Megaridis, and S. Jung. Droplet impacting a cantilever: a leaf-raindrop system. *Phys. Rev. Appl.*, 3:044019, 2015.

[133] C. H. Chen, Q. Cai, C. Tsai, C. L. Chen, G. Xiong, Y. Yu, and Z. Ren. Dropwise condensation on superhydrophobic surfaces with two-tier roughness. *Appl. Phys. Lett.*, 90:173108, 2007.

[134] D. Quéré. Non-sticking drops. *Rep. Prog. Phys.*, 68:2495–2532, 2005.

[135] G. S. Watson, M. Gellender, and J. A. Watson. Self-propulsion of dew drops on lotus leaves: a potential mechanism for self cleaning. *Biofouling*, 30:427–434, 2014.

[136] B. D. L. Fitt, P. H. Gregory, A. D. Todd, H. A. McCartney, and O. C. Macdonald. Spore dispersal and plant disease gradients; a comparison between two empirical models. *J. Phytopathol.*, 118:227–242, 1987.

[137] B. Mockenhaupt, H. J. Ensikat, M. Spaeth, and W. Barthlott. Superhydrophobicity of biological and technical surfaces under moisture condensation: stability in relation to surface structure. *Langmuir*, 24:13591–13597, 2008.

[138] C. Neinhuis and W. Barthlott. Characterization and distribution of water-repellent, self-cleaning plant surfaces. *Annals of Botany*, 79:667–677, 1997.

[139] K. Koch and W. Barthlott. Superhydrophobic and superhydrophilic plant surfaces: an inspiration for biomimetic materials. *Phil. Trans. R. Soc. A*, 367:1487–1509, 2009.

[140] R. Mukherjee, S. F. Ahmadi, H.Zhang, R. Qiao, and J. B. Boreyko. Electrostatic jumping of frost. *ACS Nano*, 15:4669–4677, 2021.

[141] I.D. Brindle and R.H. Tomlinson. Deflection of falling solvents by an electric field. *J. Chem. Edu.*, 52:382–383, 1975.

[142] X. Su, L. Lianos, Y. Ron Shen, and G. A. Somorjai. Surface-induced ferroelectric ice on pt(111). *Phys. Rev. Lett.*, 80:1533–1536, 1998.

[143] T. Takahashi. Electrification of growing ice crystals. *J. Atmos. Sci.*, 30:1220–1224, 1973.

[144] E. J. Workman and S. E. Reynolds. Electrical phenomena occurring during the freezing of dilute aqueous solutions and their possible relationship to thunderstorm electricity. *Phys. Rev.*, 78:254–260, 1950.

[145] J. Latham and B. J. Mason. Electric charge transfer associated with temperature gradients in ice. *Proc. R. Soc. Lond. A*, 260:523–536, 1961.

[146] C. Jaccard. Thermoelectric effects in ice crystals: I. theory of the steady state. *Phys. Kondens. Materie.*, 1:143–151, 1963.

[147] W. Findeisen. über die entstehung der gewitterelektrizität. *Meteor. Z.*, 57:201–215, 1940.

[148] J. Latham. The electrification of frost deposits. *Quart. J. R. Met. Soc.*, 91:265–270, 1963.

[149] Y. Dong and J. Hallett. Charge separation by ice and water drops during growth and evaporation. *J. Geophys. Res. Atmos.*, 97:20,361–20,371, 1992.

[150] V. J. Schaefer and R. J. Cheng. The production of ice crystal fragments by sublimation and electrification. *J. Rech. Atmos.*, 5:5–10, 1971.

[151] T. W. Zawidzki and H. M. Papée. Pseudo-whiskers of ice, grown from clouds of supercooled water in an electric field. *Nature*, 196:568–569, 1962.

[152] J. T. Bartlett, A. P. van den Hueval, and B. J. Mason. The growth of ice crystals in an electric field. *Z. Angew. Math. Phys.*, 14:599–610, 1963.

[153] B. Vonnegut. Orientation of ice crystals in the electric field of a thunderstorm. *Weather*, 20:310–312, 1965.

[154] V. J. Schaefer. The generation of large number of ice crystals in an electric field. *J. Appl. Meteorol. Climatol.*, 7:452–455, 1968.

[155] T. Bharathidasan, S. V. Kumar, M. S. Bobji, R. P. S. Chakradhar, and B. J. Basu. Effect of wettability and surface roughness on ice-adhesion strength of hydrophilic, hydrophobic and superhydrophobic surfaces. *Appl. Surf. Sci.*, 314:241–250, 2014.

[156] M. He, J. Wang, H. Li, and Y. Song. Super-hydrophobic surfaces to condensed micro-droplets at temperatures below the freezing point retard ice/frost formation. *Soft Matter*, 7(8):3993–4000, 2011.

[157] S. Nath, S. F. Ahmadi, and J. B. Boreyko. A review of condensation frosting. *Nanosc. Microsc. Therm.*, 21:81–101, 2017.

[158] Y. Xie, D. Bos, L. J. de Vreede, H. L. de Boer, M. van der Meulen, M. Versluis, A. J. Sprenkels, A. van den Berg, and J. C. T. Eijkel. High-efficiency ballistic electrostatic generator using microdroplets. *Nat. Commun.*, 5:3575, 2014.

[159] B. J. Mason. A critical examination of theories of charge generation in thunderstorms. *Tellus*, 5:446–460, 1953.

[160] J. Latham and C. D. Stow. Electrification associated with the evaporation of ice. *J. Atmos. Sci.*, 22:320–324, 1965.

[161] L. Pauling. The structure and entropy of ice and of other crystals with some randomness of atomic arrangement. *J. Am. Chem. soc.*, 57:2680–2684, 1935.

[162] J. D. Bernal and R. H. Fowler. A theory of water and ionic solution, with particular reference to hydrogen and hydroxyl ions. *J. Chem. Phys.*, 1:515–548, 1933.

[163] N. Bjerrum. Structure and properties of ice. *Science*, 115:385–390, 1952.

[164] V. F. Petrenko and R. W. Whitworth. *Physics of Ice*. Oxford Univ. Press, Oxford, 1999.

[165] K. G. Libbrecht. Physical dynamics of ice crystal growth. *Annu. Rev. Mater. Res.*, 47:271–295, 2017.

[166] J. D. Jackson. *Classical electrodynamics*. John Wiley & Sons, New York, 1999.

[167] J. Guardiola, V. Rojo, and G. Ramos. Influence of particle size, fluidization velocity and relative humidity on fluidized bed electrostatics. *J. Electrostat.*, 37:1–20, 1996.

[168] E. Kapon. *Semiconductor Lasers I: Fundamentals*. Academic Press, Cambridge, MA, 1999.

[169] P. A. Seifert. *The potential difference in ice crystal due to the thermoelectric effect*. PhD thesis, North Dakota State University, 2003.

[170] H. Gao and H. Yao. Shape insensitive optimal adhesion of nanoscale fibrillar structures. *Proc. Natl. Acad. Sci. U.S.A.*, 101:7851–7856, 2004.

[171] S. F. Ahmadi, S. Nath, C. M. Kingett, P. Yue, and J. B. Boreyko. How soap bubbles freeze. *Nat. Commun.*, 10:2531, 2019.

[172] E. Virot, A. Ponomarenko, É. Dehandschoewercker, D. Quéré, and C. Clanet. Critical wind speed at which trees break. *Phys. Rev. E*, 93:023001, 2016.

[173] J. Fineberg, S. P. Gross, M. Marder, and H. L. Swinney. Instability in dynamic fracture. *Phys. Rev. Lett.*, 67:457–460, 1991.

[174] J. Latham and B. J. Mason. Generation of electric charge associated with the formation of soft hail in thunderclouds. *Proc. R. Soc. Lond. A*, 260:537–549, 1961.

[175] R. Mukherjee, M. Habibi, Z. T. Rashed, O. Berbert, X. Shi, and J. B. Boreyko. Oil-impregnated hydrocarbon-based polymer films. *Sci. Rep.*, 8:11698, 2018.

[176] J. Cui, D. Daniel, A. Grinthal, K. Lin, and J. Aizenberg. Dynamic polymer systems with self-regulated secretion for the control of surface properties and material healing. *Nat. Mater.*, 14:790–795, 2015.

[177] D. Daniel, M. N. Mankin, R. A. Belisle, T. S. Wong, and J. Aizenberg. Lubricant-infused micro/nano-structured surfaces with tunable dynamic omniphobicity at high temperatures. *Appl. Phys. Lett.*, 102:231603, 2013.

[178] P. Zhang, H. Chen, L. Zhang, Y. Zhang, D. Zhang, , and L. Jiang. Stable slippery liquid-infused anti-wetting surface at high temperatures. *J. Mater. Chem. A*, 4:12212—12220, 2016.

[179] A. K. Epstein, T. S. Wong, R. A. Belisle, E. M. Boggs, and J. Aizenberg. Liquid-infused structured surfaces with exceptional anti-biofouling performance. *Proc. Natl. Acad. Sci. U.S.A.*, 109:13182–13187, 2012.

[180] L. Xiao, J. Li, S. Mieszkin, A. Di Fino, A.S. Clare, M.E. Callow, J.A. Callow, M. Grunze, A. Rosenhahn, and P.A. Levkin. Slippery liquid-infused porous surfaces showing marine antibiofouling properties. *ACS Appl. Mater. Interfaces*, 5:10074–10080, 2013.

[181] D. C. Leslie, A. Waterhouse, J. B. Berthet, T. M. Valentin, A. L. Watters, A. Jain, P. Kim, B. D. Hatton, A. Nedder, K. Donovan, E. H. Super, C. Howell, C. P. Johnson, T. L. Vu, D. E. Bolgen, S. Rifai, A. R. Hansen, M. Aizenberg, M. Super, J. Aizenberg, and D. E. Ingber. A bioinspired omniphobic surface coating on medical devices prevents thrombosis and biofouling. *Nat. Biotechnol.*, 32:1134–1140, 2014.

[182] N. MacCallum, C. Howell, P. Kim, D. Sun, R. Friedlander, J. Ranisau, O. Ahanotu, J. J. Lin, A. Vena, B. Hatton, T. S. Wong, and J. Aizenberg. Liquid-infused silicone as a biofouling-free medical material. *ACS Biomater. Sci. Eng.*, 1:43–51, 2015.

[183] U. Manna, N. Raman, M.A. Welsh, Y.M. Zayas-Gonzalez, H.E. Blackwell, S.P. Palecek, and D.M. Lynn. Slippery liquid-infused porous surfaces that prevent microbial surface fouling and kill non-adherent pathogens in surrounding media: A controlled release approach. *Adv. Funct. Mater.*, 26:3599–3611, 2016.

[184] J. Lee, S. Shin, Y. Jiang, C. Jeong, H.A. Stone, and C.H. Choi. Oil-impregnated nanoporous oxide layer for corrosion protection with self-healing. *Adv. Funct. Mater.*, 27:1606040, 2017.

[185] Y. Kovalenko, I. Sotiri, J. V. I. Timonen, J. C. Overton, G. Holmes, J. Aizenberg, and C. Howell. Bacterial interactions with immobilized liquid layers. *Adv. Healthcare Mater.*, 6:1600948, 2017.

[186] P. Wang, D. Zhang, S. Sun, T. Li, and Y. Sun. Fabrication of slippery lubricant-infused porous surface with high underwater transparency for the control of marine biofouling. *ACS Appl. Mater. Interfaces*, 9:972–982, 2017.

[187] H. Liu, P. Zhang, M. Liu, S. Wang, and L. Jiang. Organogel-based thin films for self-cleaning on various surfaces. *Adv. Mater.*, 25:4477–4481, 2013.

[188] P. Kim, T. S. Wong, J. Alvarenga, M. J. Kreder, W. E. Adorno-Martinez, and J. Aizenberg. Liquid-infused nanostructured surfaces with extreme anti-ice and anti-frost performance. *ACS Nano*, 6:6569–6577, 2012.

[189] L. Zhu, J. Xue, Y. Wang, Q. Chen, J. Ding, and Q. Wang. Ice-phobic coatings based on silicon-oil-infused polydimethylsiloxane. *ACS Appl. Mater. Interfaces*, 5:4053–4062, 2013.

[190] S. B. Subramanyam, K. Rykaczewski, and K. K. Varanasi. Ice adhesion on lubricant-impregnated textured surfaces. *Langmuir*, 29:13414–13418, 2013.

[191] P. W. Wilson, W. Lu, H. Xu, P. Kim, M. J. Kreder, J. Alvarenga, and J. Aizenberg. Inhibition of ice nucleation by slippery liquid-infused porous surfaces (slips). *Phys. Chem. Chem. Phys.*, 15:581–585, 2013.

[192] P. Irajizad, M. Hasnain, N. Farokhnia, S. M. Sajadi, and H. Ghasemi. Magnetic slippery extreme icephobic surfaces. *Nat. Commun.*, 7:13395, 2016.

[193] B. R. Solomon, K. S. Khalil, and K. K. Varanasi. Drag reduction using lubricant-impregnated surfaces in viscous laminar flow. *Langmuir*, 30:10970–10976, 2014.

[194] B. J. Rosenberg, T. Van Buren, M. K. Fu, and A. J. Smits. Turbulent drag reduction over air- and liquid-impregnated surfaces. *Phys. Fluids*, 28:015103, 2016.

[195] T. V. Buren and A. J. Smits. Substantial drag reduction in turbulent flow using liquid-infused surfaces. *J. Fluid Mech.*, 827:448–456, 2017.

[196] M. K. Fu, I. Arenas, S. Leonardi, and M. Hultmark. Liquid-infused surfaces as a passive method of turbulent drag reduction. *J. Fluid Mech.*, 824:688–700, 2017.

[197] S. Anand, A. T. Paxson, R. Dhiman, J. D. Smith, and K. K. Varanasi. Enhanced condensation on lubricant-impregnated nanotextured surfaces. *ACS Nano*, 6:10122–10129, 2012.

[198] R. Xiao, N. Miljkovic, R. Enright, and E. N. Wang. Immersion condensation on oil-infused heterogeneous surfaces for enhanced heat transfer. *Sci. Rep.*, 3:1988, 2013.

[199] T. Kajiya, F. Schellenberger, P. Papadopoulos, D. Vollmer, and H.J. Butt. 3d imaging of water-drop condensation on hydrophobic and hydrophilic lubricant-impregnated surfaces. *Sci. Rep.*, 6:23687, 2016.

[200] K. C. Park, P. Kim, A. Grinthal, N. He, D. Fox, J. C. Weaver, and J. Aizenberg. Condensation on slippery asymmetric bumps. *Nature*, 531:78–82, 2016.

[201] P. B. Weisensee, Y. Wang, Q. Hongliang, D. Schultz, W. P. King, and N. Miljkovic. Condensate droplet size distribution on lubricant-infused surfaces. *Int. J. Heat Mass Transfer*, 109:187–199, 2017.

[202] P. Zhang, F. Y. Lv, A. Askounis, D. Orejon, and B. Shen. Role of impregnated lubricant in enhancing thermosyphon performance. *Int. J. Heat Mass Transfer*, 109:1229—1238, 2017.

[203] D. J. Preston, Z. Lu, Y. Song, Y. Zhao, K. L. Wilke, D. S. Antao, M. Louis, and E. N. Wang. Heat transfer enhancement during water and hydrocarbon condensation on lubricant infused surfaces. *Sci. Rep.*, 8:540, 2018.

[204] W. Ma, Y. Higaki, H. Otsuka, and A. Takahara. Perfluoropolyether-infused nanotexture: a versatile approach to omniphobic coatings with low hysteresis and high transparency. *Chem. Commun.*, 49:597–599, 2013.

[205] X. Yao, Y. Hu, A. Grinthal, T. S. Wong, L. Mahadevan, and J. Aizenberg. Adaptive fluid-infused porous films with tunable transparency and wettability. *Nat. Mater.*, 12:529–534, 2013.

[206] N. Vogel, R. A. Belisle, B. Hatton, T. S. Wong, and J. Aizenberg. Transparency and damage tolerance of patternable omniphobic lubricated surfaces based on inverse colloidal monolayers. *Nat. Commun.*, 4:2176, 2013.

[207] S. Sunny, N. Vogel, C. Howell, T. L. Vu, and J. Aizenberg. Lubricant-infused nanoparticulate coatings assembled by layer-by-layer deposition. *Adv. Funct. Mater.*, 24:6658–6667, 2014.

[208] A. C. Glavan, R. V. Martinez, A. B. Subramaniam, H. J. Yoon, R. Nunes, H. Lange, M. M. Thuo, and G. M. Whitesides. Omniphobic "rf paper" produced by silanization of paper with fluoroalkyltrichlorosilanes. *Adv. Funct. Mater.*, 24:60–70, 2014.

[209] J. S. Wexler, I. Jacobi, and H. A. Stone. Shear-driven failure of liquid-infused surfaces. *Phys. Rev. Lett.*, 114:168301, 2015.

[210] X. Hou, Y. Hu, A. Grinthal, M. Khan, and J. Aizenberg. Liquid-based gating mechanism with tunable multiphase selectivity and antifouling behaviour. *Nature*, 519:70–73, 2015.

[211] P. S. Brown and B. Bhushan. Liquid-impregnated porous polypropylene surfaces for liquid repellency. *J. Colloid Interface Sci.*, 487:437—443, 2017.

[212] H. Guo, P. Fuchs, K. Casdorff, B. Michen, M. Chanana, H. Hagendorfer, Y. E. Romanyuk, and I. Burgert. Bio-inspired superhydrophobic and omniphobic wood surfaces. *Adv. Mater. Interfaces*, 4:1600289, 2017.

[213] C. Howell, T.L. Vu, J.J. Lin, S. Kolle, N. Juthani, E. Watson, J.C. Weaver, J. Alvarenga, and J. Aizenberg. Self-replenishing vascularized fouling-release surfaces. *ACS Appl. Mater. Interfaces*, 6:13299–13307, 2014.

[214] A. Eifert, D. Paulssen, S. N. Varanakkottu, T. Baier, and S. Hardt. Simple fabrication of robust water-repellent surfaces with low contact-angle hysteresis based on impregnation. *Adv. Mater. Interfaces*, 1:1300138, 2014.

[215] X. Yao, J. Ju, S. Yang, J. Wang, and L. Jiang. Temperature-driven switching of water adhesion on organogel surface. *Adv. Mater.*, 26:1895–1900, 2014.

[216] X. Yao, S.S. Dunn, P. Kim, M. Duffy, J. Alvarenga, and J. Aizenberg. Fluorogel elastomers with tunable transparency, elasticity, shape-memory, and antifouling properties. *Angew. Chem. Int. Ed.*, 53:4418–4422, 2014.

[217] Q. Wei, C. Schlaich, S. Prevost, A. Schulz, C. Bottcher, M. Gradzielski, Z. Qi, R. Haag, and C. A. Schalley. Supramolecular polymers as surface coatings: rapid fabrication of healable superhydrophobic and slippery surfaces. *Adv. Mater.*, 26:7358–7364, 2014.

[218] U. Manna and D. M. Lynn. Fabrication of liquid-infused surfaces using reactive polymer multilayers: principles for manipulating the behaviors and mobilities of aqueous fluids on slippery liquid interfaces. *Adv. Mater.*, 27:3007–3012, 2015.

[219] L. Yu, G. Y. Chen, H. Xu, and X. Liu. Substrate-independent, transparent oil-repellent coatings with self-healing and persistent easy-sliding oil repellency. *ACS Nano*, 10:1076–1085, 2016.

[220] P. Zhang, H. Liu, J. Meng, G. Yang, X. Liu, S. Wang, and L. Jiang. Grooved organogel surfaces towards anisotropic sliding of water droplets. *Adv. Mater.*, 26:3131–3135, 2014.

[221] X. Yao, S. S. Dunn, P. Kim, M. Duffy, J. Alvarenga, and J. Aizenberg. Fluorogel elastomers with tunable transparency, elasticity, shape- memory, and antifouling properties. *Angew. Chem. Int. Ed.*, 53:4418–4422, 2014.

[222] C. Urata, G. J. Dunderdale, M. W. England, and A. Hozumi. Self-lubricating organogels (slugs) with exceptional syneresis-induced anti-sticking properties against viscous emulsions and ices. *J. Mater. Chem. A*, 3:12626–12630, 2015.

[223] O.G. Piringer and A.L. Baner, editors. *Plastic Packaging: Interactions with Food and Pharmaceuticals, 2nd Edition*. Wiley-VCH, 2008.

[224] J. Aizenberg, M. Aizenberg, P. Kim, and X. Yao. Structured flexible supports and films for liquid-infused omniphobic surfaces, us patent no. 20150209846. Technical report, 2015.

[225] T. Yabe, T. Takajo, S. Kato, and F. Ueki. Lubricant-supplying properties and durability of oil-impregnated polymers. *Tribology Trans.*, 43:453–458, 2000.

[226] W. E. Jamison, J. J. Kauzlarich, and R. E. Mondy. Lubricant supply characteristics of a microporous polymer. *A S L E Transactions*, 21:71–77, 1978.

[227] K. Golovin and A. Tuteja. A predictive framework for the design and fabrication of icephobic polymers. *Sci. Adv.*, 3:e1701617, 2017.

[228] P. Kim, M. J. Kreder, J. Alvarenga, and J. Aizenberg. Hierarchical or not? effect of the length scale and hierarchy of the surface roughness on omniphobicity of lubricant-infused substrates. *Nano Lett.*, 13:1793–1799, 2013.

[229] M. Muschi, B. Brudieu, J. Teisseire, and A. Sauret. Drop impact dynamics on slippery liquid-infused porous surfaces: influence of oil thickness. *Soft Matter*, 14:1100–1107, 2018.

[230] A. M. Cazabat and M. A. C. Stuart. Dynamics of wetting: effects of surface roughness. *J. Phys. Chem.*, 90:5845–5849, 1986.

[231] J. Bico, C. Tordeux, and D. Quéré. Rough wetting. *Europhys. Lett.*, 55:214–220, 2001.

[232] M. Conrath, N. Fries, M. Zhang, and M. E. Dreyer. Radial capillary transport from an infinite reservoir. *Transp. Porous Med.*, 84:109–132, 2010.

[233] E.W. Washburn. The dynamics of capillary flow. *Phys. Rev.*, 17:273–283, 1921.

[234] A. Hammad, T. D. Swinburne, H. Hasan, S. Del Rosso, L. Iannucci, and A. P. Sutton. Theory of the deformation of aligned polyethylene. In *Proc. R. Soc. A*, 2015.

[235] P. J. Phillips. Mechanism of orientation of aromatic molecules by stretched polyethylene. *Chem. Rev.*, 90:425–436, 1990.

[236] G. Martic, F. Gentner, D. Seveno, D. Coulon, , J. De Coninck, and T. D. Blake. A molecular dynamics simulation of capillary imbibition. *Langmuir*, 18:7971–7976, 2002.

[237] S. Supple. and N. Quirke. Rapid imbibition of fluids in carbon nanotubes. *Phys. Rev. Lett.*, 90:214501, 2003.

[238] D. I. Dimitrov, A. Milchev, and K. Binder. Capillary rise in nanopores: molecular dynamics evidence for the lucas-washburn equation. *Phys. Rev. Lett.*, 99:054501, 2007.

[239] W. Andrew. *Chemical resistance of plastics and elastomers (4th Electronic edition).* Plastics Design Library, 2008.

[240] H. Schott. Kinetics of swelling of polymers and their gels. *J. Pharm. Sci.*, 81:467–470, 1992.

[241] G. S. Jamieson and W. F. Baughman. The chemical compostion of cottonseed oil. *J. Am. Chem. Soc.*, 42:1197–1204, 1920.

[242] C. Roberts, A. Graham, M. Nemer, L. Phinney, R. Garcia, and E. Stirrup. Physical properties of low-molecular weight polydimethylsiloxane fluids. Technical report, 2017.

[243] W. Woishnis and S. Ebnesajjad. *Chemical Resistance of Thermoplastics*. Elsevier, 2012.

[244] Y. Liu. *Silicone Dispersions*. CRC Press, 2017.

[245] M. Salame. An empirical method for the prediction of liquid permeation in polyethylene and related polymers. *SPE Trans.*, 1:153–163, 1961.

[246] W. M. Lee. Selection of barrier materials from molecular structure. *Polym. Engg. Sci.*, 20:65–69, 1980.

[247] B. A. Morris. *The science and technology of flexible packaging: multilayer films from resin and process to end use*. Elsevier, 2017.

[248] J. H. Kim and J. P. Rothstein. Delayed lubricant depletion on liquid-infused randomly rough surfaces. *Exp. Fluids*, 57:81, 2016.

[249] J.J. Van Rossum. Viscous lifting and drainage of liquids. *Appl. Sci. Res.*, 7:121–144, 1958.

[250] G.I. Taylor. Deposition of a viscous fluid on the wall of a tube. *J. Fluid Mech.*, 10:161–165, 1961.

[251] B.G. Cox. On driving a viscous fluid out of a tube. *J. Fluid Mech.*, 14:81–96, 1962.

[252] A. Ali, A. Underwood, Y.R. Lee, and D.I. Wilson. Self-drainage of viscous liquids in vertical and inclined pipes. *Food and Bioproducts Processing*, 99:38—50, 2016.

[253] A. S. Haase, J. A. Wood, L. M. J. Sprakel, and R. G. H. Lammertink. Inelastic non-newtonian flow over heterogeneously slippery surfaces. *Phys. Rev. E*, 95:023105, 2017.

[254] G. G. Pereira. Effect of variable slip boundary conditions on flows of pressure driven non-newtonian fluids. *J. Non-Newtonian Fluid Mech.*, 157:197–206, 2009.

[255] T. G. Myers. Application of non-newtonian models to thin film flow. *Phys. Rev. E*, 72:066302, 2005.

[256] Q.H. Nguyen and N.D. Nguyen. *Continuum Mechanics - Progress in Fundamentals and Engineering Applications*. InTech, 2012.

[257] A. Keiser, L. Keiser, C. Clanet, and D. Quéré. Drop friction on liquid-infused materials. *Soft Matter*, 13:6981–6987, 2017.

[258] F. Brochard and P. G. deGennes. Shear-dependent slippage at a polymer/solid interface. *Langmuir*, 8:3033–3037, 1992.

[259] K. Watanabe and H. Udagawa. Drag reduction of non-newtonian fluids in a circular pipe with a highly water-repellent wall. *AIChE J.*, 47:256–262, 2001.

[260] H. Jeffreys. The draining of a vertical plate. *Proc. Cambridge Philos. Soc.*, 26:204–205, 1930.

[261] J. Seiwert, M. Maleki, C. Clanet, and D. Quéré. Drainage on a rough surface. *Europhys. Lett.*, 94:16002, 2011.

[262] X. Liu, S. J. Feakins, X. Dong, Q. Xue, T. Marek, D. I. Leskovar, C. B. Neely, and A. M. H. Ibrahim. Experimental study of leaf wax n-*alkane* response in winter wheat cultivars to drought conditions. *Org. Geochem.*, 113:210–223, 2017.

[263] J. B. Boreyko and C. H. Chen. Restoring superhydrophobicity of lotus leaves with vibration-induced dewetting. *Phys. Rev. Lett.*, 103:174502, 2009.

[264] X. Chen, R. S. Patel, J. A. Weibel, and S. V. Garimella. Coalescence-induced jumping of multiple condensate droplets on hierarchical superhydrophobic surfaces. *Sci. Rep.*, 6:18649, 2016.

[265] M. Watkins, J. VandeVondele, and B. Slater. Point defects at the ice (0001) surface. *Proc. Natl. Acad. Sci. U.S.A.*, 28:12429–12434, 2010.

[266] H. Zhang, J. de Poorter, R. Mukherjee, J. B. Boreyko, and R. Qiao. Thermoelectrics in ice slabs: charge dynamics and thermovoltages. *Phys. Chem. Chem. Phys.*, 10.1039/D1CP02304G, 2021 (Accepted Manuscript).

[267] H. J. Butt and M. Kappl. *Surface and interfacial forces*. Wiley, 2010.

[268] J. N. Israelachvili. *Intermolecular and surface forces*. Academic Press, 1990.

Dormammu, I've come to bargain.